Onshore/Offshore Structure of the Northern Cascadia Subduction Zone from Bayesian Receiver Function Inversion

by

Camille Brillon
B.Sc., University of Alberta, 2003

A Thesis Submitted in Partial Fulfillment of the
Requirements for the Degree of

MASTER OF SCIENCE

in the School of Earth and Ocean Sciences

Onshore/Offshore Structure of the Northern Cascadia Subduction Zone from Bayesian Receiver Function Inversion

by

Camille Brillon

B.Sc., University of Alberta, 2003

Supervisory Committee

Dr. John Cassidy, Co-Supervisor

(Pacific Geoscience Centre, Natural Resources Canada)

Dr. Stan Dosso, Co-Supervisor

(School of Earth and Ocean Sciences, University of Victoria)

Dr. Garry Rogers, Member

(Pacific Geoscience Centre, Natural Resources Canada)

Supervisory Committee

Dr. John Cassidy, Co-Supervisor

(Pacific Geoscience Centre, Natural Resources Canada)

Dr. Stan Dosso, Co-Supervisor

(School of Earth and Ocean Sciences, University of Victoria)

Dr. Garry Rogers, Member

(Pacific Geoscience Centre, Natural Resources Canada)

ABSTRACT

This study applies Bayesian inversion to receiver functions (RF) to estimate local shear wave velocity (V_s) structure of the crust and upper mantle beneath two ocean bottom seismometers (OBS) offshore, and two land-based seismometers onshore Vancouver Island, British Columbia, Canada. We use passive seismic data recorded on NC89, a permanent NEPTUNE (North-east Pacific Time-series Undersea Networked Experiments) OBS located on the continental slope, and on a temporary autonomous KECK foundation OBS, KEBB, located at the Endeavour segment of the Juan de Fuca Ridge (JdFR). The two land based seismometers (OZB and PGC) are located on Vancouver Island and are part of the Canadian National Seismograph Network

(CNSN). The introduction of NEPTUNE has helped to fill a gap in offshore seismic monitoring, however; due to high noise levels and a relatively short deployment time, few useful events have been recorded (to date) for RF analysis. In this study, we utilize three-component, broadband recordings of large (M6+), distant (30°-100°) earthquakes to compute RFs due to locally generated P (compressional) to S (shear) converted waves. RFs are then inverted using a non-linear Bayesian approach which yields optimal profiles of V_s, V_p (compressional wave velocity), and strike and dip angles, as well as rigorous uncertainty estimates for these parameters. Near the JdFR a thin sediment layer ($\leq$1 km) is resolved overlying a 2 km thick oceanic crust. The crust contains a large velocity contrast at the depth of an expected axial magma chamber. The oceanic crust thickens to 10 km at the continental slope where it is overlain by 5 km of sediments. At the coastal station (OZB) a low velocity zone is imaged at 16 km depth dipping approximately 12° NE. Evidence for this low velocity zone is also seen beneath southern Vancouver Island (PGC) at a depth consistent with previous studies. Determining such models at a number of locations (from the spreading ridge to the coast) provides new information regarding local structure and can aid in seismic hazard analysis.

Contents

List of Tables

List of Figures

ACKNOWLEDGEMENTS

The idea for this research stemmed from the combination of the areas of interest of my supervisory committee: inversions, receiver functions and ocean bottom seismometers. I would like to thank Drs. John Cassidy, Stan Dosso and Garry Rogers for taking on this project with me. Thank you Drs. John Cassidy and Stan Dosso for your ongoing support, encouragement, advice and expertise throughout the past three years.

Throughout my degree I was fortunate to be located at the Pacific Geoscience Center and the University of Victoria; thank you to all students, staff and researchers at both institutions for sharing your knowledge and inspiring me to do valuable research. Thanks to Jan Dettmer for assistance with inversions, and Honn Kao for providing the forward model code used in my inversions as well as the support to go along with it. Also, thank you to Taimi Mulder, Natalie Balfour, and Wanda Bentkowski for teaching me how to use the Antelope software package and all I know about locating earthquakes.

I would also like to acknowledge NEPTUNE Canada for access to their OBS data, William Wilcock for access to the KECK OBS data set, and NRCAN for data from the CNSN network.

Of course the past three years wouldn't have been successful without my outstanding network of friends whom have motivated me by showing interest in my work, and my well being. Whether it was a lake run that left me aching, a never ending bike ride, a quiet dinner, or sharing your stories of graduate school, it was all appreciated.

Chapter 1

Introduction

1.1 Setting

Vancouver Island, British Columbia, lies above the Cascadia Subduction Zone (CSZ). Offshore the west coast of Vancouver Island lies the small, oceanic Juan de Fuca (JdF) plate bound by the Pacific plate to the west, North American (NA) plate to the east, Explorer plate to the north, and Gorda plate to the south (figure 1.1). Approximately 250 km off the west coast of Vancouver Island is the JdF ridge (JdFR, figure 1.1). Here the Pacific and JdF plates diverge at a full spreading rate of 56 mm/year (Wilson, 1993; Canales et al., 2009). This spreading centre creates a scientifically important and intriguing environment as earthquakes, volcanoes, and hydrothermal vents are some of the many tectonic processes that occur here.

Just to the west of Vancouver Island the JdF and NA plates converge at ∼46 mm/year (Riddihough and Hyndman, 1991). The younger, warmer JdF plate subducts beneath the older, cooler NA plate at N56° E, (Riddihough and Hyndman, 1991, figure 1.1). As subduction proceeds, sediments are scraped off the JdF plate and added to the NA plate, further increasing thickness by creating an accretionary

wedge (Hyndman, 1995). Currently, there is little to no motion observed between the two plates, which leads to the belief that the plates are in a locked state (Hyndman and Rogers, 2010), storing energy. It is likely that when the locked portion of this boundary is released, there will be up to a M9+ earthquake similar to the historical 1700 Cascadia earthquake or the recent March 17, 2011, Tohoku event.

At the north and south boundaries of the JdF plate are seismically active transform faults which represent the differing east-west motions of the Explorer and Gorda plates which border the JdF plate to the south and north, respectively (figure 1.1).

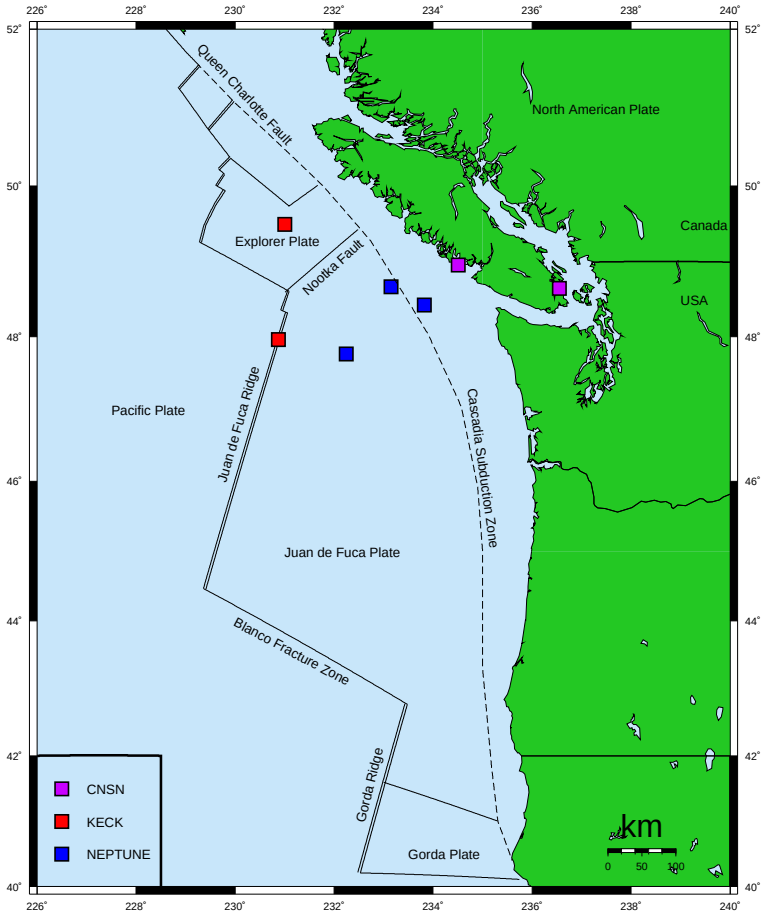

Figure 1.1: Tectonic setting offshore Vancouver Island, BC, Canada. Squares represent seismograph stations from indicated datasets.

1.2 Motivation

The current collection of geophysical results paints a widely accepted picture of the JdF plate from ridge to deformation front, and further east beneath Vancouver Island. Seismic reflection and refraction, gravity and magnetic surveys as well as core sampling have resulted in a set of known properties of the CSZ. While refraction lines provide an interpretation of compressional wave velocities (V_p), reflection surveys have the ability to define interfaces and structural variations, but do not resolve the actual velocities as well as the refraction surveys. Gravity and magnetic surveys highlight broad density and mineral anomalies, which gives an idea of general structure. Logs and cores obtained from the Ocean Drilling Project (ODP) provide precise localized measurements, but sample mainly sediments and uppermost crust. The one property that remains largely unconstrained is the shear wave velocity, V_s. A more accurate V_s profile will aid in determining the hazard that the locked portion of the CSZ poses to NA.

Receiver Function (RF) analysis utilizes waveforms from distant earthquakes recorded on three component broadband seismometers to estimate the V_s profile beneath a seismic station. Seminal developments in RF studies were conducted by Langston (1977, 1979), Owens (1984), Ammon (1991), and Cassidy (1992). Originally, RFs were computed in the frequency domain, and resulting models were found via forward modelling. The current processing speed of computers coupled with advances in inversion techniques has allowed RF analysis methods to develop into more computationally aggressive operations.

Today, common RF analysis techniques include forward modelling and optimization. Forward modelling allows the analyst to create a V_s profile which may be biased by their preconceived ideas, which can result in models with more detail than what the raw data actually support. Optimization methods find a model which minimizes

the data misfit. Neither of these methods provide a quantitative measure of parameter uncertainties. Alternatively, Bayesian inversion attempts to find a best fitting model and accompanying posterior probability density (PPD). From statistical investigation of the PPD, a meaningful representation of the model uncertainty can be quantified.

The introduction of NEPTUNE (North-East Pacific Time-series Undersea Networked Experiments) to the scientific community provides new data in an intriguing environment that has, until this point, seen relatively little research. PGC, a Canadian National Seismograph Network (CNSN) station near Sidney, BC, has been utilized for RF studies. Results from those studies agree with active seismic studies and tectonic theories, making this station ideal to evaluate new RF inversion techniques. OZB is a CNSN station located on the west coast of Vancouver Island where the JdF plate is early in its descent. Data recorded at OZB has yet to be used for RF analysis. Ocean bottom seismometers (OBS) have filled a gap in seismic monitoring. Along with existing CNSN stations OBS provide an opportunity to apply RF analysis to a corridor extending from the JdF ridge across the CSZ to southern Vancouver Island, which will enhance existing knowledge regarding the depth of the subducting JdF plate in that area.

Characteristics of the CSZ that remain unclear include the depth of the JDF plate beneath Vancouver Island, the thickness of the subducting oceanic crust, where in this structure earthquakes occur, and why they occur. This study will contribute to the results of previous research and assist in determining these characteristics.

Chapter 2

Previous Work

2.1 Oceanic Crust

With the exception of plate boundaries, hot spots, and fracture zones, is it generally agreed that the thickness and structure of the oceanic crust is consistent through out the world's oceans (White et al., 1992). The accepted general model of the oceanic crust is divided into a layer of sediments plus three prominent sub-layers as shown in figure 2.1 and outlined below (from White et al., 1992).

Layer 1: Oceanic sediments

Layer 2A: Extrusive basaltic lavas and dikes

2.11 ± 0.55 km thick, V_p = 2.5 – 6.6 km/s

Layer 2B: Gabbros

4.97 ± 0.90 km thick (2/3 of the igneous crust)

V_p = 6.7 – 7.2 km/s

Layer 3: Mantle peridotite

$V_p \geq$ 7.6 km/s

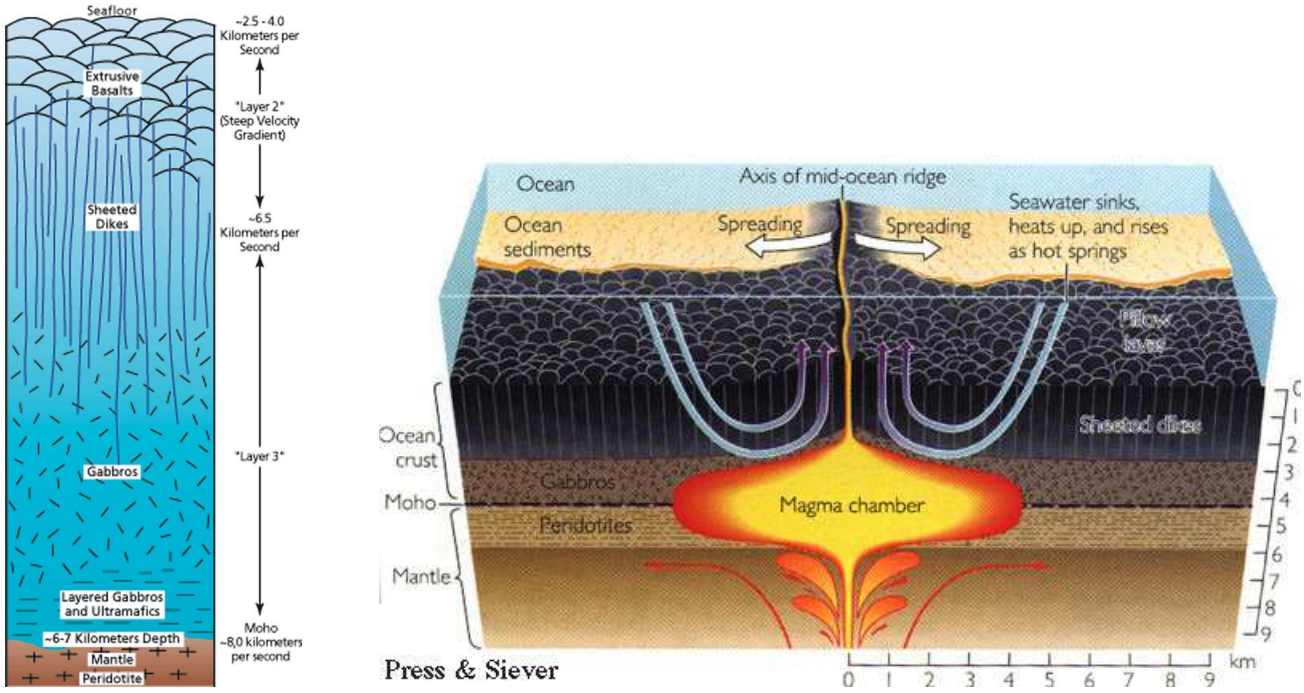

Figure 2.1: (left) General structure of oceanic crust (Tucholke, 1998);(right) formation of oceanic crust at fast spreading ridges (Press and Seiver, 2001).

2.2 Juan de Fuca Ridge

The JdFR (figure 1.1) is oriented N20° E and has a half spreading rate of ∼30–35 mm/year (Wilson et al., 1984; Riddihough, 1984; Hasselgren and Clowes, 1995). Such a spreading rate defines the JdFR as an intermediate spreading ridge (Van Ark et al., 2007), which has characteristics shared by both fast (e.g. East Pacific Rise) and slow (e.g. Mid-Atlantic Ridge) spreading ridges. The JdFR is composed of five segments (Endeavour, Northern Symmetric, Co-Axial, Vance and Cleft). Each segment has similar features that differ in size. Each segment has an axial ridge ∼20 km wide that rises to 200–450 m above the seafloor with an axial summit graben (ASG) 0.5 km (Cleft and Endeavour) to 7 km (Vance) wide and 30 m (Cleft and Endeavour) to 250 m (Vance) deep (Rohr et al., 1988; Canales et al., 2005).

My research focuses on the Endeavour segment, the northernmost segment of the JdFR, that is home to five high temperature vents (Barclay and Wilcock, 2004), and

is the most seismically active, although it has no evidence of recent eruptions. The region of high seismicity is located at a depth range of 1.5–3.5 km below the sea floor (Wilcock et al., 2002, 2007).

In 1985 the first seismic reflection line, line 85-03, was recorded across the Endeavour segment of the JdFR (figure 2.2). Interpretations of this line led Rohr et al. (1988) to believe that at this location layer 2A is 600–1000 m thick with velocities between 3.5 km/s and 4.5 km/s. Beneath 2A, pore space is infilled with sediment and velocities increase to 5–6 km/s forming layer 2B, which extends to 2.5 km beneath the seafloor. At this depth it was hypothesized that a 1 km wide axial magma chamber (AMC), or area of high temperature, creates a reflection seen on line 85-03, which coincides with the layer 2B/3 interface predicted by Cudrack and Clowes (1993). The oceanic Moho across the ridge is seen on line 85-03 at 6.6 km and 4.2 km below the seafloor on the Pacific and JdF plates, respectively.

Interpreting the SEISRIDGE-85 seismic refraction survey (figure 2.2), White and Clowes (1987, 1990) arrived at a similar result to that of Rohr et al. (1988). Layer thicknesses and velocities were estimated from travel time tomography to be 2A: 250–650 m, 2.5 km/s; 2B: 800 m, 4.8 km/s; 3: 5.8 km/s. A region 3–4 km wide and approximately 800 m thick extending from layer 2B to 3 showed a 0.4 km/s velocity decrease. This decrease in velocity was not significant enough to be considered an AMC, but instead a layer of increased fracturing and hydrothermal circulation.

Similar to White and Clowes (1987), Cudrack and Clowes (1993) did not detect the existence of an AMC from the SEISRIDGE-85 data. Their final average interpretation (figure 2.3) consists of a four layer model that has velocities ranging from 2.56–6.50 km/s, with a 0.1–0.2 decrease of V_p gradient in layer 3. The change in gradient was not interpreted as an AMC but as a region of higher temperatures.

Compliance measurements (which are highly sensitive to the shear modulus and

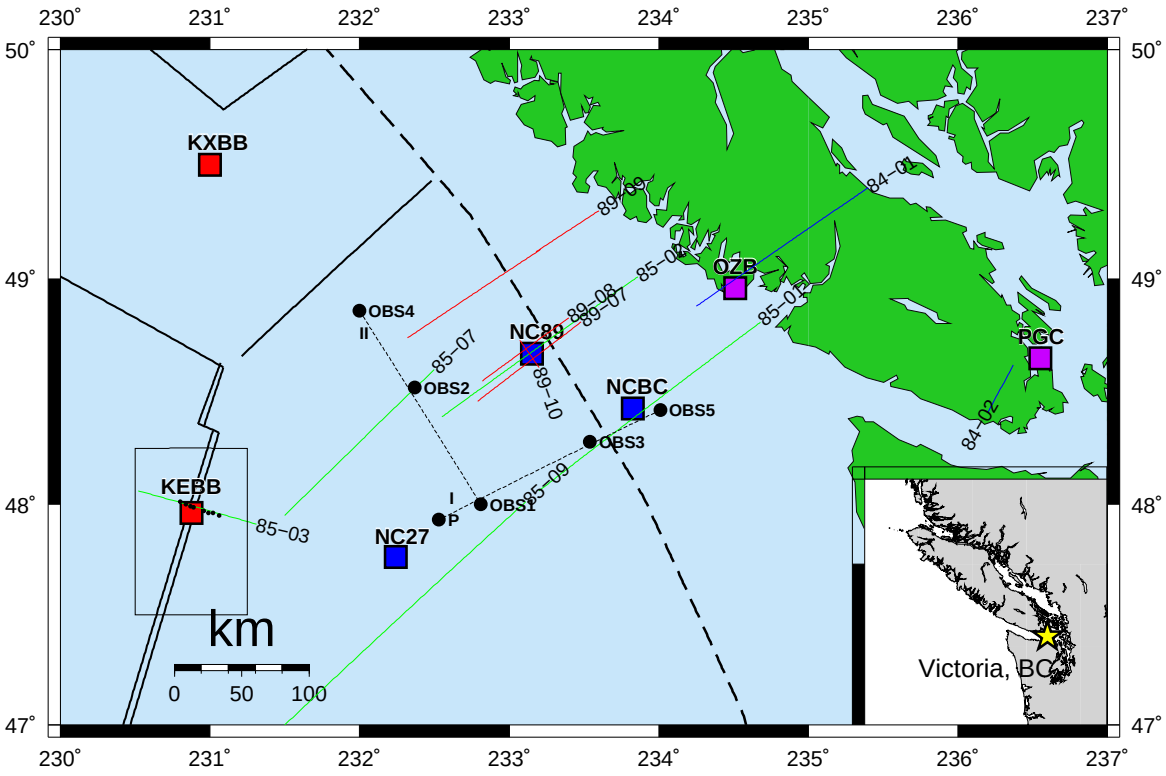

Figure 2.2: Location of previous seismic studies. Green and red lines represent LITHOPROBE and SEISRIDGE85 reflection lines, respectively. Black circles are OBS locations used for VISP I and II (large circles) and SEISRIDGE85 (small circles) refraction surveys. Black square outlines the area covered by 25 MCS lines interpreted by Van Ark et al. (2007). Coloured squares represent seismic stations as in figure 1.1

.

thus V_s) were made 4 km east of Endeavour ridge axis in August and September 1993 and inverted for V_s. Inversion results showed a general lower V_s at the Endeavour segment, but no indication of an AMC that far from the ridge axis was seen (Crawford, 1994).

In 2002, a multi-channel seismic reflection survey (MCS) was conducted 50 km along the Endeavour, Vance and Cleft segments of the JdFR (Canales et al., 2005, 2009; Van Ark et al., 2007). Interpretations for each of these segments predicted an AMC 2–3 km below the seafloor at all segments, similar to that predicted by Rohr

et al. (1988) and coincident to the hydrothermal reactive and high seismicity zone specified by Wilcock et al. (2002, 2007). The size and shape of the AMC differ for each segment but have similar general characteristics. In each segment the AMC is overlain by layer 2A, which is thinner (250–350 m) on the ridge, and thickens to 500–600 m off-axis. Velocities of layer 2A decrease from ∼4.7 km/s above the AMC to 2.26 km/s near-axis, then increase to 3.18 km/s 9 km off-axis (figure 2.3). More detailed processing from Canales et al. (2009) also showed an off-axis thin magma lens 850-900 m above the Moho.

Comparing the reflection seen on MCS lines from 2002 to that of AMC seen at other spreading ridges and considering seismicity at the JdFR, Van Ark et al. (2007) concluded that the AMC at Endeavour is 0.4–1.2 km wide and extends 16–24 km along the ridge, 2.1–3.3 km below the seafloor. On top of the AMC is a thin layer of sediments and a distinct 180–630 m thick layer 2A. Below the AMC an intermittent reflector is seen at ∼5 km depth (1.9–2.4 s two-way travel time) that is likely representative of the Moho.

It is agreed that faulting and hydrothermal circulation are present at Endeavour (and other segments), which would suggest that Poisson's ratio, and hence the V_p/V_s values, will vary across the ridge. Hyndman (1979) found that the oceanic crust has a higher V_p/V_s ratio (1.81–1.91) than the mantle (∼1.71) due to weathering, porosity, fractures, and alteration of minerals. Wilcock et al. (2002) also discovered a highly varying V_p/V_s ratio (between 1.6 and 2.0) with a best fit solution for the area being 1.84, indicating anisotropy. This result agrees with conclusions from Cudrack and Clowes (1993) and Clowes and Au (1993) which saw 10% P wave and negligible S wave anisotropy in the upper mantle.

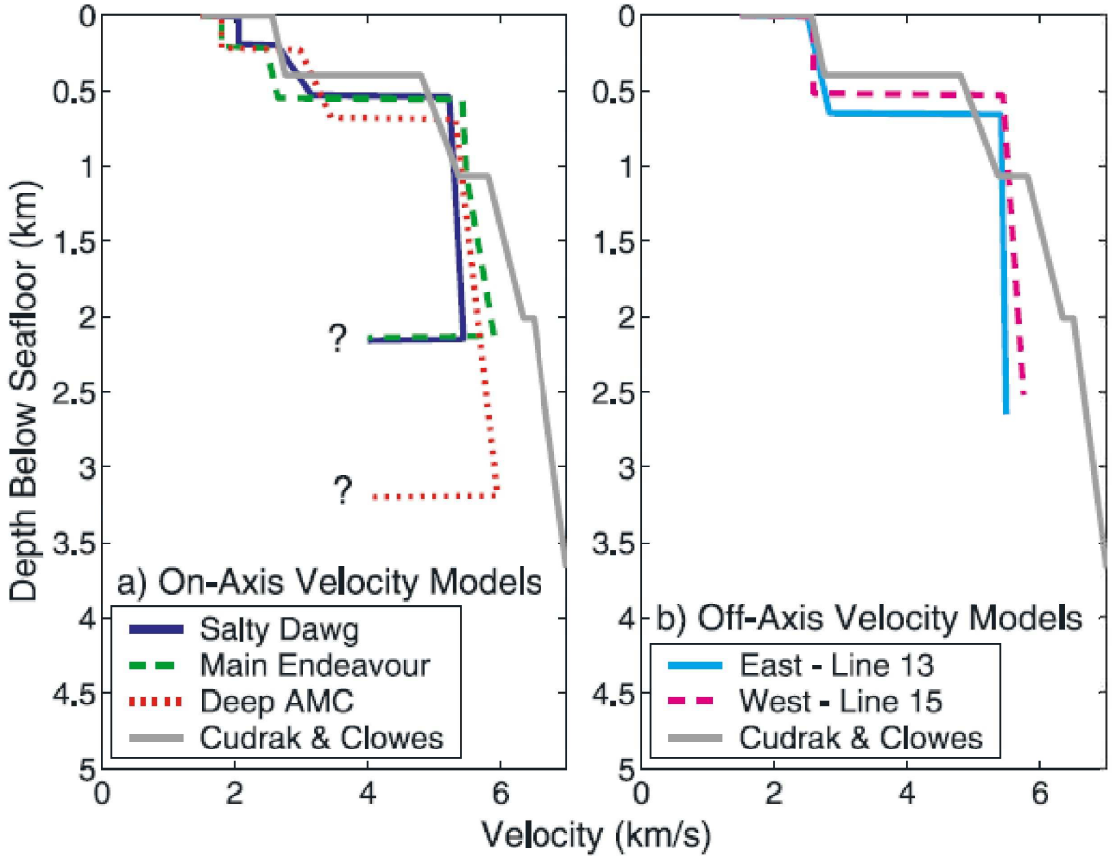

Figure 2.3: P wave velocities on and near the JdFR as determined by Van Ark et al. (2007) and Cudrack and Clowes (1993) using seismic reflection data.

2.3 Abyssal Plain

Located between the JdFR and the deformation front lies the Cascadia abyssal plain (figure 1.1). Interpretations of LITHOPROBE lines 85-07 and 85-09 (figure 2.2) describe this area as fairly uniform with a slight eastward dip of the JdF plate (<1°) and thickening of sediments (200–1600 m) (Hasselgren and Clowes, 1995). Across the plain the oceanic crust deviates from uniform in the vicinity of pseudo-faults and intraplate faults. Pseudofaults are expressions of ridge propagation which have been detected on magnetic surveys as a change in the magnetic signature where the old crust meets the new crust (Wilson et al., 1984). Two major pseudofaults of the

Endeavour segment are pseudofaults 4 and 7.

The east end of line 85-07 (figure 1.1) coincides with the position of pseudofault 7, where sediments are significantly disturbed. Increases in crustal thickness are estimated to be up to 30% at pseudofault 7 (Hasselgren and Clowes, 1995). The velocity profile at the eastern end of line 85-07 is shown in figure 2.4. The overall structure and velocities agree reasonably well with the velocity structure (figure 2.4) determined by White and Clowes (1987) using data from the VISP II refraction line (figure 2.2), which predicts a crustal thickness of 8.4 km.

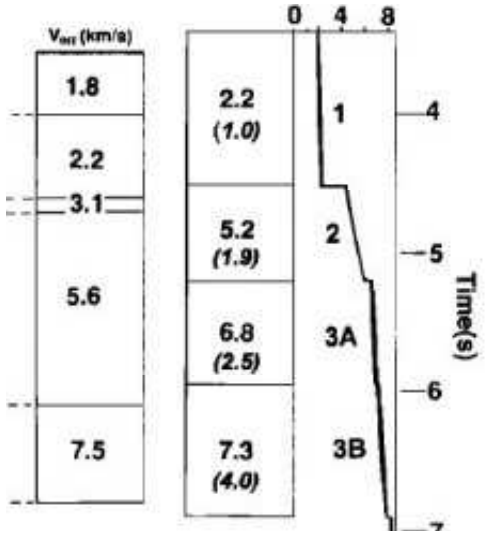

Figure 2.4: P wave velocities (km/s) on abyssal plain from (left) line 85-07 reflection and (right) VISP II refraction. Numbers in parenthesis are approximate layer thicknesses in km (Hasselgren and Clowes, 1995).

McClymont and Clowes (2005) investigated the anomalous thickening of the crust proposed by Hasselgren (Hasselgren et al., 1992; Hasselgren and Clowes, 1995) near pseudofaults 4 and 7. A nine layer velocity model with a 43% thickening of layer 3 was used to predict the gravity profile across an area of thickened crust. The predicted gravity did not produce a negative anomaly of the expected size. The gravity anomaly observed was successfully modelled with two serpentinized (25%-30%) anomalous crustal bodies which have a similar P wave velocity as gabbro, but a lower density (3.1 g/cm^3 compared to 3.3 g/cm^3), which is characteristic of serpentinized peridotite (McClymont and Clowes, 2005). Hence, the zones of high reflectivity on lines 85-07 and 85-09 may be explained by highly serpentinized peridotite that extends from 2–6 ma (40 km) about each pseudofault (Calvert et al., 1990; McClymont and Clowes, 2005).

2.4 Northern Cascadia Deformation Front

The deformation front is considered to be the location where the JdF plate begins to plunge beneath the NA plate (figure 1.1). As the subduction proceeds, crustal deformation occurs. Here sediments are scraped off the top of the JdF plate and are added to the NA plate, creating what is known as the accretionary wedge. Since the early 1980's an extensive collection of geophysical data has been gathered across the CSZ in an attempt to illuminate and understand the subduction process and associated hazards.

In 1980 the Vancouver Island Seismic Project (VISP) recorded four seismic refraction profiles within the CSZ. VISP I (figure 2.2) was an offshore-onshore line perpendicular to the subduction zone near Barkley Canyon. Waldron (1982) and Spence et al. (1985) interpreted this line, with the former focusing on the offshore

portion. Using modelling constraints from a continuous seismic profile, a multichannel channel seismic survey, free air gravity, and well logs, Waldron (1982) produced models corresponding to waveforms recorded on the three OBS used in the offshore portion of VISP I. West of the deformation front (OBS #1), the sediments and underlying crust have virtually no dip, and the Moho is at 9 km depth. Moving towards the slope (OBS #3), the model depicts a thickening of sediments from 1 km on the abyssal plain to 2 km at the foot of the continental slope, while the JdF plate also begins a slight $\sim 3^\circ$ eastward dip and velocity increase. East of the deformation front (OBS #5), the Moho dips to the east $\sim 6^\circ$ and low velocity sediments are detected which are interpreted as former oceanic sediments that have been accreted to the NA plate (Waldron, 1982).

Following the VISP project, the LITHOPROBE program conducted numerous seismic reflection surveys across the CSZ. Also, in 1985 marine seismic surveys as a part of the Frontier Geoscience Program were recorded. Lines from this collection of surveys that serve as a comparison to my research are 85-03 (previously discussed), 85-01 and 85-02 (figure 2.2).

Seismic line 85-01 is coincident to VISP I and is a continuation of the 84-01 LITHOPROBE onshore line. Drew (1987) focused on these two lines to update the velocity model from Waldron's 1982 result. The final model from Drew (1987, figure 2.5) did not differ greatly from Waldron (1982) in the offshore area.

In 1989 LITHOPROBE conducted another large survey across the northern Cascadia margin. Included in this were reflection lines 89-07 and 89-08 perpendicular to the subduction front and 89-10 parallel to the front (figure 2.2). Lines 89-08 and 89-10 coincide with the Ocean Drilling Project's hole 889 and NEPTUNE's node ODP89. Using velocity constraints from Waldron (1982), Yuan et al. (1994) used lines 89-07 and 89-10 to investigate the velocity of the oceanic plate seaward and landward of

the deformation front. The conclusions of that study were that velocities increase landwards towards the deformation front, where velocities then decrease. These velocity changes are due to compaction and decrease in pore fluids of the sediments in the early stages of accretion, followed by an unconsolidation once the sediments have been scraped off the JdF plate and added to the NA plate (Yuan et al., 1994).

Interpretations of lines 89-08 and 85-02 as well as ODP sites show an 2.5-3 km thick incoming sediment layer comprised of turbidites and hemipelagics overlying the oceanic crust. At ODP 889 the first 87 m is comprised of clayey silts and silty sands interbedded with sand layers indicative of accretionary wedge sediments. Beneath that is a transition to clayey silts similar to that seen on the abyssal plain (Scherwath et al., 2006). Since this area is abundant in gas hydrates, most research focuses on determining properties of the sediments where hydrates occur. Few interpretations of deeper structure are available.

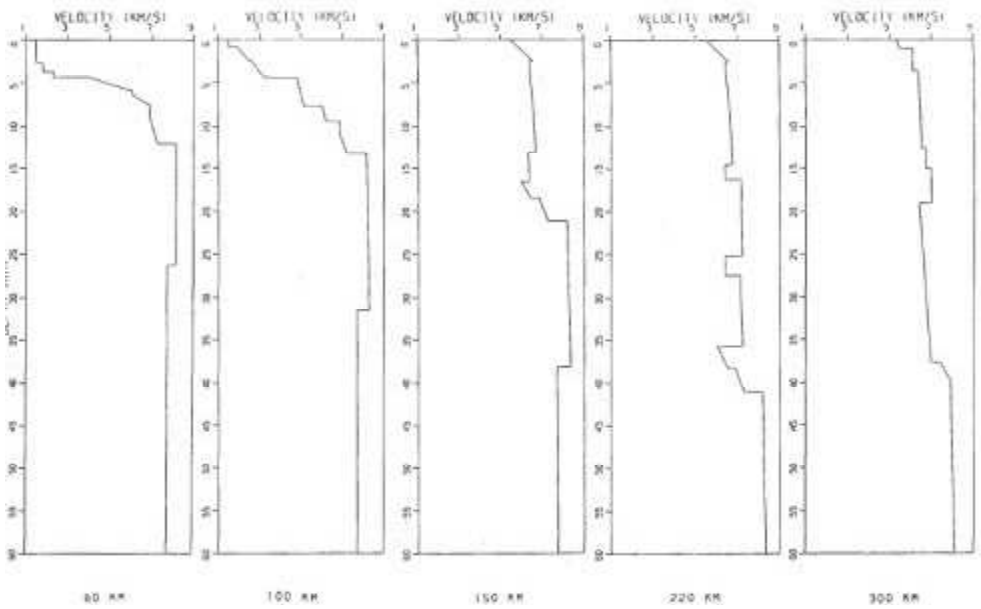

Figure 2.5: Velocity profile from deep ocean to mainland BC Distances at along the bottom axis (60 km, 100 km, 150 km, 220 km, 300km) refer to distances east of point P on figure 2.2 along line I. The vertical scale ranges from 0 to 60 km depth in 5 km increments. The horizontal scale is V_p from 1 km/s to 9 km/s incremented by 2 km/s. (Drew, 1987).

2.5 Vancouver Island

Numerous geophysical studies in this area have led to the velocity structure beneath Vancouver Island being quite well defined. There is some agreement about the velocity structure of the oceanic and continental plates in this area, but, remarkably there are still some aspects that are not agreed upon.

Existing studies on Vancouver Island include receiver function analysis (Cassidy and Ellis, 1993), seismic reflection and refraction (Spence et al., 1985, as part of LITHOPROBE, SHIPS (Seismic Hazard in Puget Sound) and VISP), gravity (Riddihough, 1979), magnetic (Clowes et al., 1997), magnetelluric (Kurtz et al., 1990), and seismicity (Calvert et al., 2011). From this collection, main attributes of the Cascadia subduction zone are:

1. The Pacific Rim and Crescent Terranes were accreted to the Wrangellian Terrane during the Eocene. The accretionary wedge accreted to, and the JdF plate subducted beneath, these formations.

2. The top of the F reflector is at approximately 30 km depth beneath the west coast of Vancouver Island and 40 km depth beneath central Vancouver Island.

3. The eastward dip of the JdF plate increases from 3°–4° west of the deformation front to 8° at the deformation front and 14° beneath Vancouver Island.

4. There is a zone of high velocity (7.1 km/s) bound by low velocity zones at 15 km and 30 km depth. The low velocity bands represent the C and E reflectors which merge into one thin (<2 km) reflector offshore.

5. There is ∼5–8 km between the bottom of the E and top of the F reflectors.

6. At shallow depths low velocity accretionary sediments are imaged.

7. The gravity signature across the JdF plate is similar to that seen on other ridges and subduction zones. There is a gravity low across the sediment filled trench at the foot of the continental slope and a large, positive gravity anomaly across Vancouver Island is modelled by a high density root beneath Vancouver Island but above the JdF plate.

8. Magnetic and gravity profiles across the subduction zone have large anomalies, which are evidence of non-uniform structure. Onshore, magnetic anomalies are aligned with the accreted terranes. Offshore, magnetic anomalies between the basin and deformation front are aligned with the seafloor spreading. Large gravity and magnetic anomalies are seen across known pseudofaults.

9. Most onshore seismicity is located in the upper 20 km of the NA plate which falls within the continental crust.

10. Magnetotelluric stations across Vancouver Island have defined a conductive dipping layer that is believed to be the E layer. To achieve the conductivities observed, fluid porosity between 1%–4% is required.
    (from Hyndman et al., 1990)

Initial interpretations of LITHOPROBE lines estimated the top of the F layer to represent the subducting oceanic crust reaching depths of 40 km beneath Vancouver Island, (Hyndman et al., 1990, figure 2.6). Since then, other theories have developed. Calvert (Calvert, 2004; Calvert et al., 2011) proposed that the E reflector represents a ∼5 km thick imbricated zone where oceanic sediments have been subducted and underplated. This sequence is seen as a high velocity layer sandwiched by two low velocity layers (E and F) totalling about 16 km above the top of the JdF plate represented by the F reflector. Ramachandran et al. (2006) also predicted that the subducting JdF crust, represented by the F reflector, lies 30–45 km beneath Vancouver Island.

Based on newer SHIPS and LITHOPROBE transects, Nedimovic et al. (2003) proposed that the E layer is <2 km thick offshore central Vancouver Island and 5–7 km thick on the west coast of Vancouver Island. This theory interprets the E reflector as a layer of shearing, which forms reflective mylonites, and fluid (to satisfy the high conductivity observed at corresponding depths). This theory would result in the bottom of the seismic E layer representing the top of the oceanic crust at ∼35 km depth beneath Vancouver Island.

Interpretations based on recent RF analysis by Nicholson et al. (2005) agree with a shallower subducting oceanic plate. Based on studies at other subduction zones, it was postulated that the low velocity seismic E layer represents the subducting crust of the JdF plate (figure 2.7). As the subduction proceeds, the plate is de-watering, creating a layer of high conductivity and reflectivity (Bostock et al., 2002). Nicholson

et al. (2005) estimates the top of the 4–5 km thick E layer dipping at 16.5° along a strike −48° at ∼22 km depth on the western coast of Vancouver Island and ∼30 km beneath Vancouver Island, which is 8–10 km shallower than predicted by Hyndman et al. (1990), Calvert (2004) and Cassidy and Ellis (1993), and 4–5 km shallower than predicted by Nedimovic et al. (2003).

Though numerous studies have been carried out which address the structure of the CSZ, the velocity structure and what the velocity profile represents has not been agreed upon. Questions remain regarding the depth of the JdF plate and thickness of the oceanic crust, as well as how these properties change as subduction proceeds.

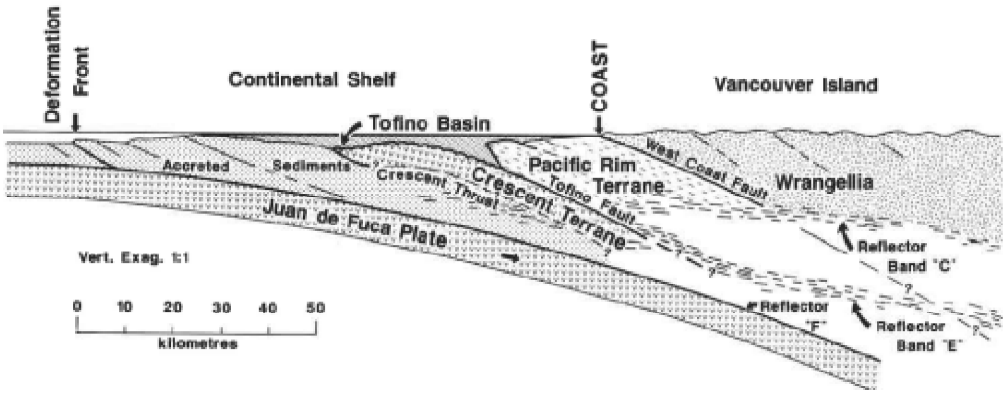

Figure 2.6: Cross section of Cascadia from ocean basin to mainland BC derived from a combination of geophysical studies (Hyndman, 1995).

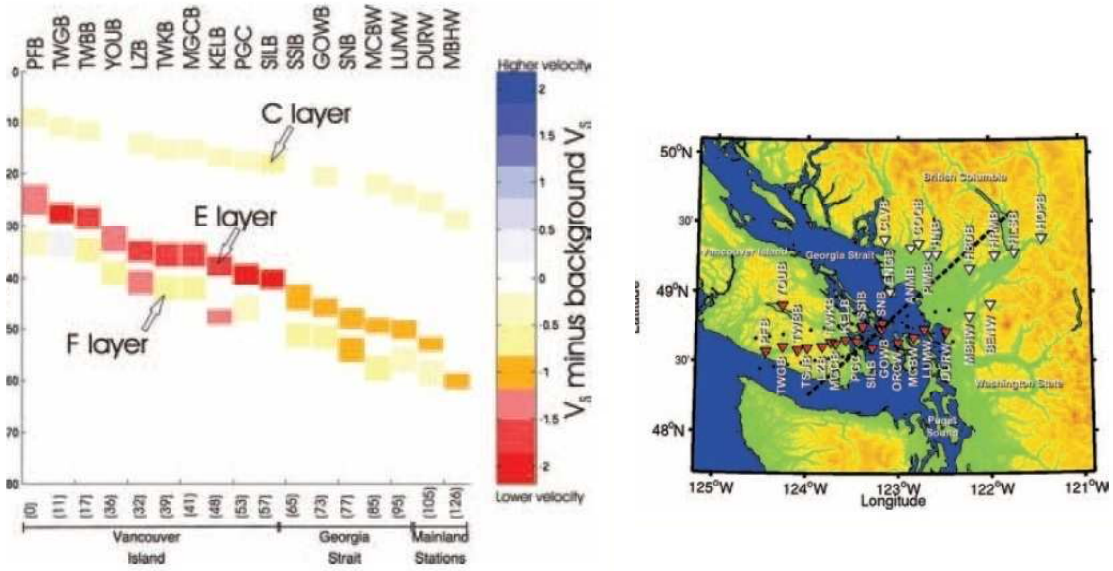

Figure 2.7: S wave velocity structure beneath Vancouver Island (left) determined from RF obtained from Polaris stations (right) (Nicholson et al., 2005).

Chapter 3

Receiver Functions

3.1 Theory

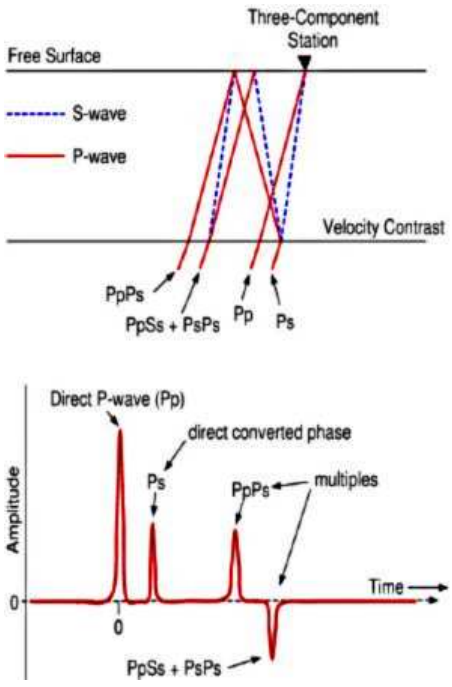

Figure 3.1: Illustration of a simple receiver function. TOP: converted body waves; BOTTOM: corresponding receiver function (Ammon, 1991).

Seismic recordings of distant earthquakes (teleseisms) contain an abundance of information. Information about the source, the wave's path through the mantle, and the near surface velocity structure is all encompassed within a waveform. To isolate the effect of the subsurface beneath a station, path and source effects are removed from the waveform leaving the receiver function (RF).

When a primary compressional wave (P) from a distant earthquake approaches a seismograph from beneath the surface, it encounters interfaces. At each of these inter-

faces, some of the P wave energy can be converted to P and S waves. If there are numerous interfaces, conversions can happen each time a wave passes through an interface. The result of this is that the P-coda contains P to S converted wave arrivals (Ps) and multiples.

Ps arrivals are not usually evident on the raw waveforms. Processing (section 3.2) is needed to obtain a RF where the converted waves are dominant (figure 3.1). Receiver functions are calculated from earthquakes where the angular epicentral distance of the source of the earthquake is 30°–100° away from the designated three-component seismic station. This distance range ensures that the angle of incidence beneath the station can be approximated as near vertical and that the recorded waveforms are not reflections from the surface or core. The closer the source is to the receiver the less attenuation and therefore more energy will arrive at the seismometer resulting in a larger amplitude RF. As well, a closer source ensures a less steep angle of incidence which allows for more energy to be converted and recorded on horizontal components. The deeper the source, the less the travel path and crustal effects near the source will contribute noise to the signal. Choosing deep ($\geq$25 km) events from distances as close to 30° as possible (but not less), will result in the most accurate RF to analyze.

Within the RF the first large arrival is the direct P wave. Subsequent converted waves arrive at a time after the direct P wave arrival that depends on the depth and velocity contrast of interfaces. The amplitude and polarity of an arrival is dependent upon the velocity contrast between contiguous layers. The larger positive or negative a contrast, the larger positive or negative (respectively) the amplitude of the converted wave (Ammon, 1991). By convention, each time a conversion is made the arrival of the waveform is denoted by a P followed by an s or p, depending on if the converted wave is shear or compressional (respectively). Each RF is unique, but will be influenced in the same way by the properties of the crustal structure.

Other properties that determine the waveform character are dip, strike, and gradational boundaries. The dip, and by association the strike, of each interface, affect the amplitudes and arrival time of Ps conversions. If the source is down-dip of the station (waves travel up-dip), the amplitude and travel time increase. The opposite occurs for a wave travelling down-dip. If a wave travels along strike there is no effect on the radial RF. Given this, to obtain a well constrained model of strike and dip interfaces, RF from a wide range of back azimuths (BAZ) are needed (Cassidy, 1992).

Dipping layers also introduce a transverse component to the RF waveform. Waves travelling up or down dip will not introduce a transverse response, while those travelling along strike will. If transverse components are available they help to better constrain dipping layers. However, a more complex geology will create complex transverse RF that are not easily modelled. For this reason, the transverse RF is not often used (Cassidy, 1992).

The distance around the station that the RF samples depends on the length of time the data used represents as well as the depth of the targeted interface. The longer the time window, the more multiples are included, which sample a greater lateral distance than the direct Ps arrival. From Snell's law, for an interface depth of h km and ray parameter of 0.06 s/km, the lateral distance a wave samples is determined by $h\tan(\text{asin}(0.06V_s))$(Ammon, 1991).

3.2 Receiver Function Calculation

3.2.1 Frequency Domain Deconvolution

Assuming the travel path beneath a station is near-vertical, the P-coda of any teleseismic waveform recorded on the vertical component of the seismograph will be dominated by P-waves containing information regarding the source of the earthquake

and any path effects. The horizontal channels will record these same effects, as well as locally generated Ps conversions (and their multiples) that only appear on the horizontal components. Deconvolving the waveform recorded on the vertical component from the horizontal component results in a RF, which isolates the converted waves (Langston, 1979).

In the frequency domain, let the vertical component be Z(ω), and the two horizontal channels be N(ω) and E(ω). The first step is to rotate the horizontal waveforms into radial and tangential components (parallel and perpendicular direction to the earthquake), R(ω) and T(ω). The radial and transverse RF, RF_r and RF_t, respectively, can then calculated using spectral division, as follows.

Radial receiver function:

$$RF_r = \frac{R(\omega)}{Z(\omega)}. \tag{3.1}$$

Tangential receiver function:

$$RF_t = \frac{T(\omega)}{Z(\omega)}. \tag{3.2}$$

Problems arise when $Z(\omega)$ is small making the deconvolution unstable. To solve this problem, Langston (1979) introduced a source equalization method which involves dividing by an averaging function, $A(\omega)$, dependant on a Gaussian filter $G(\omega)$. This method also includes a water-levelling parameter (c) that ensures small values in the denominator will not cause the deconvolution to fail. The general equations 3.1 and 3.2 become

$$RF = \frac{R(\omega)A(\omega)}{Z(\omega)}, \tag{3.3}$$

where

$$A(\omega) = \frac{R(\omega)\overline{R(\omega)}G(\omega)}{\phi(\omega)}, \tag{3.4}$$

$\overline{R(\omega)}$ is the complex conjugate of $R(\omega)$,

$$G(\omega) = \exp \frac{-\omega^2}{4\alpha^2}, \tag{3.5}$$

and

$$\phi = \max(R(\omega)\overline{R(\omega)}, c(R(\omega)\overline{R(\omega)})). \tag{3.6}$$

The Gaussian width, α, can affect the perceived characteristics of a RF. Varying α will control the frequency content of the RFs and hence the ability to resolve thin layers. When α=3, frequencies greater than $\sim$ 0.5 Hz are filtered out, resulting in a lower frequency RF, that only sample thicker layers. Alternatively, an α value of 7 removes frequencies greater than $\sim$2 Hz and will resolve any arrivals that sampled the same layers as the α=3 RF as well as thinner layers. Hence, the larger α is the higher the expected layer resolution. Cassidy (1992) determined minimum layer thicknesses of 1, 2 and 3 km can be determined from α values of 7, 5, and 3 (respectively). Trying to resolve thin layers without including higher frequencies results in under-determined velocity contrasts.

3.2.2 Time Domain Deconvolution

Ammon (1991) introduced a new deconvolution method that simplified and improved the deconvolution by introducing an iterative method that preserves amplitudes. In this approach the RF is computed via a time domain process which predicts the peaks of a RF. This deconvolution uses the vertical, $Z(t)$, and either the radial, $R(t)$, or transverse, $T(t)$, components to estimate a series of 'bumps' representing the RF waveform. The largest arrivals on $R(t)$ or $T(t)$ and $Z(t)$ are indicated using cross-correlation and are approximated first with smaller arrivals predicted in succession. A single iteration to calculate a radial receiver function, $RF_r(t)$ proceeds as follows.

1. Estimate a single bump of $RF_r(t)$ using a Gaussian pulse as source.

2. Multiply $RF_r(t)$ with $Z(t)$ to estimate $R(t)$.

3. Compute the misfit between the estimated $R(t)$ and observed $R(t)$.

4. Add another bump to the estimated $RF_r(t)$ and repeat the process.

A user defined maximum number of bumps or a minimum improvement between iterations determines when the deconvolution has achieved an acceptable result and is stopped. A Gaussian filter is applied in this process but neither c or a conversion to the frequency domain is needed. Because the method of Langston (1979) normalizes the RF by the $A(\omega)$, and the method of Ammon (1991) does not, an adjustment to the RF computed by the time domain method is required before comparison with a RF computed by the frequency domain method can be carried out. Dividing the time domain RF by the value in the right column of table 3.1 for the corresponding Gaussian width α used in the iterative deconvolution, the amplitudes the two RFs are comparable.

Table 3.1: Receiver Function Normalization (Ammon, 1991).

Gaussian Width	**Scaling Factor**
0.5	0.29
1.0	0.57
1.5	0.85
2.5	1.42
3.0	1.70
5.0	2.83

Chapter 4

Inversion Methodology

4.1 Bayes Method

Existing inversion approaches to estimating the shear-wave velocity model responsible for a specific RF or set of RFs include forward modelling (Cassidy, 1992), linearization (Ammon et al., 1990), genetic algorithms (Shibutani et al., 1996), and neighbourhood algorithms (Sambridge, 1999a). These methods aim to find the model that produces the lowest misfit to the observed RF. Solutions from these methods are often presented as the best model with its associated misfit. Sometimes, in addition to plotting the estimated model, an ensemble of arbitrarily good fitting models is also plotted in an attempt to qualitatively illustrate the range of possible solutions. What is missing from such solutions is a rigorous quantitative measure of uncertainty of the results. An approach to address this shortcoming is Bayesian inversion (Tarantola, 1987; Gilks et al., 1996; Sambridge and Mosengaard, 2002). Bayesian inversion is based on the idea that the model parameters of interest represent random variables. The solution to a Bayesian inversion represents probability distributions for these random variables, constrained by data and prior information, so that quantitative conclusions about the

parameter resolution are achieved.

Derived from definitions of joint and conditional probability, for fixed, measured data $\mathbf{d}$ and model $\mathbf{m}$, Bayes rule gives an expression for the posterior probability density (PPD) as

$$P(\mathbf{m}|\mathbf{d}) = \frac{P(\mathbf{d}|\mathbf{m})P(\mathbf{m})}{P(\mathbf{d})}. \tag{4.1}$$

Since $\mathbf{d}$ is known $P(\mathbf{d})$ is constant. $P(\mathbf{m})$ is the prior information which constrains the parameters, while $P(\mathbf{d}|\mathbf{m})$ is the conditional probability of $\mathbf{d}$ given $\mathbf{m}$, which represents the data uncertainty distribution. However, since $\mathbf{d}$ is known, this term can also be interpreted as the likelihood of a model, $\mathbf{L}(\mathbf{m})$.

Writing $L(\mathbf{m}) \propto \exp[-E(\mathbf{m})]$, where $E(\mathbf{m})$ is the data misfit, the PPD can be written in the form

$$P(\mathbf{m}|\mathbf{d}) \propto e^{[-\{E(\mathbf{m}) - \log_{\mathbf{e}} \mathbf{P}(\mathbf{m})\}]}. \tag{4.2}$$

Defining the total misfit of the model, including data and prior information, as

$$\phi(\mathbf{m}) = E(\mathbf{m}) - \log_e P(\mathbf{m}), \tag{4.3}$$

the PPD becomes

$$P(\mathbf{m}|\mathbf{d}) = \frac{e^{[-\phi(\mathbf{m})]}}{\int e^{[-\phi(\mathbf{m}')]} d\mathbf{m}'}. \tag{4.4}$$

For problems involving a large number of parameters, the multidimensional PPD is difficult to represent. Properties of the PPD are estimated to give a quantitative representation, including the following.

Most-probable model: Maximum *a posteriori* (MAP) model,

$$\hat{\mathbf{m}} = \mathrm{Arg}_{\max} P(\mathbf{m}|\mathbf{d}) = \mathrm{Arg}_{\min} \phi(\mathbf{m}). \tag{4.5}$$

Mean Model: Average of each parameter,

$$\bar{\mathbf{m}} = \int \mathbf{m}' P(\mathbf{m}'|\mathbf{d}) d\mathbf{m}'. \tag{4.6}$$

Model Covariance Matrix: The main diagonal gives the parameter variances, off diagonal elements are covariances,

$$\mathbf{C_m} = \int (\mathbf{m}' - \bar{\mathbf{m}})(\mathbf{m}' - \bar{\mathbf{m}})^T P(\mathbf{m}'|\mathbf{d}) d\mathbf{m}'. \tag{4.7}$$

Correlation Matrix: Gives normalized correlation coefficients between parameters. A value of 1, -1 and 0 in the correlation matrix corresponds to parameters being correlated, anti-correlated and uncorrelated, respectively. Values between 0 and -1 show evidence of a negative correlation between two parameters, whereas a value between 0 and $+1$ shows a positive correlation. The larger positive or negative the value the stronger the correlation or anti-correlation. The correlation matrix is given by

$$\mathbf{R}_{ij} = \frac{\mathbf{C}_{ij}}{\sqrt{\mathbf{C}_{ii}\mathbf{C}_{jj}}}. \tag{4.8}$$

Marginal Probability Distribution: In one dimension, this represents the distribution of a single parameter with all other parameters integrated out. This concept can be extended to two dimensions and joint marginals show the relationships between two parameters. In one and two dimensions (respectively), these are represented by

$$P(\mathbf{m}_i|\mathbf{d}) = \int \delta(\mathbf{m}'_i - \mathbf{m}_i) P(\mathbf{m}'|\mathbf{d}) d\mathbf{m}' \tag{4.9}$$

$$P(\mathbf{m}_i, \mathbf{m}_j|\mathbf{d}) = \int \delta(\mathbf{m'}_i - \mathbf{m}_i)(\mathbf{m'}_j - \mathbf{m}_j)P(\mathbf{m'}|\mathbf{d})d\mathbf{m'}. \tag{4.10}$$

The MAP model (equation 4.5) is determined using an optimization method (discussed later in this section). The remaining properties require solving the multidimensional integrals above. For a non-linear problem, such as RF inversion, these integrals must be solved numerically, generally using Markov Chain Monte Carlo (MCMC) methods (Tarantola, 1987; Gilks et al., 1996; Sambridge and Mosengaard, 2002).

4.2 Likelihood

The likelihood and data misfit functions depend on the assumed statistical distribution of data errors. In an ideal, simple case the data errors represent independent, identically distributed (IID) Gaussian random variables with standard deviation σ, and the likelihood is defined as

$$L(\mathbf{m}, \sigma) = \frac{1}{(2\pi)^{N/2}\sigma^N} \exp\left[-\frac{|\mathbf{d} - \mathbf{d}(\mathbf{m})|^2}{2\sigma^2}\right]. \tag{4.11}$$

If σ is not known, it can be included as an unknown in the inversion. A maximum likelihood estimate for σ can be determined by equating the partial derivative of equation (4.11) with respect to σ to 0 and solving gives

$$\sigma^2 = \frac{1}{N}|\mathbf{d} - \mathbf{d}(\mathbf{m})|^2. \tag{4.12}$$

Substituting equation (4.12) into equation (4.11), the likelihood becomes

$$L(\mathbf{m}) = \frac{N^{\frac{N}{2}} \exp\left[-\frac{N}{2}\right]}{2\pi\,|\mathbf{d} - \mathbf{d}(\mathbf{m})|^N}, \tag{4.13}$$

and the misfit becomes

$$E(\mathbf{m}) = \frac{N}{2} \log_e \left| \mathbf{d} - \mathbf{d}(\mathbf{m}) \right|^2 . \tag{4.14}$$

If the data errors are assumed to be correlated with a covariance matrix $\mathbf{C_d}$, the likelihood becomes

$$L(\mathbf{m}) = \frac{1}{(2\pi)^{N/2} \left| \mathbf{C_d} \right|^{1/2}} \exp \left[\frac{(\mathbf{d} - \mathbf{d}(\mathbf{m}))^T \mathbf{C_d}^{-1} (\mathbf{d} - \mathbf{d}(\mathbf{m}))}{2} \right], \tag{4.15}$$

and the corresponding misfit function is

$$E(\mathbf{m}) = \frac{1}{2} (\mathbf{d} - \mathbf{d}(\mathbf{m}))^T \mathbf{C_d}^{-1} (\mathbf{d} - \mathbf{d}(\mathbf{m})). \tag{4.16}$$

4.3 Numerical Optimization

Adaptive simplex simulated annealing (ASSA) is the optimization method used in this thesis for determining the MAP model for RF inversion. ASSA combines the global search method of simulated annealing (SA) and the local downhill simplex method (DHS) to ensure efficient sampling of the parameter space without getting trapped in local minima (Dosso et al., 2001). To explain ASSA, the methods of SA and DHS are first briefly reviewed.

4.3.1 Simulated Annealing

SA is a global search method that mimics the process of thermodynamic annealing by which crystals grow. For a system described by M parameters $\mathbf{m} = \{m_i, i = 1, .., M\}$, the probability of a given model is given by the Boltzman or Gibbs distribution

$$P(\mathbf{m}) = \frac{1}{Z} e^{-E(\mathbf{m}) k_b T}, \tag{4.17}$$

where E is the free energy of the system, T is the absolute temperature, k_b is Boltzman's constant and Z is the partition function, $Z = \sum_{\mathbf{m}} e^{-E(\mathbf{m})k_b T}$.

The crystallization process begins at a melting point (high T) and then the system is slowly cooled. As T decreases, the Gibbs distribution will favour low energies. If cooled slow enough, the atoms will form a single crystal that has the minimum energy. If the system is cooled too fast many small crystals that represent local energy minima are formed. Using a Markov chain Monte Carlo method, specifically Metropolis Hasting sampling (MHS) with a decreasing temperature, a system in Gibbs equilibrium can be simulated as it is cooled and settles into its ground state (global minimum energy). An analogous procedure can be used to find the optimum solution to an inversion problem (Kirkpatrick et al., 1983; Ingber, 1989).

MHS samples a parameter space accepting or rejecting a random perturbation to a model based on the Metropolis criterion (MC). This criterion is based on the following conditions (where ΔE reflects the misfit of the new model minus that of the old model and k_b is absorbed into T):

- If $\Delta E \leq 0$, the new model is accepted.
- If $\Delta E > 0$, the model is accepted based on a random number, ζ, drawn from a uniform distribution on [0,1]. If $\zeta \leq e^{-\Delta E/T}$, the perturbation is accepted, and if $\zeta \geq e^{-\Delta E/T}$, the perturbation is rejected.

This approach to optimization always accepts a downhill step (lower misfit), and sometimes accepts an uphill step (higher misfit), with probability according to the MC. The probability of accepting an uphill step is reduced as temperature decreases. This eventually leads to "freezing", where there are no more uphill steps accepted or downhill steps available. However, if cooled too quickly the optimization can get trapped in a local minimum, resulting in a suboptimal solution. To determine if this

has happened the optimization should be repeated a number of times or cooled more slowly to see if a lower energy model can be found.

4.3.2 Downhill Simplex

The downhill simplex method (DHS) is a local search method, which is efficient at searching for local minima (Nelder and Mead, 1965; Press et al., 1992). It is a gradient based method which move down gradients without computing partial derivatives or solving a system of equations.

This search method starts with a simplex of $M+1$ models, where M is the number of parameters defining a model. The models are ranked from highest to lowest misfit. This method makes a number of 'moves', as shown in figure 4.1 for $M = 3$, in an attempt to find a lowest misfit model. The algorithm first tries to find a better model by reflecting the highest misfit model through the simplex face formed by the other $M - 1$ models (figure 4.1b). If the reflection results in a model with a lower misfit than all other models in the simplex, an expansion is attempted by extending the reflection move by a factor of 2 (figure 4.1c). If the reflection did not find a model that fits better than the second worst model, the highest misfit model is contracted towards the face of the simplex by a factor of 1/2 (figure 4.1d). If the reflection and contraction did not produce a model with a misfit less than at least one other model in the simplex, a multiple contraction is applied (figure 4.1d). In this case all but the lowest misfit model are contracted by 1/2 towards this model. When the ratio of the difference between the highest and lowest misfit to the average the misfit is less than some user defined value, convergence is reached.

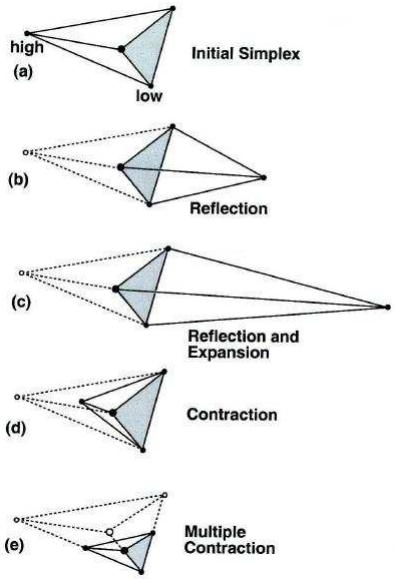

Figure 4.1: Downhill Simplex Method (a) starting simplex, (b) reflection, (c) expansion following reflection, (d) contraction and (e) multiple contraction (Dosso et al., 2001).

4.3.3 Adaptive Simplex Simulated Annealing

Separately, global (section 4.3.1) and local (section 4.3.2) search methods can produce reasonable results, but they each have shortcomings. Global search methods such as SA sample slowly, particularly for problems with correlated parameters which form narrow valleys in the search space. Local or gradient based methods such as DHS are efficient at searching narrow valleys, but not designed to move uphill, and can become trapped in local minima. Combining methods produces an efficient algorithm (Dosso et al., 2001).

To integrate the DHS with SA, a DHS step followed by a random perturbation is applied to a simplex of models to produce a perturbed model. This model is then accepted or rejected based on the MC. After a required number of perturbations have been accepted, the temperature is decreased according to $T_{i+1} = \beta T_i$ where $\beta < 1$. This procedure (perturbations and cooling) is repeated until the DHS convergence

criterion is reached.

In the ASSA algorithm, the random perturbations are chosen from a Cauchy distribution. The distributions are centred on the current parameter value with the distribution width scaled according to the average size of recently accepted perturbations. This provides an adaptive algorithm which automatically reduces perturbations sizes as the method converges.

The starting temperature is chosen so that essentially all perturbations are initially accepted allowing for the parameter space to be thoroughly sampled. An appropriate cooling rate which provides an adequate search of the space within a reasonable time frame typically requires some experimentation.

4.4 Numerical Integration

Multi-dimensional integrals of the form

$$I = \int f(\mathbf{m}')P(\mathbf{m}'|\mathbf{d})d\mathbf{m}', \tag{4.18}$$

such as equations 4.6–4.10, can be estimated numerically by MHS at temperature $T = 1$ drawing Q models $\mathbf{m}$ from a proposal distribution. The final estimate of the integral is represented by

$$I = \frac{1}{Q}\sum_{i=1}^{Q} f(\mathbf{m_i}). \tag{4.19}$$

The proposal distribution that parameters are drawn from can significantly effect efficiency. The ideal choice of proposal distribution would be the PPD itself; however, the PPD is the unknown in practical problems. The PPD can be approximated for the proposal distribution using linearization. According to linear inverse theory, the PPD of a model $\mathbf{m}$ is a Gaussian distribution about the MAP model with covariance

given by

$$\mathbf{C_m} = [\mathbf{J^T C_d}^{-1}\mathbf{J} + \mathbf{C_{\hat{m}}^{-1}}]^{-1}, \tag{4.20}$$

where $\mathbf{J}$ is the Jacobian of partial derivatives at $\hat{\mathbf{m}}$, $J_{ij} = \frac{\partial d_i(\hat{\mathbf{m}})}{\partial m_j}$, $\mathbf{C_d}$ is the data covariance matrix and $\mathbf{C_{\hat{m}}}$ is the covariance of an assumed Gaussian prior distribution.

For efficiency purposes, all MHS perturbations are made in principal-component parameter space (Dosso and Dettmer, 2011) so that $\mathbf{m_{rotated}} = \mathbf{U^T m}$ where $\mathbf{U}$ is the column eigen- vector matrix of the model covariance $\mathbf{C_m} = \mathbf{UWU^T}$ ($\mathbf{W}$ is the eigen-value matrix). After perturbation, the parameters are rotated back into the original parameter space $\mathbf{m} = \mathbf{U m_{rotated}}$ for evaluation of the forward model and acceptance/rejection according to the MC. To achieve a well mixed Markov chain that extensively samples that parameter space perturbations are drawn from a Cauchy distribution, scaled by the square root of the diagonal elements of W (principal component variances).

Using the linear approximation of the PPD as the proposal distribution, two MCMC samplers run in parallel selecting models according to MHS (Dosso and Dettmer, 2011). During a preliminary burn-in in stage samples are used to calculate a nonlinear estimate of $\mathbf{C_m}$ according to equation (4.7), after which these samples are discarded. The linearized approximation of $\mathbf{C_m}$ is then replaced by this nonlinear estimate and sampling continues to evaluate the general integral, equation (4.19).

To evaluate the state of the samplers the integral estimates of the pair of samplers are compared. When the difference between the two chains is insignificant, the sampling routine is complete. The final sample is a union of all the samples collected by the two samplers.

4.5 Parametrization

An important decision to be made for any inversion problem is the number of parameters used to represent the model. The number of layers chosen to represent the earth model in RF inversion is an example of this. In some cases the data may not contain enough information to constrain the layers one is attempting to solve for. This leads to an over-parametrized problem where some parameter values can have little effect on the model and are therefore unconstrained with large uncertainties. An under-parametrized inversion occurs when not enough layers are used to represent the model. In this case the existing parameters are often biased and uncertainties are under-estimated. The number of layers resolved by the data is generally not known *a priori*. One approach to estimating this is based on the Bayesian information criterion (BIC).

The BIC evaluates various model parametrizations by calculating their likelihood and penalizing for complexity, taking into account the number of data points being inverted. The parametrization with the lowest BIC value is the one recommended as the most simple parametrization that the data can resolve (Schwartz, 1978; Kass and Raftery, 1995).

Bayes theorem leads to a representation of Bayesian evidence for a parametrization $\mathcal{I}$,

$$P(\mathbf{d}|\mathcal{I}) = \int P(\mathbf{d}|\mathbf{m},\mathcal{I})\, P(\mathbf{m}|\mathcal{I})\, d\mathbf{m}. \tag{4.21}$$

Since the data are fixed, $P(\mathbf{d},\mathcal{I})$ is the likelihood of $\mathcal{I}$, where $P(\mathbf{m}|\mathcal{I})$ represents prior information. This integral is numerically challenging to solve but can be approximated by a point estimate as

$$-2\log_e P(\mathbf{d}|\mathcal{I}) \approx \mathrm{BIC} = -2\log_e L(\hat{\mathbf{m}}) + M\log_e N \tag{4.22}$$

or,

$$\mathrm{BIC} = 2E(\hat{\mathbf{m}}) + M \log_e N. \tag{4.23}$$

For high dimensional problems, calculating the MAP model with the lowest possible misfit can be a difficult task and hence the BIC may not be precisely estimated. However, even in these cases it should provide a reasonable estimate of the number of layers.

4.6 Data Error Estimation

Data errors in RF inversion combine observation, theory and processing errors. Observation errors can include instrumental and environmental noise as well as any instrument inconsistencies. Theory errors are related to shortcomings of the parametrization and forward model, such as an unknown number of layers and assumptions which might not be fully met (e.g., flat layered Earth and vertical incidence signal, no internal multiples). Processing errors are introduced when calculating the RF (deconvolution).

In an ideal inversion problem the data errors are known, independent, identically distributed (IID), Gaussian random errors. Most often, this is not the case. The goal of Bayesian inversion is to map data uncertainties into parameter uncertainties; therefore, a reasonable estimate of error statistics is required. How well these are estimated can significantly influence the solution. Underestimating data uncertainties leads to overly optimistic solutions, whereas overestimated uncertainties could result in a solution with excessive parameter uncertainties.

A variety of methods exist to determine data error statistics. Sambridge (1999b) estimated the errors from multiple realizations of correlated noise. Piana Agostinetti and Malinverno (2009) used the averaging function computed from the data, and

Bodin (2010) includes the variance and a simple parametrization for the covariance as unknowns in the inversion.

Assuming the error statistics are an IID random process they can be estimated from data error residuals (Dosso, 2002; Dosso et al., 2006). If correlated data errors are indicated correlation can be accounted for by constructing a data covariance matrix $\mathbf{C_d}$ from data residuals, i.e., the difference between the observed RF and the RF predicted by the MAP model, $\mathbf{r} = \mathbf{d} - \mathbf{d}(\hat{\mathbf{m}})$.

Formally, the data covariance matrix is defined

$$\mathbf{C} = \langle \left(\mathbf{r} - \langle \mathbf{r} \rangle\right) \left(\mathbf{r} - \langle \mathbf{r} \rangle\right)^T \rangle, \tag{4.24}$$

where $\langle \cdot \rangle$ represents an ensemble average over many realizations of the error process, which are often not available. However, if the error process can be assumed stationary and ergodic, a Toeplitz covariance matrix can be estimated by approximating the ensemble average of equation (4.24) by a finite temporal average over the residuals using a non-parametric procedure (Dosso et al., 2006):

$$\hat{C}_{ij} = \frac{1}{N} \sum_{k=1}^{N-|i-j|} \left(r_k - \bar{r}\right) \left(r_{k+|i-j|} - \bar{r}\right), \tag{4.25}$$

where $\bar{r}$ is the residual mean. The inversion is then repeated using this covariance matrix in the misfit function (this procedure can be repeated iteratively, but usually changes little after one iteration). In some cases, the residuals are not stationary as the variance appears to change slowly across the residuals. In this case a non-Toeplitz covariance matrix can be estimated by assuming the residuals are quasi-stationary (i.e., can be approximated as stationary over some finite time interval). This can be addressed using equation (4.25) averaging the residuals over the appropriate time window rather than over all points (Dosso and Dettmer, 2011).

The assumptions of Gaussian-distributed, random errors can be examined by considering the standardized residuals, $\mathbf{C_d}^{-1/2}\,\mathbf{r}$, which should be an uncorrelated Gaussian random process with unit standard deviation. Gaussianty and randomness can be considered using both qualitative and quantitative measures (Montgomery and Peck, 1992; DeGroot, 1975). Gaussianity can be considered qualitatively by comparing histograms of the standardized residuals with the standard Gaussian distribution. Quantitatively, the Kolmogorov-Smirnov (KS) test can be applied to quantify the evidence against Gaussianity in terms of a p value, with $p > 0.05$ considered no significant evidence. Randomness of the standardized residuals can be considered qualitatively in terms of their autocorrelation function. The autocorrelation function for random errors is characterized by a narrow peak at zero lag, whereas a wide peak indicates serial correlation. The runs test can be used to quantify the evidence against randomness in terms of a p value.

4.7 Forward Model

The forward modelling routine, RAY3D, used in ASSA and MHS follows methods of Langston (1977), implemented by Tom Owens in 1982 and revised numerous times by various users since then. This routine calculates travel times, azimuthal anomalies and ray parameter anomalies for primary converted waves and free surface multiples, assuming a plane wave. The model can support either layers with non-zero strike and dip angles, or V_s gradients, but not both. In the CSZ, the orientation of the JdF plate is important, therefore V_s gradients were not included in the model. The output is a synthetic seismogram for the model with layers described by V_s, thickness (z), $\mathrm{V}_p/\mathrm{V}_s$, density ($\rho$), and strike and dip.

The predicted RF for that model is then computed using PWAVEQN, a frequency

domain deconvolution using methods of Langston (1979). The RF (observed data in the inversion problem) is calculated using Ammon's time domain iterative deconvolution. Testing has shown that the time domain deconvolution produces the same results for a RF calculated in the frequency domain (John Cassidy, personal communication 2011), therefore the difference of deconvolution methods used in the inversion should have an insignificant effect in the inversion.

Chapter 5

Data and Processing

5.1 NEPTUNE

NEPTUNE (North-East Pacific Time-series Undersea Networked Experiments) is a real-time, cabled offshore observatory that extends from the JdFR to Port Alberni on the west coast of southern Vancouver Island. Currently, NEPTUNE consists of five nodes (table 5.1) which house numerous scientific instruments designed to enlighten scientists in areas such as plate tectonics, subduction dynamics, seabed fluids, climate change and marine ecosystems. Data flows real-time from each instrument to a database at the University of Victoria (UVic) via a seafloor fibre optic cable. The seismic data from these stations is archived at IRIS (Incorporated Research Institutions for Seismology).

NODE	**Location Description**
Folger Passage	Inshore shelf near entrance to Barkley Sound.
ODP889	Mid-Continental slope (North). Rich in gas hydrates.
Barkley Canyon	Submarine canyon on continental slope (South). Rich in gas hydrates and sediments.
ODP1027	Juan de Fuca mid-plate abyssal plain.
Endeavour Ridge	Juan de Fuca ocean spreading centre.

Table 5.1: Locations descriptions of NEPTUNE nodes

Of the five locations, three (ODP89, ODP27 and Barkley Canyon, see figures 1.1 and 2.2) are equipped with Guralp three component, broadband, ocean bottom seismometers (OBS) with a 100 Hz sampling rate. These seismometers are buried ∼70 cm below the seafloor in a caisson filled with glass beads (to simulate sediments on seafloor as shown in figure 5.1c-d). The seismometers are connected to a junction box, which supplies power and transfers data to the UVic shore station at Port Alberni. Due to installation difficulties, instrument malfunctions and human interference, data have not been continuously available since the day of installation to present date. On average in 2010, ∼25% of the data was initially diverted and therefore unavailable. Data were available for this research from January 01, 2010 (table 5.2).

(a) ROPOS (Remotely operated platform for ocean science) delivering seismometer to seafloor.

(b) Seismometer in cassion.

(c) Filling cassion with glass beads.

(d) Completed OBS installation

Figure 5.1: Installation of OBS (from NEPTUNE Canada)

5.2 KECK

In addition to NEPTUNE data, seismic data were collected by an autonomous deployment of two OBSs (identical to NEPTUNE instruments) from 2003–2006 (Wilcock et al., 2007). This deployment was funded by the W.M. Keck foundation and was intended to provide a preliminary evaluation of OBS data in Northern Cascadia. The broadband stations included KEBB, placed just east of the JdFR near the present NEPTUNE Endeavour node, and KXBB, located on the Explorer plate, which is north of and separated from the JdF plate by the Nootka Fault. These OBSs were deployed in the same manner as the NEPTUNE instruments, except buried ∼10 cm shallower in the seabed. Data between August 2004 and September 2005 were provided by William Wilcock from The University of Washington (table 5.2).

5.3 CNSN

The Canadian National Seismograph Network (CNSN) operates over 100 seismographs throughout Canada. Stations OZB and PGC are located on the west coast, and southern tip, respectively, of Vancouver Island and within approximately 100 km north-south and 600 km east of the KECK and NEPTUNE arrays. Data were recorded at both CNSN stations used here by a Guralp broadband seismometer with a 40 Hz sampling rate. Due to their different locations, each has different site conditions and site response.

OZB is a coastal station located on Mount Ozzard near Ucluelet, BC. This seismometer resides on a concrete pad located on hard sediments just above bedrock. Since this is a coastal station, perfect coupling to sediments beneath is not expected and some microseismic noise is recorded at this station. The PGC seismometer is located at the Pacific Geoscience Centre in Sidney, BC. It is housed in an underground

Station	Latitude	Longitude	Elevation(m)	Dates of Data Availability
KXBB	49.50	-129.00	-2370	08/2004–09/2005
KEBB	47.96	-129.13	-2377	08/2004–03/2005
NCBC	48.43	-126.18	-398	01/2010–02/2011
NC27	47.76	-127.76	-2656	10/2010–08/2011
NC89	48.67	-126.85	-1258	01/2010–08/2011
OZB	48.96	-125.49	671	04/1996–08/2011
PGC	48.65	-123.45	5	07/1993–08/2011

Table 5.2: Seismometer Locations and deployment dates

concrete room situated on bedrock.

5.4 Data Quality

As mentioned previously, earthquakes suitable to RF analysis are limited to M6+ teleseismic events with high signal to noise ratio (section 3.1). Together with restricted data availability, these prerequisites limited the number of events that were available for analysis (for more information see appendix A).

Noise in the form of microseisms and infragravity waves was expected to be recorded at OBS stations (Dolenc et al., 2008). Infragravity waves (long period, $\geq$20 s surface waves generated from loading of the ocean floor) and microseisms (high frequency, $\geq$0.1 Hz noise generated from the ocean surface) were observed during previous OBS deployments (Blackman et al., 1995; Laske et al., 2009; Webb, 1992). Previous to the NEPTUNE deployment, Ristau and Rogers (2006) compared the noise on the KECK instruments to that at coastal (OZB) and inland (PNT) seismic stations. Comparing seismic data recorded at the land and OBS stations on a quiet day, the vertical channel of the OBS stations had similar to higher noise than the land stations, and the horizontal components had higher noise levels at periods $\leq$5 s and $\geq$20 s, but lower noise levels for periods between 5 and 20 s. For a noisy day, OBS stations had less noise at periods $\leq$1 s and $\geq$6 s, and similar noise levels between

these periods. Since the first step in RF computation involves deconvolution, a high signal to noise ratio for both the horizontal and vertical components is important. These noise studies preceding the NEPTUNE deployment, hinted that obtaining good quality signals on all channels at the same time could be challenging.

As the water depth and distance to the shore decrease and the amount of soft sediment increases at a station, microseisms and infragravity amplitude increases at the station. Due to these natural factors, KEBB appeared to be the quietest of the OBS stations while NCBC was the noisiest. As expected, the signal at all stations was degraded during the winter when storm swells created the most noise.

Of the six broadband OBS stations deployed in Northern Cascadia, events recorded at KEBB and NC89 are used in this thesis for RF analysis (table 5.3 and figure 5.3a-b). KXBB, NCBC and NC27 did not record any events suitable for RF analysis (see appendix A).

The CNSN stations are permanent land based stations that provide 'good' quality events. The quality of the OZB data was slightly less than that at PGC but of higher quality than was recorded at OBS sites (figure 5.2, appendix A). However, because it has been deployed for many years a sufficient number of useful events were recorded. PGC is a reliable station and had no extended periods of down-time. Events were chosen at these two stations that provided wide BAZ coverage, were as close to 30◦ as possible, had a high signal to noise ratio (figure 5.4–5.8), and produced a deconvolution result with a high measure of fit (table 5.3). Previous studies have shown that having few high quality RFs or many lower quality RFs generally produce similar results (John Cassidy, personal communication 2011).

The azimuthal coverage of the RFs used in this thesis are shown in figure 5.9. All azimuths are reasonably covered with the exception being to the northeast where large earthquakes are rare. Where applicable, similar events (back azimuth (BAZ)

and azimuthal distance (AZ) within 10°) were stacked to optimize the signal to noise ratio.

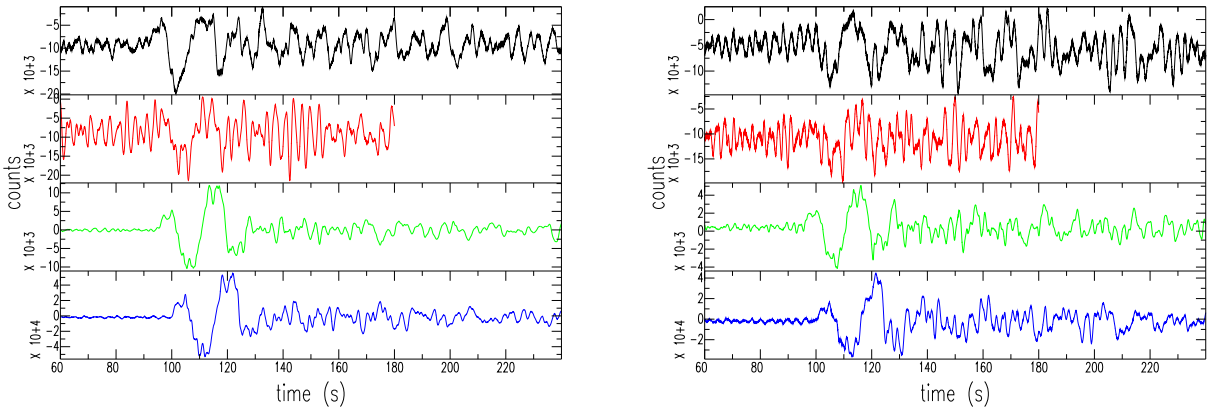

Figure 5.2: Comparison of the same teleseismic event recorded on NC89, NCBC, OZB and PGC. (a) vertical component, (b) horizontal component. Vertical scale is digital counts.

Station	**Julian Date**	**Latitude**	**Longitude**	**Depth(km)**	**Magnitude**	**Fit(%)**	Back Azimuth (°)	Distance (°)
KEBB	2004249	33.070	136.62	14	7.2	90.6	296	69
NC89	2010222	-17.53	168.07	10	7.3	80.0	240	88
OZB	2005164	-19.99	-69.19	11	7.8	97.5	128	85
OZB	2006288	19.88	-155.93	38	6.7	93.1	231	38
OZB	2007150	52.14	157.29	116	6.4	92.1	305	47
OZB	2007253	2.97	-77.96	15	6.8	95.4	122	61
OZB	2008329	54.2	154.32	492	7.3	91.7	308	48
OZB	2009015	46.86	-155.15	36	7.4	97.1	300	51
OZB	2009097	46.05	151.55	31	6.9	90.7	301	53
OZB	2010246	51.45	-175.87	23	6.5	92.3	294	32
OZB	2010355	26.9	143.69	14	7.4	95.9	288	70
OZB	2011175	52.01	-171.86	63	7.3	96.2	293	29
PGC	1997011	18.22	-102.76	33	7.2	98.0	131	44
PGC	2001013	13.05	-88.66	60	7.7	99.0	129	46
PGC	2004249	33.07	126.62	12	7.2	99.0	300	72
PGC	2006288	19.88	-155.93	38	6.7	96.6	234	39
PGC	2010222	17.54	168.07	25	7.3	97.8	266	63
PGC	2005036	16.01	145.87	142	6.6	93.7	281	79
PGC	2007164	13.55	-90.62	23	6.7	97.2	131	44
PGC	2007253	2.97	-77.96	15	6.8	99.0	125	60
PGC	2010355	26.9	143.69	14	7.4	98.3	290	72
PGC	2011070	38.32	142.37	32	9.0	98.3	300	72
PGC	2011097	38.25	141.64	42	7.1	93.9	300	65
PGC	2011113	-10.35	161.23	82	6.8	95.0	252	88
PGC	2011130	-20.25	168.28	15	6.8	97.9	241	92

Table 5.3: Teleseisms used to compute RFs.

5.5 Processing

Raw data for the OBS stations were obtained and converted to SAC (Seismic Analysis Code) using ANTELOPE, while data from the CNSN stations were downloaded from IRIS. For all stations, initial processing was done in SAC. The horizontal components were first rotated into radial and transverse components. The mean and linear trends were then removed, and the ends were tapered. Since broadband seismometers have such a high sampling rate, waveforms also needed to be decimated so that the number of points was less than the maximum allowable in the inversion routine. Data from the CNSN stations were decimated by a factor of two and OBS stations by four, so that the resulting sampling rates were 20 HZ and 25 Hz, respectively. At OBS stations which had obvious interference from infragravity waves (figure 5.3a), a high pass filter was applied. For all inversions a filtering parameter, α, of 5 was used. Other α values were investigated, but no significant difference was observed.

An important processing factor is the length of recording time that was used, both in calculating the RF and inverting the RF. For calculating the RF, start and end times were chosen as near to zero crossings as possible. For each event, RF's were calculated using varying lengths of time (deconvolution window). The length of deconvolution window used was one that produced a consistent RF compared to others.

When choosing the inversion length it was important to consider the predicted crustal structure, as well as the limitations of the forward model. The forward model used produces only free surface multiples. As record length increases so does the possibility of recording arrivals that are a product of internal multiples. For the OBS stations, multiples of water reverberations will also be introduced that can not be modelled. However, P waves that travel from the station and are reflected off the water surface to be recorded at the OBS should not be a concern, as they are contained in the vertical component seismogram whose effect is removed from the radial RF. Beneath the CNSN stations there is dipping structure. Multiples from dipping structure are complicated to predict and therefore inversion windows are chosen so that few multiples are included.

At each station, the inversion window began one second before the direct P wave arrival and extended to the end of reasonable predicted arrivals. The length of the inversion window therefore varied by station. The window lengths used were 4 s, 6 s, 6 s and 8 s for KEBB, NC89, OZB, and PGC (respectively). Any figures included in the results section showing the observed RF depict the length of the RF used in that particular inversion.

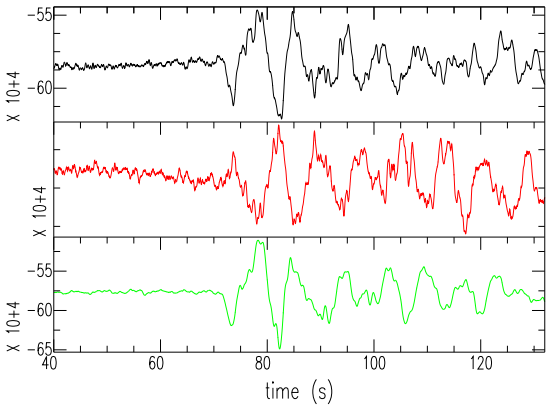

(a) KEBB 2004249

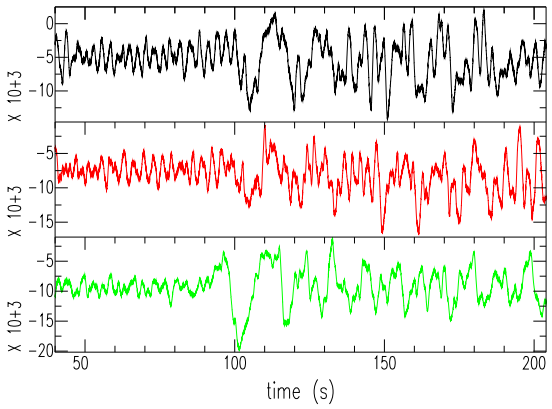

(b) NC89 2010222

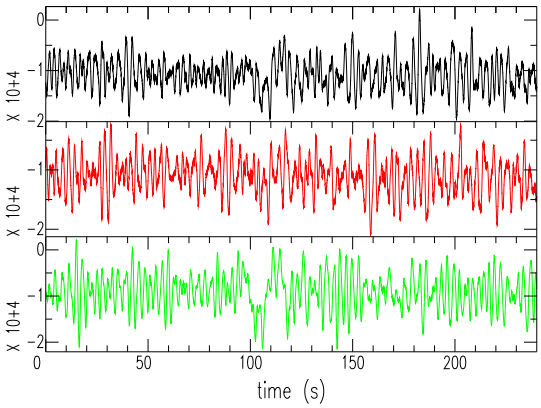

(c) NCBC 2010222

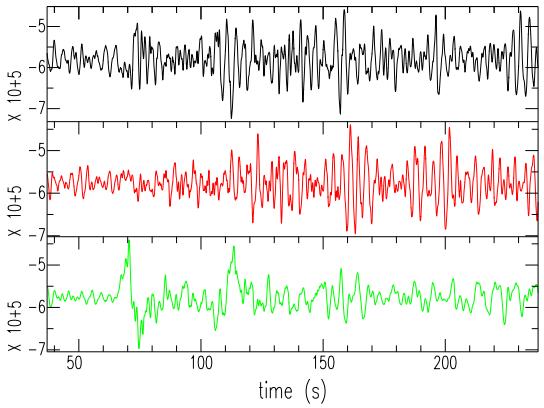

(d) KXBB 2005164

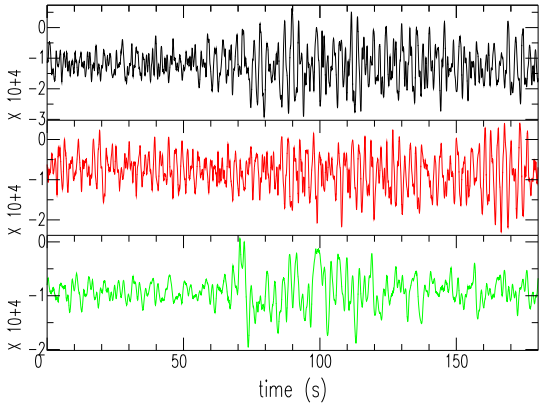

(e) NC27 2011097

Figure 5.3: Raw Data from OBS stations. NC89 and KEBB were used, NC27, NCBC and KXBB were not. Black, red and green waveforms represent E-W, N-S and Z components, respectively. Vertical scale is digital counts.

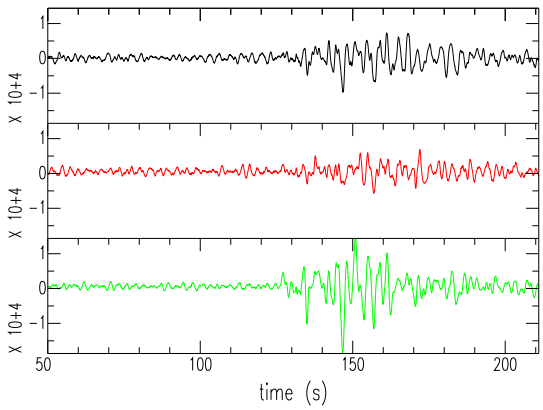

(a) OZB 2006288

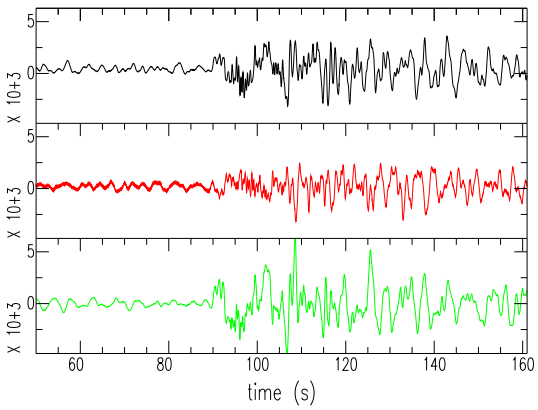

(b) OZB 2010246

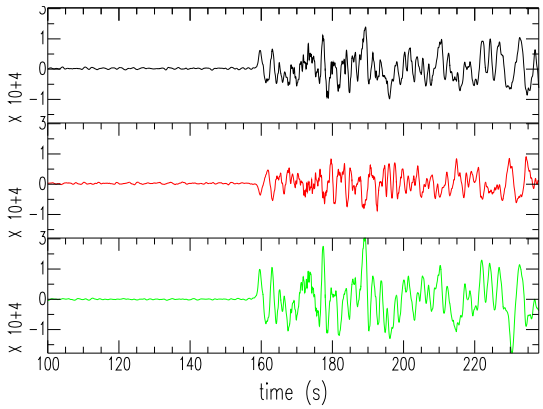

(c) OZB 2011175

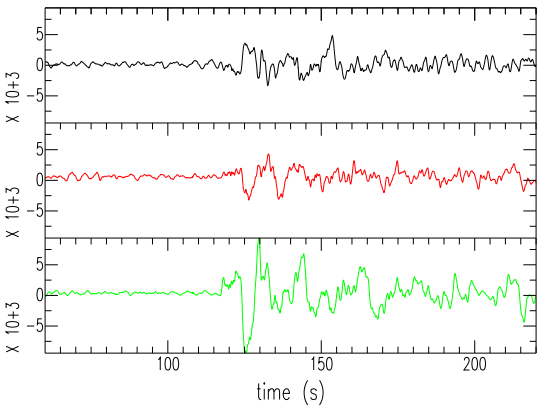

(d) OZB 2007253

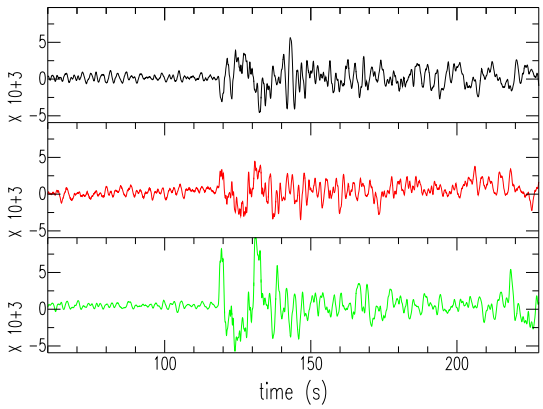

(e) OZB 2005164

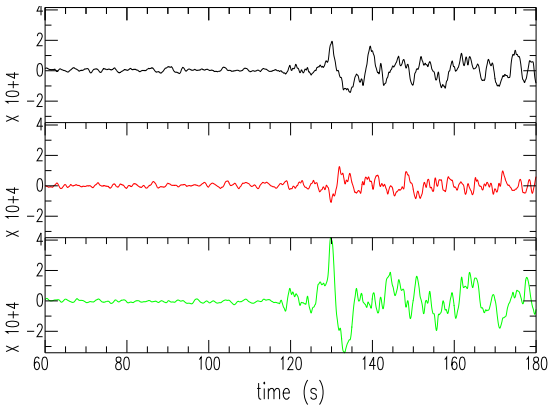

(f) OZB 2010355

Figure 5.4: Raw data from events used from station OZB. Black, red and green waveforms represent E-W, N-S and Z components, respectively. Vertical scale is digital counts.

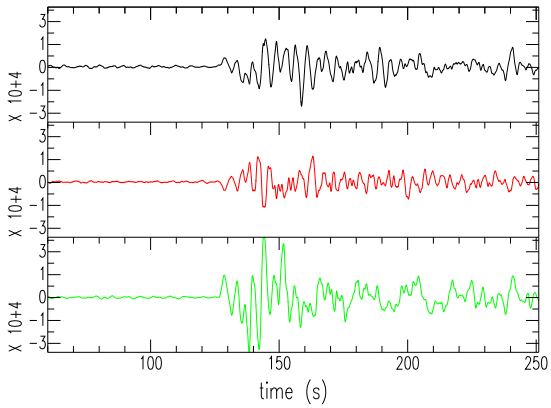

(a) OZB 2009015

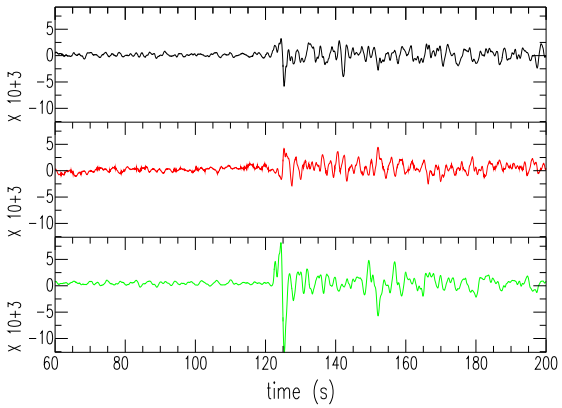

(b) OZB 2007150

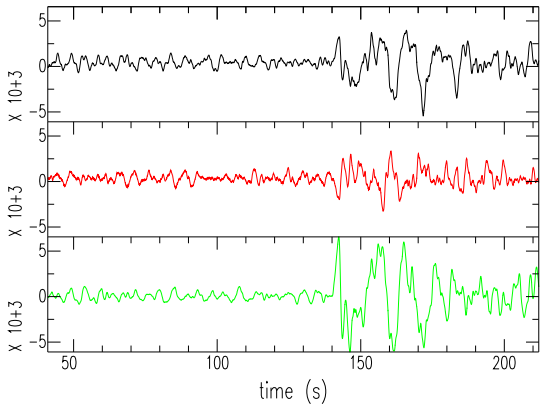

(c) OZB 2009097

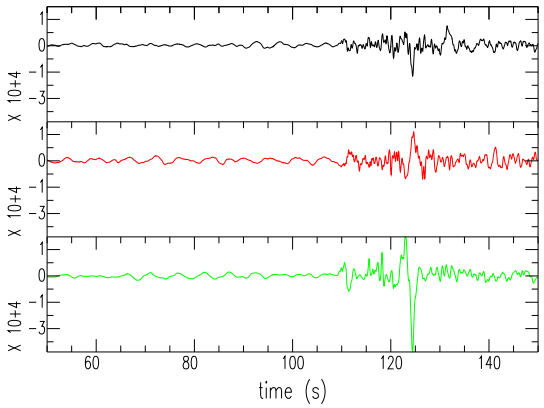

(d) OZB 2008329

Figure 5.5: Raw data from events used from station OZB (continued). Black, red and green waveforms represent E-W, N-S and Z components, respectively. Vertical scale is digital counts.

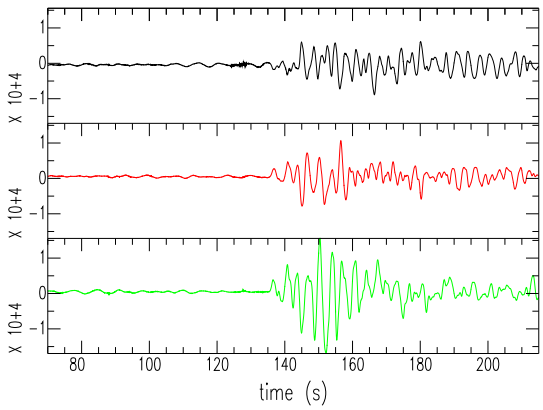

(a) PGC 1997011

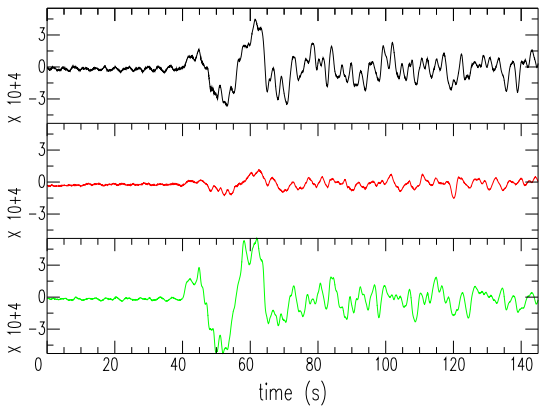

(b) PGC 2010222

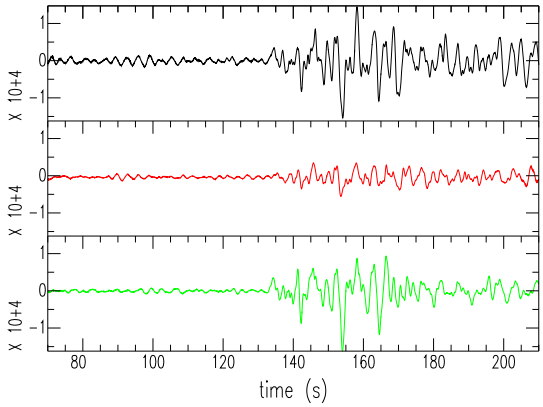

(c) PGC 2006288

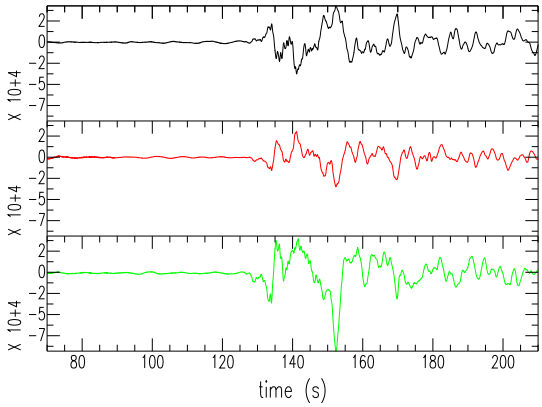

(d) PGC 2001013

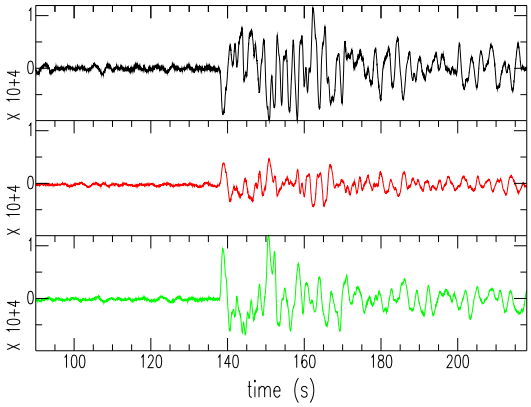

(e) PGC 2007164

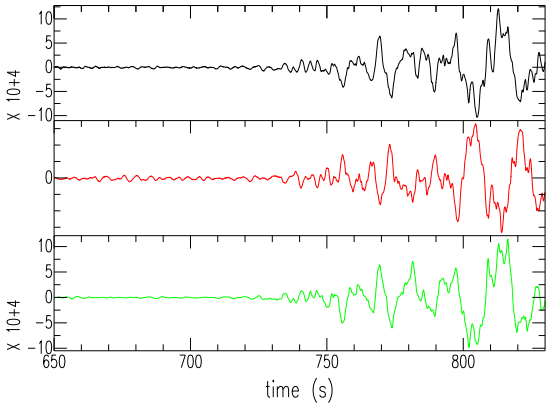

(f) PGC 2011070

Figure 5.6: Raw data from events used from station PGC. Black, red and green waveforms represent E-W, N-S and Z components, respectively. Vertical scale is digital counts.

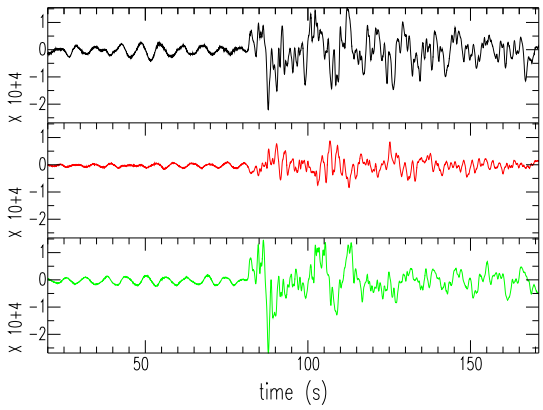

(a) PGC 2011097

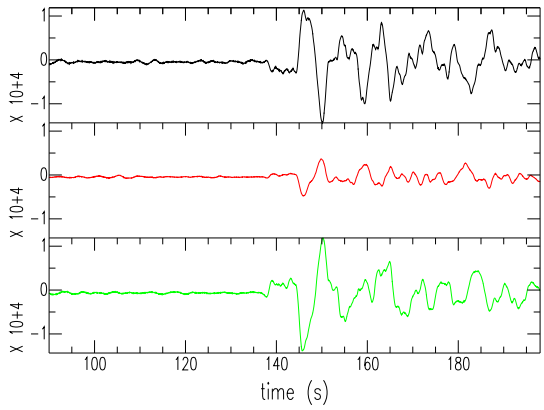

(b) PGC 2007253

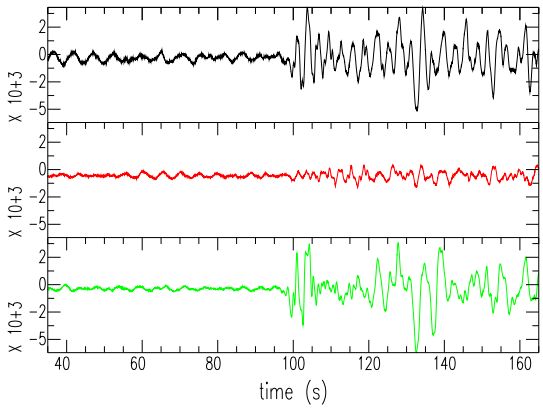

(c) PGC 2011113

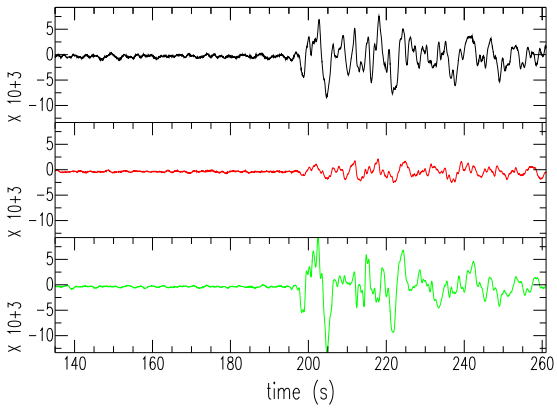

(d) PGC 2011130

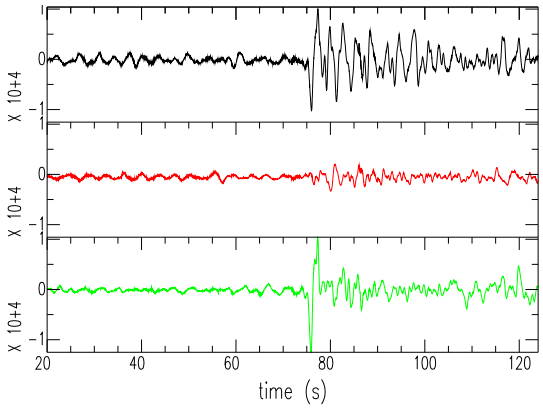

(e) PGC 2005036

Figure 5.7: Raw data from events used from station PGC (continued). Black, red and green waveforms represent E-W, N-S and Z components, respectively. Vertical scale is digital counts.

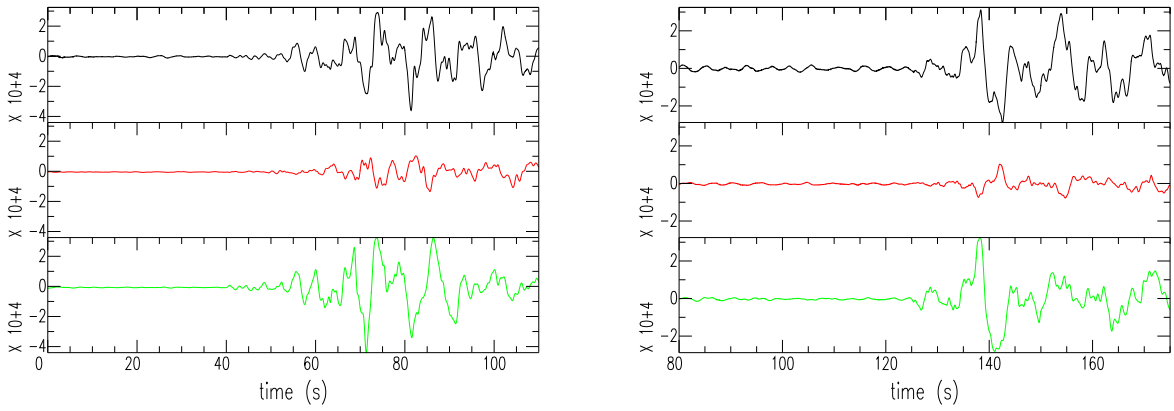

(a) PGC 2004249 (b) PGC 2010355

Figure 5.8: Raw data from events used from station PGC (continued). Black, red and green waveforms represent E-W, N-S and Z components, respectively. Vertical scale is digital counts.

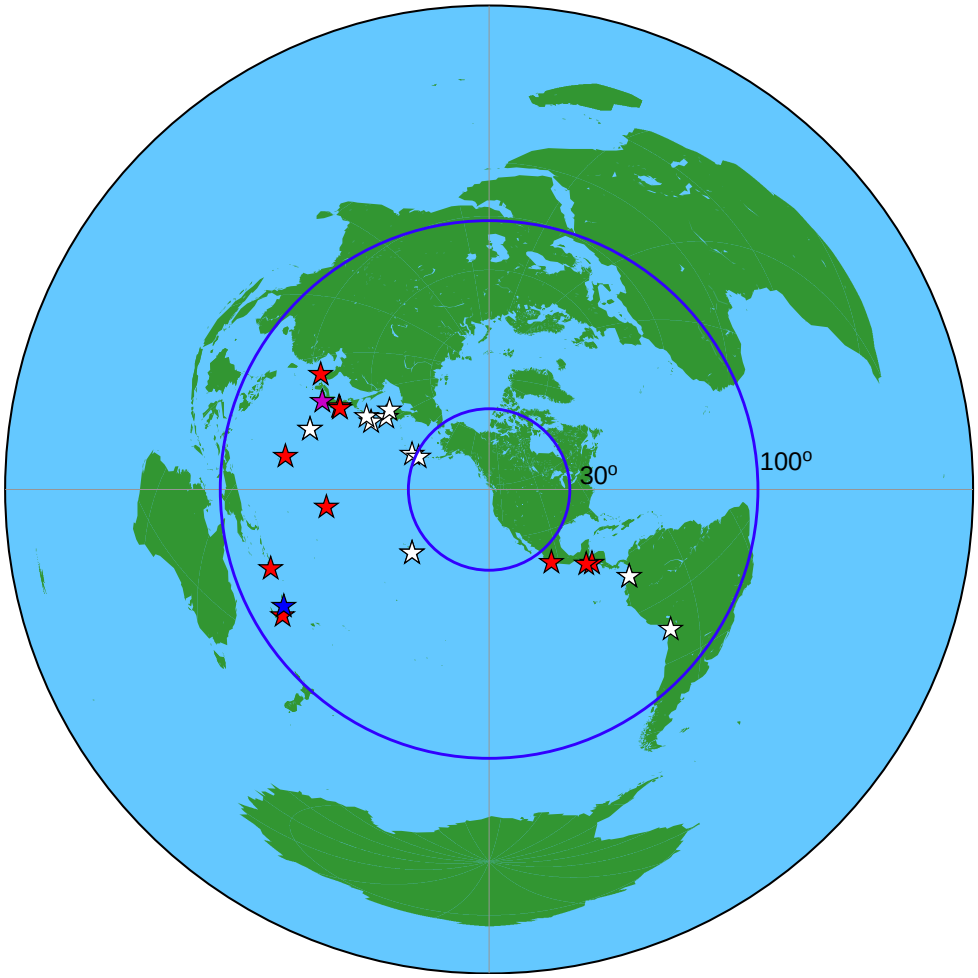

Figure 5.9: Location of Teleseisms (stars) used from each station (white=OZB, red=PGC, blue=NC89, purple=KEBB).

Chapter 6

Receiver Function Inversion Results

This chapter presents results of the Bayesian RF inversion for the four stations included in this thesis. The results are interpreted in the following chapter.

6.1 OZB

OZB is a relatively quiet CNSN station on the west coast of Vancouver Island (figure 2.2). This seismometer was deployed in 1996 providing data over a much longer period of time than the seafloor stations. Ten 'good quality' teleseismic events were collected over this time period for varying BAZ (table 5.3, figure 5.9). Stacking RFs from BAZ within 10° improved the signal to noise ratio. RFs with differing BAZ supplied the information required to invert for strike and dip, as well as V_s, Z, V_p/V_s and ρ. The *a priori* information at both CNSN stations is based on a collection of previous studies from Cassidy and Ellis (1993), Hyndman et al. (1990), Calvert (2004), Calvert et al. (2011), Ramachandran et al. (2006), Nedimovic et al. (2003) and Nicholson et al. (2005). Parameter ranges for each layer had bounds of 2 km/s $\leq V_s \leq$ 5.0 km/s, 1.0

km $\leq Z \leq$ 15 km, $1.65 \leq V_p/V_s \leq 1.9$, $-60° \leq$ strike $\leq 10°$, $0° \leq$ dip $\leq 20°$ and 2.5 g/cm^3 $\leq \rho \leq$ 3.5 g/cm^3. A minimum lower bound of 3.0 km/s was applied to V_s of the half space. As well, the surface layer was constrained to have zero strike and dip, while the bottom layer and half space were forced to have identical strike and dip (from assumptions that the last layer and half space represent the JdF plate).

Initially, a BIC study was carried out at this station assuming IID data errors with unknown standard deviation σ. For models comprised of six to nine layers a time window of 6 seconds (1 s before and 5 s after the direct P wave arrival) of all RFs (six in total) were inverted simultaneously to find the optimum model for each parametrization (figure 6.1). The minimum BIC value corresponded to an eight layer model (figure 6.2). This model and the resulting RFs are shown in figure 6.3 along with velocity profiles determined by Nicholson et al. (2005) via RF inversion of data recorded on the Polaris array.

Having multiple RFs allowed a meaningful estimate of the data error statistics at this station. Residuals were calculated between the observed RF and the RF predicted for the MAP model for each BAZ which were then used to estimate the data covariance matrix, $\mathbf{C_d}$, (figure 6.4) as described in section 4.6. The improvement realized by including the estimated covariance matrix in the inversion is illustrated in figure 6.5, which shows histograms and autocorrelation functions for the raw residuals $\mathbf{r}$ and standardized residuals $\mathbf{C_d}^{-1/2}\mathbf{r}$, as well as p values for the KS and runs tests. The left column of figure 6.5 shows the histogram for the standardized residuals closely resembles a Gaussian distribution, while that for raw residuals does not. Further, the standardized residuals pass the KS test with a p value of 0.57 while the raw residuals fail with a p value of 4.9×10^{-25}. The right column of figure 6.5 shows that including the covariance matrix results in a much tighter autocorrelation peak with less evidence of correlated structure, although both raw and standardized residuals fail the runs

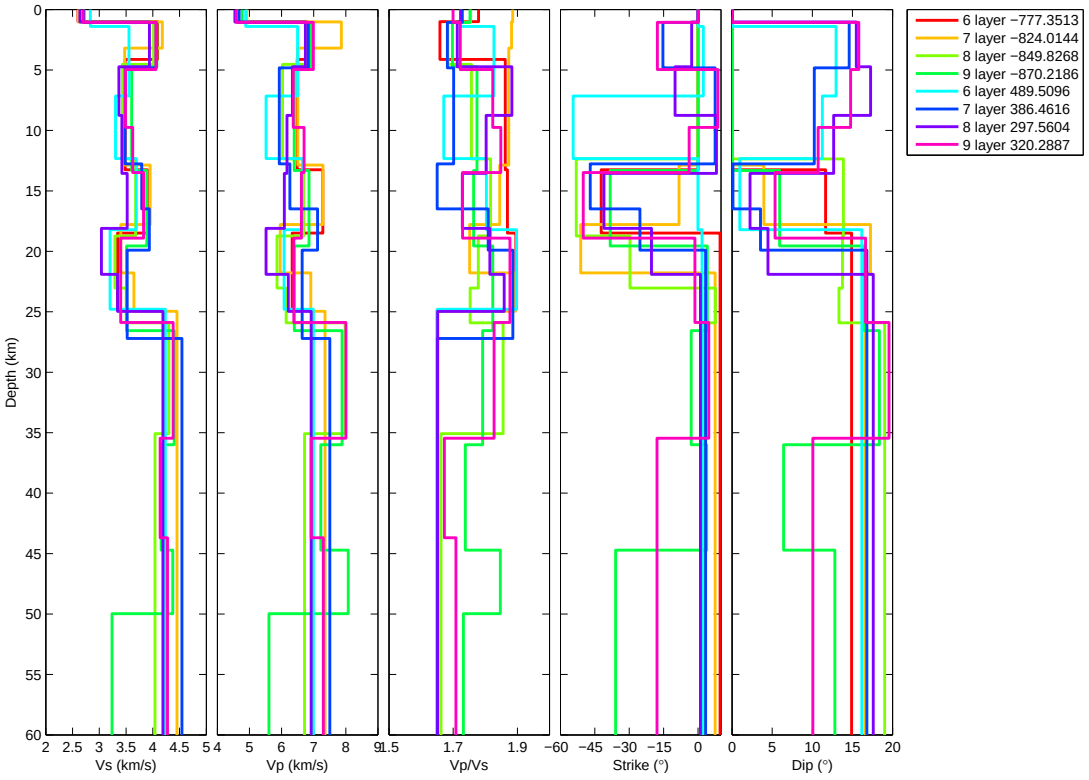

Figure 6.1: OZB optimal models computed for the BIC study. Each legend entry indicates the number of layers and the accompanying misfit. Negative misfits correspond to inversions assuming unknown σ; positive misfits correspond to inversion with estimated covariance matrix.

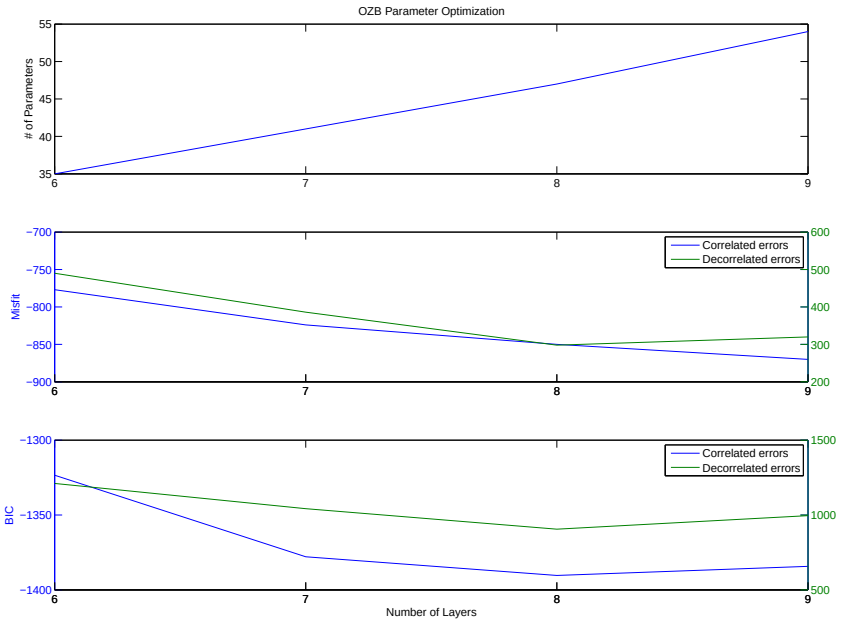

Figure 6.2: OZB BIC study.

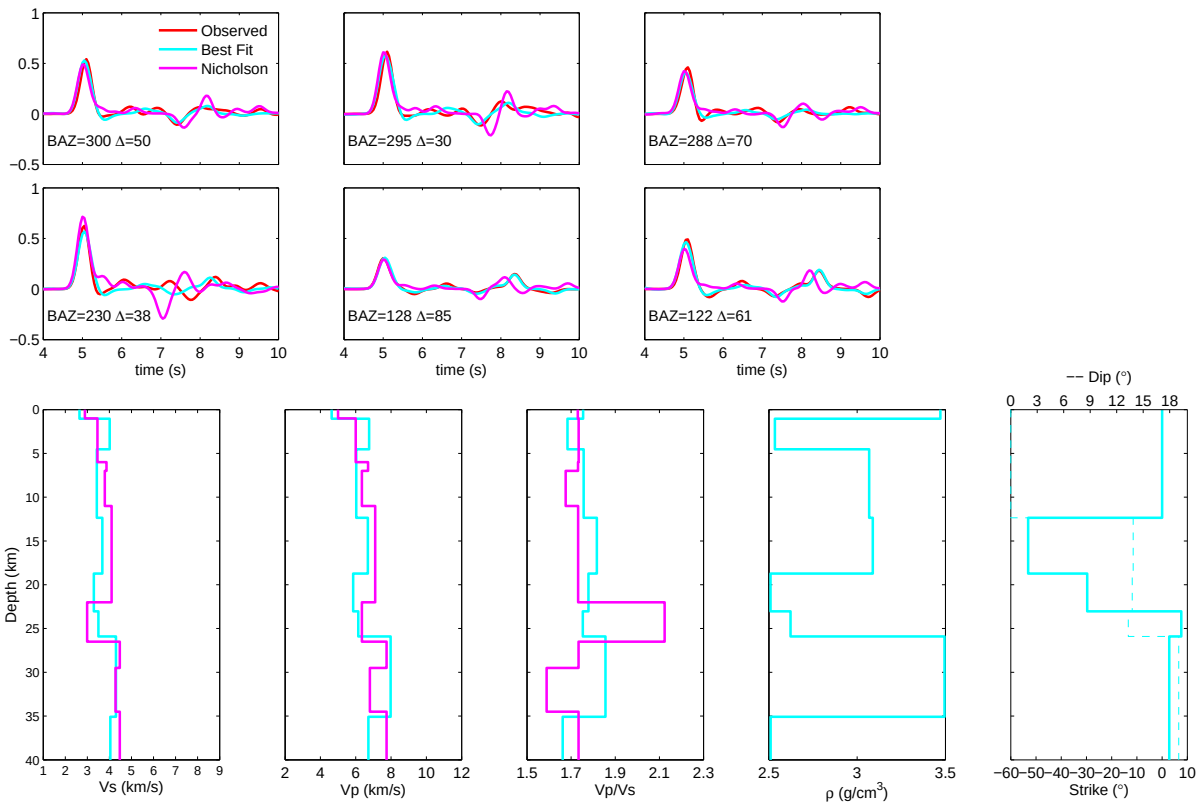

Figure 6.3: OZB optimal model and corresponding radial RFs from inversion with unknown IID data errors. Results from Nicholson et al. (2005) are included for comparison.

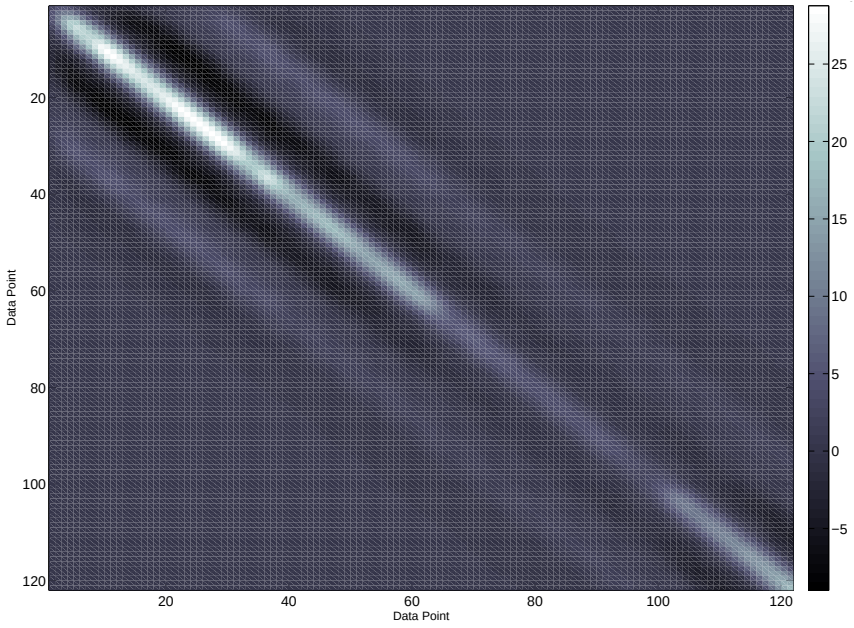

Figure 6.4: Data covariance matrix estimated for OZB.

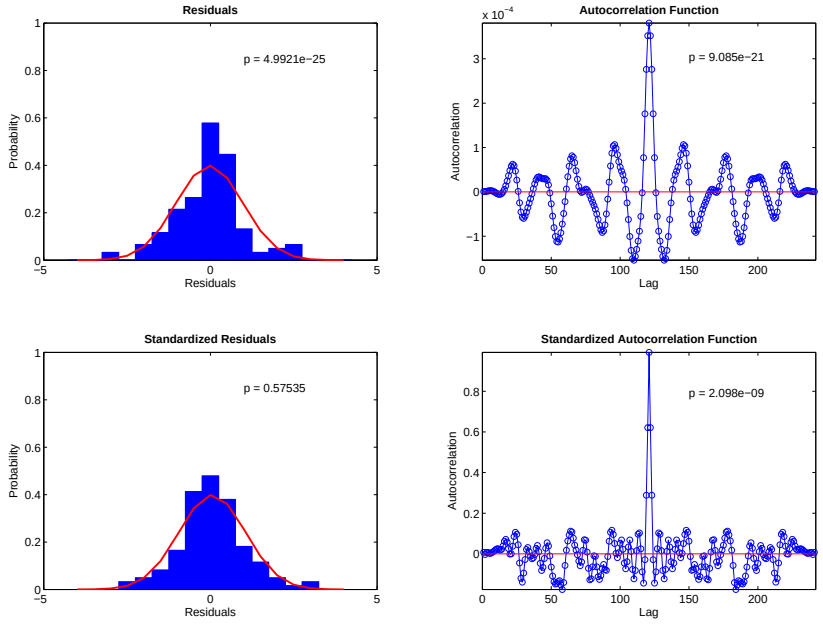

Figure 6.5: OZB statistical tests to validate Gaussianity and randomness. The top panels represent raw residuals, while the bottom panels are the standardized residuals decorrelated by the $\mathbf{C_d}$ estimated from a RF in the NW quadrant (BAZ = 300°). The red line is a standard Gaussian distribution.

test.

Following the initial BIC study, which assumed IID errors, a second BIC study was carried out which included the estimated $\mathbf{C_d}$ in the optimization. This step was carried out to validate the initial BIC choice of eight layers and to determine a model which would be used as a starting point for MHS. With the inclusion of $\mathbf{C_d}$ an eight layer model was also indicated as the optimum parametrization for this dataset (figure 6.2). This parametrization is similar to the arbitrarily chosen nine layer model used by Nicholson et al. (2005). The result of the BIC study implies that this dataset does not support more than eight layers. Using more than that may add unconstrained parameters, while using less would not represent the RF as effectively as possible and model structure could be missed. The optimum model when $\mathbf{C_d}$ was included is shown in figure 6.6.

The complexity of this inversion problem introduced computational challenges. The simultaneous inversion of six RFs meant that six RFs needed to be forward modelled at each step to calculate the misfit. This, along with the number of parameters (47), slowed the inversion process such that one computer processor was capable of generating only ∼400 models/day. To achieve a reasonable sampling (∼30000 models) in practical time, MHS was run in parallel on five processors and the results combined.

The PPD sampling achieved by MHS is illustrated in figure 6.7 in terms of one dimensional marginal probability distributions for each parameter. The distributions are smooth and appear well sampled. The parameters which defines the V_s profile (V_s and Z) are well resolved within their prior bounds, indicating these parameters are well constrained by the data (i.e., the model is not over-parametrized). Marginal PPDs for some layer thicknesses (Z) are multi-modal, indicating strong non-linearity of the inverse problem. The other parameters are generally reasonably well resolved,

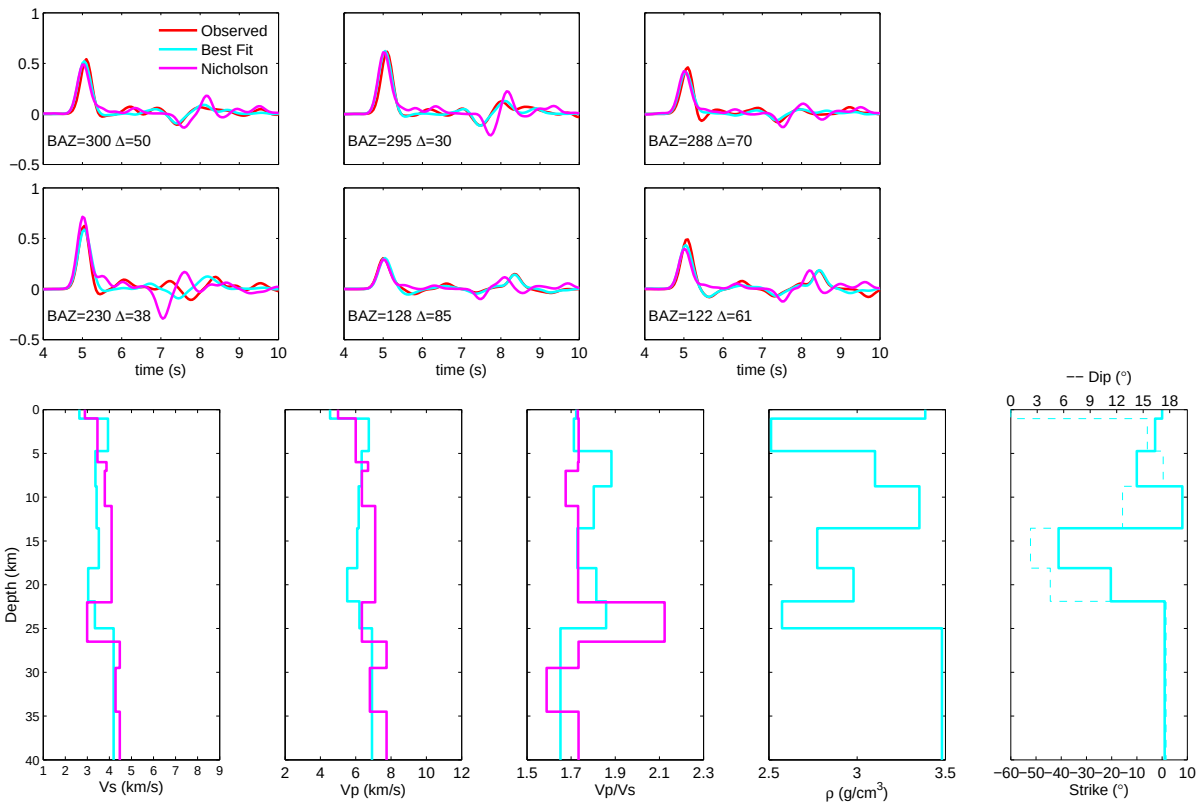

Figure 6.6: OZB optimal model and corresponding radial RFs from inversion with estimated data covariance, $\mathbf{C_d}$. Results from Nicholson et al. (2005) are included for comparison.

with some multi-modal distributions. One dimensional marginals show probability distributions for individual parameters with the effects of all other parameters integrated out. To investigate inter-parameter relationships, the correlation matrix is shown in figure 6.8. This figure indicates many significant correlations, positive and negative, between parameters. In particular, V_s parameters of neighbouring layers are generally positively correlated, V_s and Z for a given layer are negatively correlated, and V_s and ρ for a given layer are weakly negatively correlated. Parameter inter-relationships can be further examined in terms of joint marginals, as shown in figure 6.9 for selected parameters. These joint marginals confirm the negative correlations between V_s and Z for layer 2, as well as the positive correlation between V_s parameters of layers 5 and 6. The multi-model nature of Z in layers 4 and 5, observed in the one dimensional distributions, is also indicated in the joint distributions.

To illustrate the inversion results in a more intuitive and useful format, figure 6.10 shows marginal probability profiles for the parameters of the eight layer model, computed by summing (integrating) the PPD samples onto a depth-dependent grid. This figure shows interface probabilities as a function of depth, marginal probability profiles for all inversion parameters, as well as for V_p (product of V_s and V_p/V_s), normalized at each depth individually for display purposes. As expected, V_s is the best constrained property, while all other parameters are less constrained. Some multi-modal behaviour is indicated for V_p/V_s and hence V_p. Figure 6.11 shows the same marginal profiles normalized over all depths (i.e., true probabilities). These results are discussed further in the following chapter.

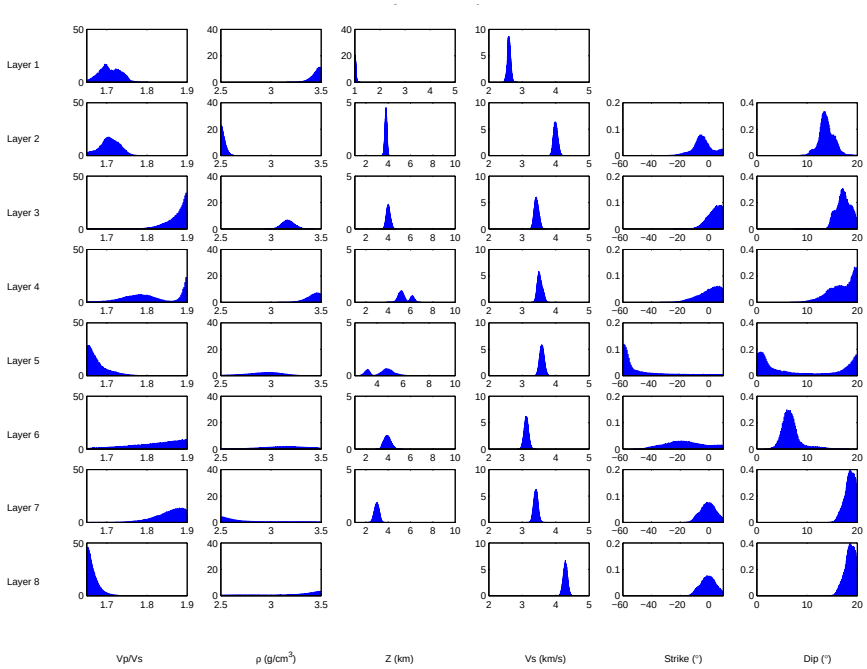

Figure 6.7: OZB marginal probability distributions for all parameters. Note the half space does not have a layer thickness or, consequently, a marginal distribution.

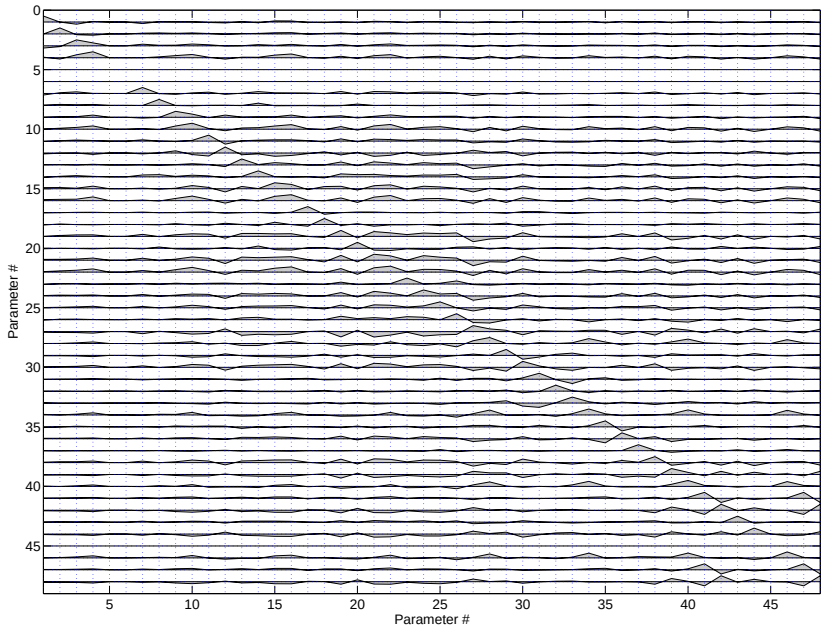

Figure 6.8: OZB parameter correlations. For layers 1,2,3, ..., 8, parameters 1, 7, 13, ..., 37 correspond to V_p/V_s; 2, 8, 14, ..., 38 to ρ; 3, 9, 15, ..., 39 to Z; 4, 10, 16, ..., to V_s; 5, 11, 17, ..., 41 to the strike and 6, 12, 18, ...,42 to dip.

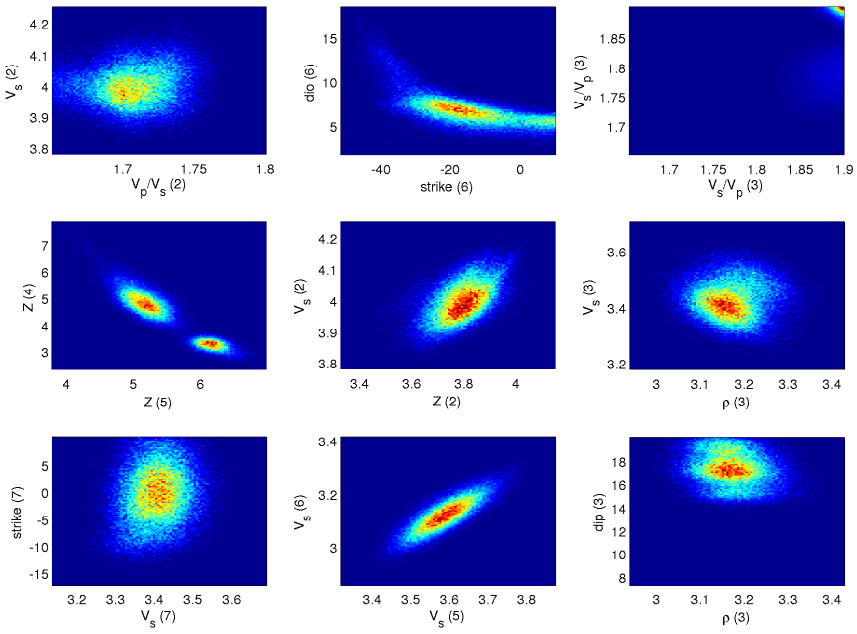

Figure 6.9: OZB joint probability distributions for select parameters and the layer they represent in parenthesis.

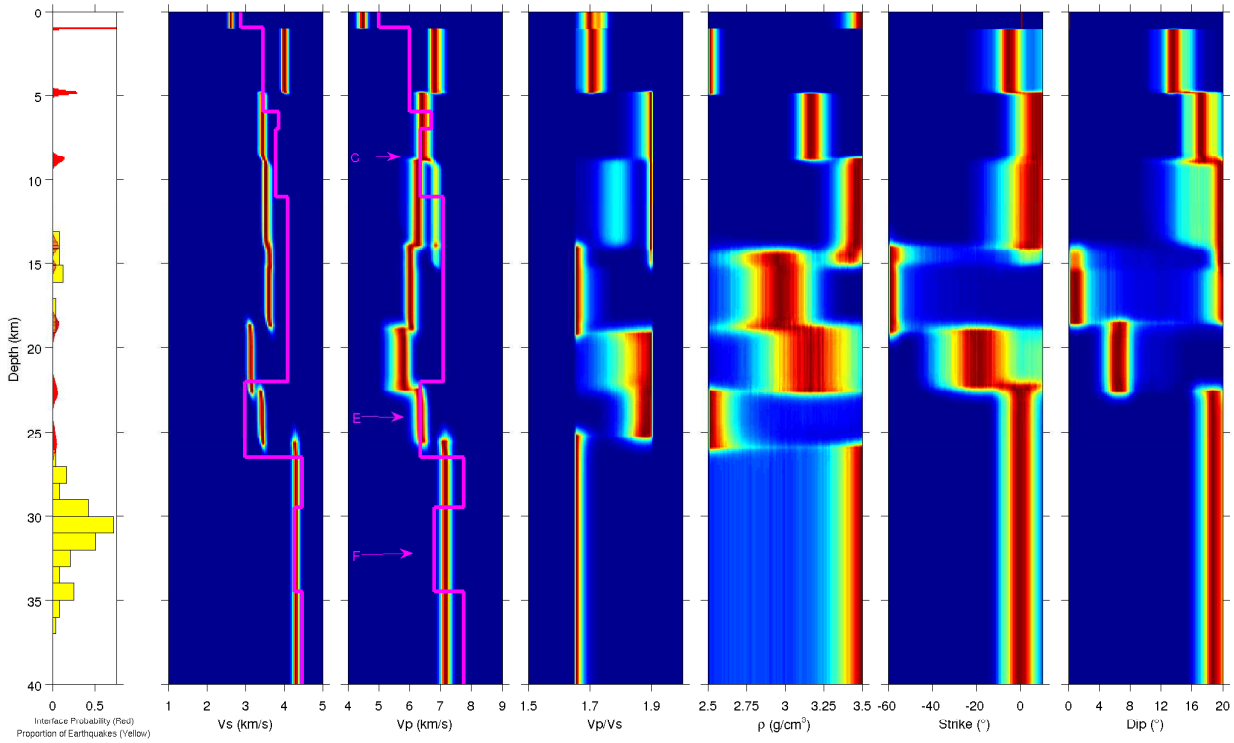

Figure 6.10: Bayesian inversion results for OZB. Interface probability and depth of earthquakes within 10 km of OZB (left-most), and marginal probability profiles (normalized at each depth) of all parameters. Hot colours represent areas of high probability, cool colours represent low probability. The pink lines and labels represent velocity profiles and interpretation of the C, E, and F layers obtained from previous RF analysis ∼100km south of by Nicholson et al. (2005).

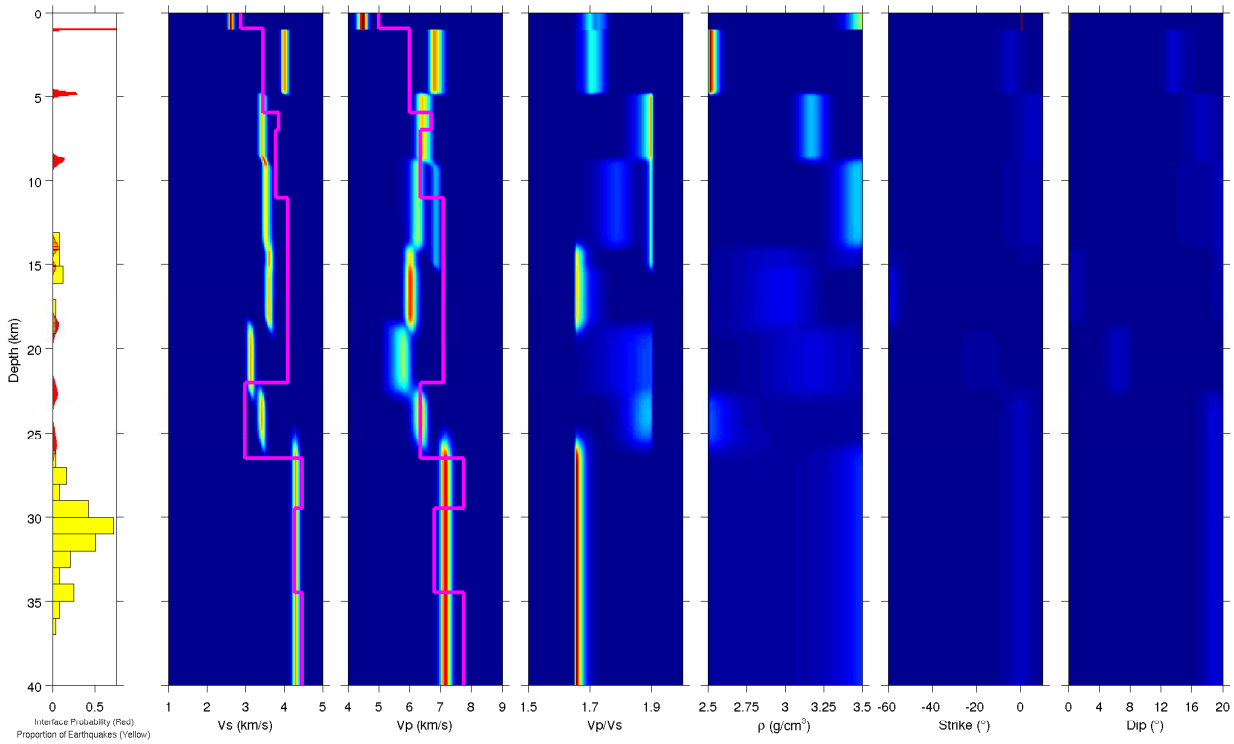

Figure 6.11: Bayesian inversion results for OZB. Interface probability and depth of earthquakes within 10 km of OZB (left-most), and marginal probability profiles of all parameters. Hot colours represent areas of high probability, cool colours represent low probability. The pink lines and labels represent velocity profiles and interpretation of the C, E, and F layers obtained from previous RF analysis ∼100km south of OZB by Nicholson et al. (2005).

6.2 PGC

PGC, located at the Pacific Geoscience Centre in Sidney, BC (figure 2.2) is the longest running station used in this study and had the best quality events. At this station 13 teleseismic events were stacked into seven RFs used in the inversion. The targeted interface (oceanic Moho) is expected to be at a greater depth than at OZB, therefore a longer time window of data was used in the inversion at this station. The same parameters that were considered at OZB were inverted for at PGC. The prior bounds differed from those at OZB only in that any layer whose top interface was at a depth less than 10 km was set to have a strike and dip of 0°, to constrain the inversion to expected values based on prior studies (Cassidy, 1992; Nicholson et al., 2005).

The BIC study with unknown and estimated data errors both resulted in the lowest BIC for a seven layer model (figures 6.12 and 6.13). The optimum model derived using unknown data errors (figure 6.14) was used to estimate the data covariance matrix, $\mathbf{C_d}$ (figure 6.15). The autocorrelation function of the standardized residuals (figure 6.16) shows a narrow peak, indicating reasonably well decorrelated residuals, although the runs test fails. The p value of 0.23 indicates that the standardized residuals are Gaussian distributed (figure 6.16). The optimum model (figure 6.17) determined using ASSA with $\mathbf{C_d}$ was used a the starting point for MHS.

MHS was conducted for this station using the same method as was used at OZB. The final sample consisted of 35000 samples and is shown in the marginal profiles in figure 6.19 and normalized marginal profiles in figure 6.18. Similar to OZB, correlations and dependencies exist between parameters, although they are not illustrated here.

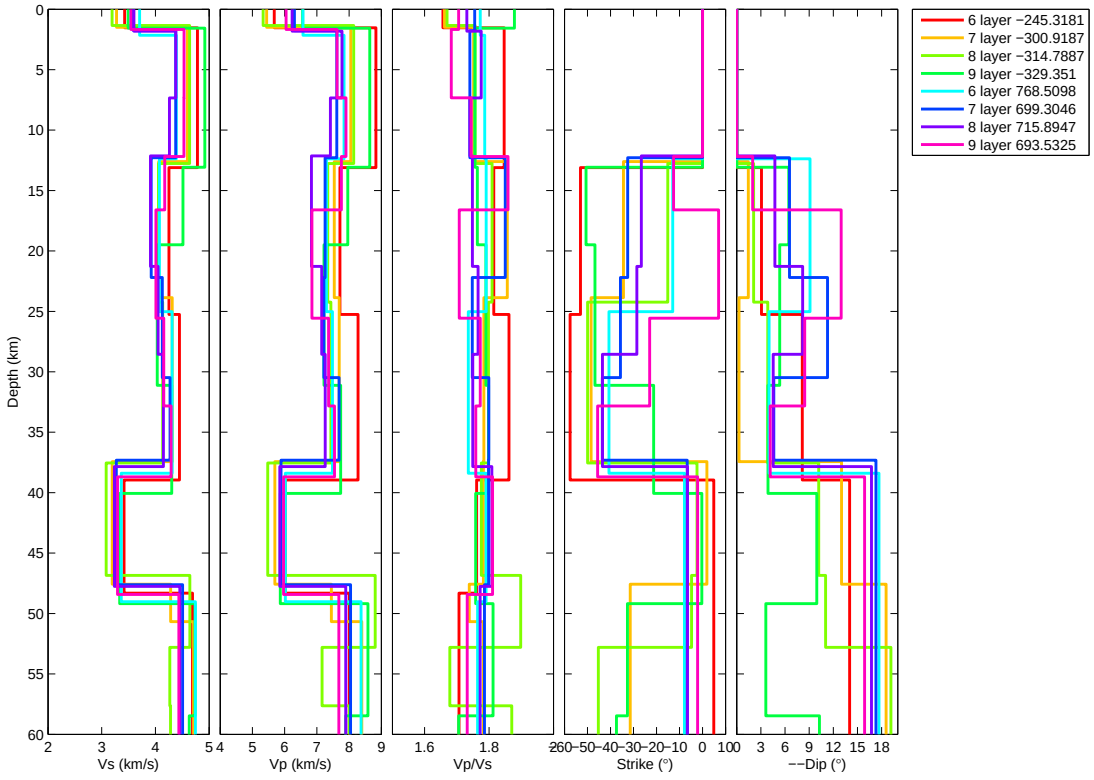

Figure 6.12: PGC optimal models computed for the BIC study. Each legend entry indicates the number of layers and the accompanying misfit. Negative misfits correspond to inversions assuming unknown σ; positive misfits correspond to inversion with estimated covariance matrix.

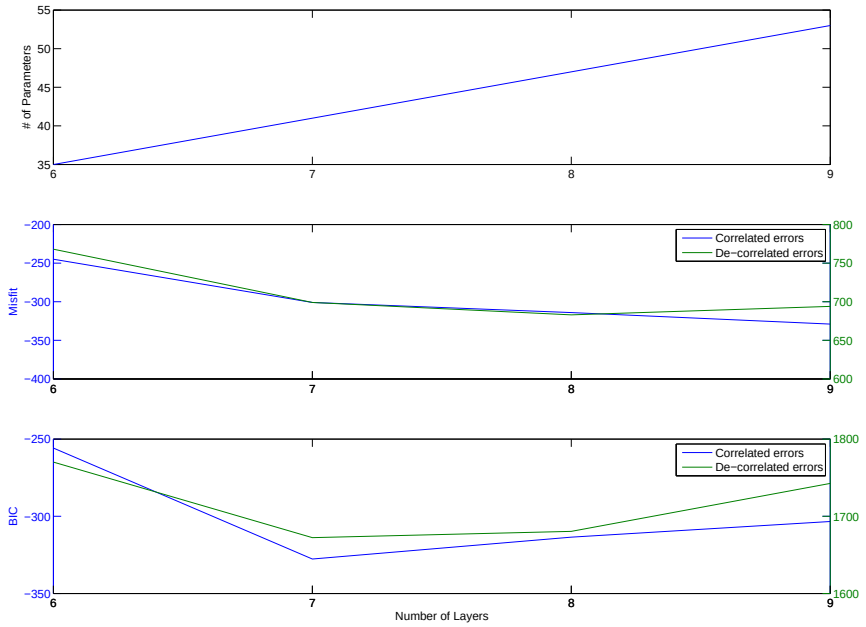

Figure 6.13: PGC BIC study

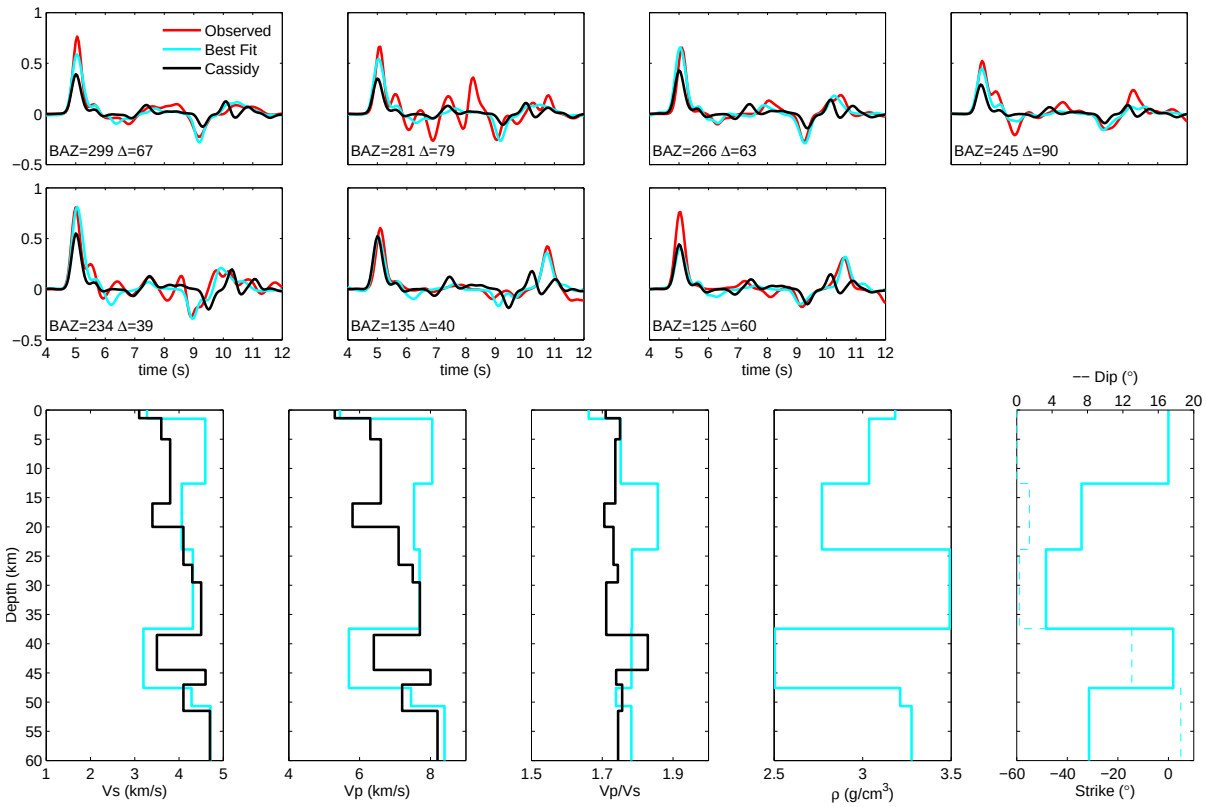

Figure 6.14: PGC optimal model and corresponding radial RFs from inversion with unknown IID data errors. Results from Cassidy and Ellis (1993) are included for comparison.

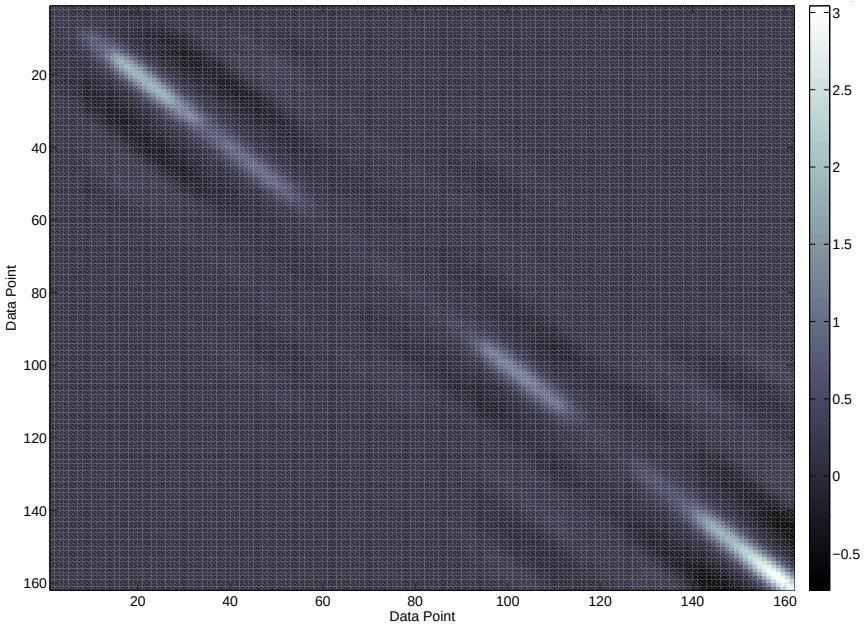

Figure 6.15: Data covariance matrix estimated for PGC.

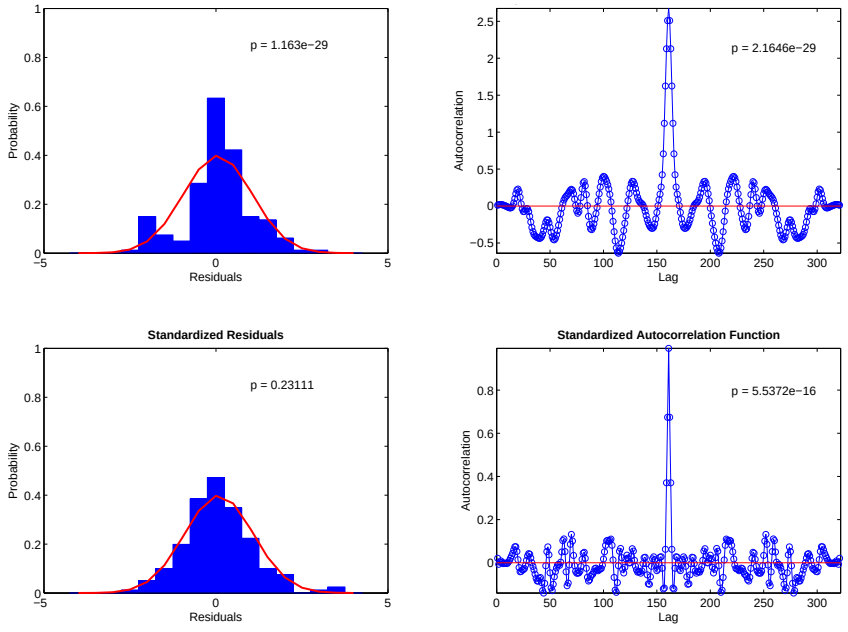

Figure 6.16: PGC statistical tests to validate Gaussianity and randomness. The top panels represent raw residuals, while the bottom panels are the standardized residuals decorrelated by the $\mathbf{C_d}$ estimated from a RF in the SE quadrant (BAZ = 135°). The red line is a standard Gaussian distribution.

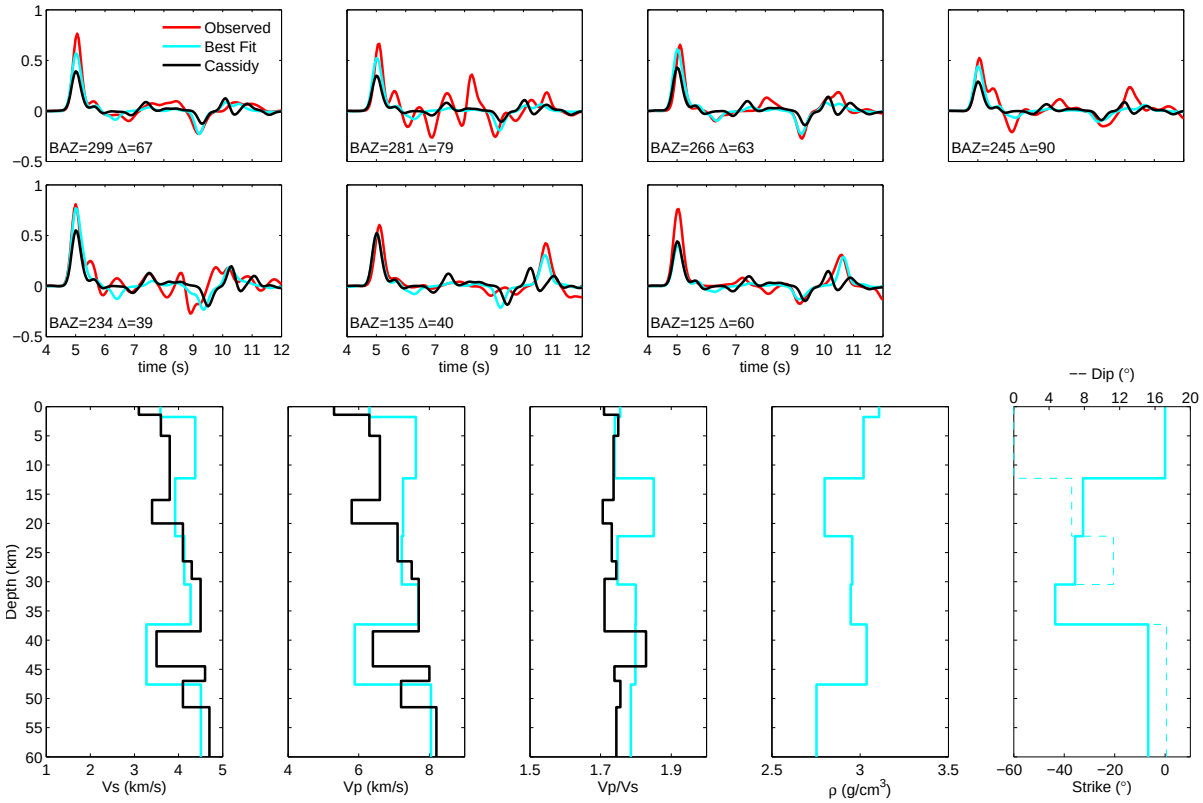

Figure 6.17: PGC optimal model and corresponding radial RFs from inversion with estimated data covariance, $\mathbf{C_d}$. Results from Cassidy and Ellis (1993) are included for comparison.

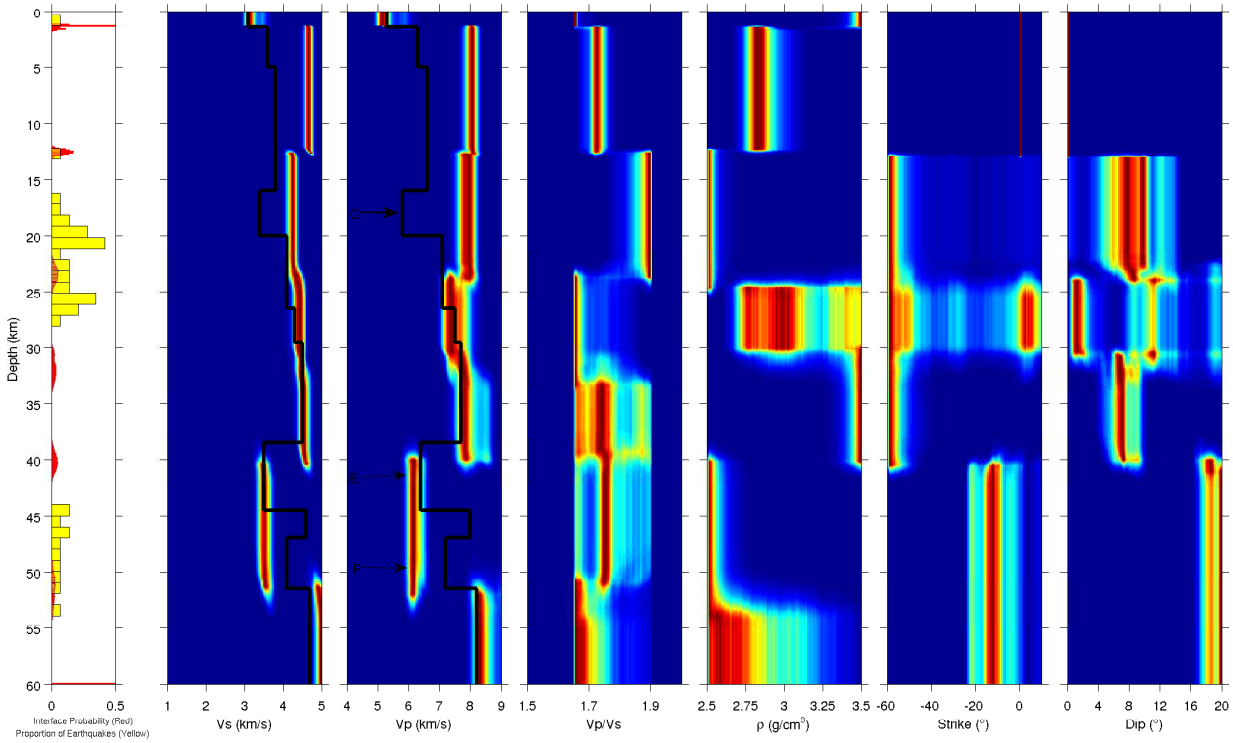

Figure 6.18: Bayesian inversion results for PGC. Interface probability and depth of earthquakes within 10 km of PGC (left-most), and marginal probability profiles (normalized at each depth) of all parameters. Hot colours represent areas of high probability, cool colours represent low probability. The black lines and labels represent velocity profiles and interpretation of the C, E, and F layers obtained from previous RF analysis at PGC by Cassidy and Ellis (1993).

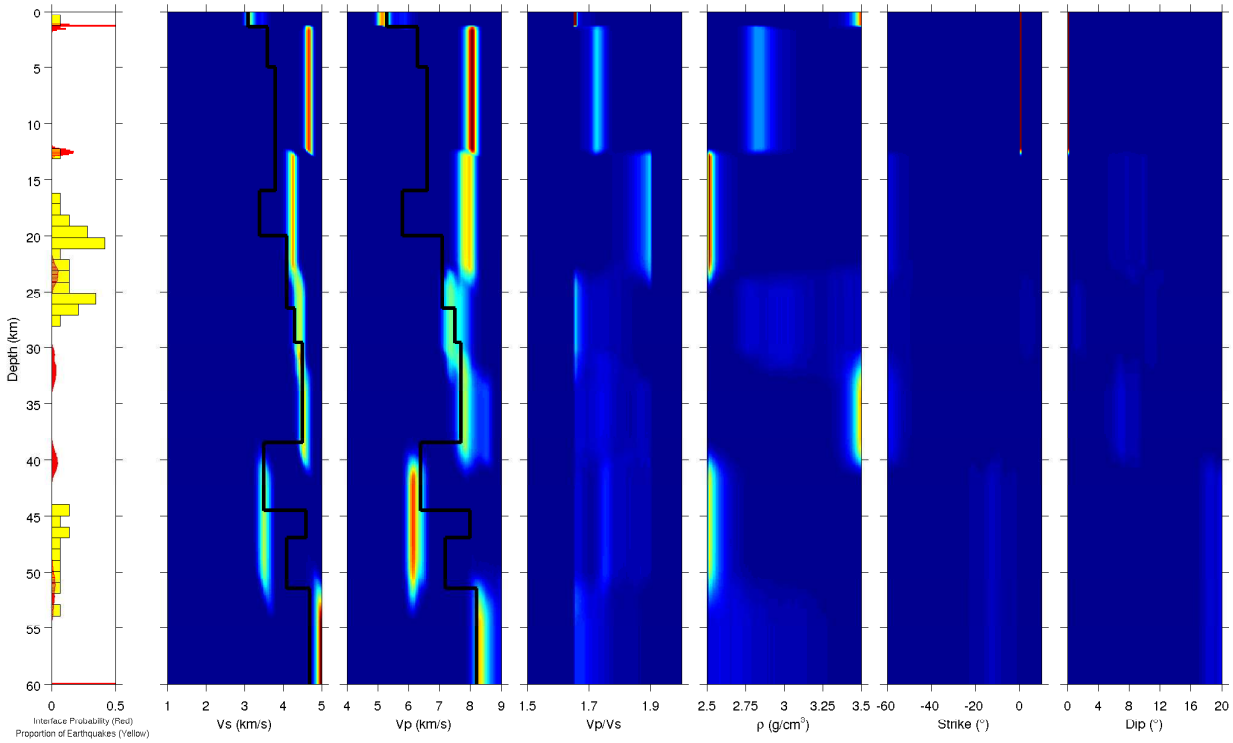

Figure 6.19: Bayesian inversion results for PGC. Interface probability and depth of earthquakes within 10 km of PGC (left-most), and marginal probability profiles of all parameters. Hot colours represent areas of high probability, cool colours represent low probability. The black lines and labels represent velocity profiles and interpretation of the C, E, and F layers obtained from previous RF analysis at PGC by Cassidy and Ellis (1993).

6.3 NC89

NC89 is a NEPTUNE station located on the continental slope offshore Vancouver Island (figure 2.2). The one RF used for inversion beneath this station originated near Vanuatu at a BAZ of 240° and epicentral distance of 88° (figure 5.3b). An inversion window of 6 s (1 s before and 5 s after the direct arrival) was inverted which included all prominent arrivals generated from within the targeted depth.

The first step in the inversion procedure was to assume IID errors and apply ASSA (using unknown σ) to find a best fitting model (figure 6.20). Parameters inverted for were V_s, Z, V_p/V_s and ρ. Prior bounds enforced in the inversion were derived from previous seismic studies (Van Ark et al., 2007; Cudrack and Clowes, 1993; Hyndman, 1979). Each layer had the same prior bounds (0.5 km/s $\leq V_s \leq$ 5.0 km/s, 0.5 km $\leq Z \leq$ 5 km, 1.65 $\leq V_p/V_s \leq$ 2.5, 2.5 g/cm^3, $\leq \rho \leq$ 3.5 g/cm^3). Previous studies (Van Ark et al., 2007; Rohr et al., 1988; Drew, 1987) have shown that the crustal structure beneath both OBS stations is relatively flat lying. Horizontal layers will not have a significant effect on radial RFs (section 3.1). For that reason, strike and dip were not included in the inversion at these sites.

As a step towards a successful and meaningful Bayesian inversion, a thorough investigation of data errors was conducted. The initial goal was to obtain data error statistics by the methods described in section 4.6, as they were at OZB and PGC. The concerns that arose using this method were that there was only one usable teleseismic event available and the deconvolution of this event produced an essentially noiseless RF. This enabled the inversion to find models that predicted the observed RF with unrealistically high accuracy (figure 6.20), such that the residuals were extremely small and the error statistics were likely not meaningful. Constructing a data covariance matrix ($\mathbf{C_d}$) from these residuals did not decorrelate the data as shown by the large side lobes of the autocorrelation function (figure 6.21). Using this $\mathbf{C_d}$

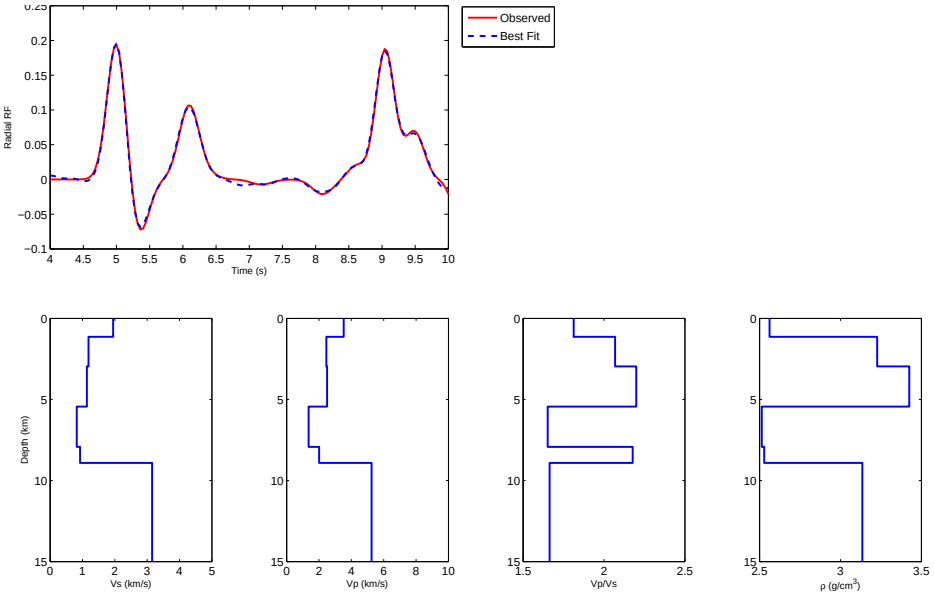

Figure 6.20: NC89 optimal model and corresponding radial RF from RF inversion with unknown IID data errors. The bottom row contains V_s, V_p, V_p/V_s and ρ profiles. The top row is the observed and predicted best fit RF.

for Bayesian inversion resulted in narrow marginal probability distributions (figure 6.22), which indicate unrealistically small parameter uncertainties.

The above results prompted an investigation for a more meaningful representation of the data errors for this station. As discussed in section 3.2.2, the time domain deconvolution attempts to construct a RF that reproduces the observed radial component waveform. For the data recorded at OBS stations, the predicted radial component fits the observed radial component with an accuracy of 80% (table 5.3), which indicates there is significant error in this process which is likely extends to the data errors. To utilize this information, the residuals between the observed and predicted radial components were calculated (figure 6.23) then deconvolved by the observed vertical component of that same event (to scale them to the same size as the RF). The standard deviation (σ=0.07) of these scaled residuals was used in likelihood calculations to evaluate models sampled by MHS.

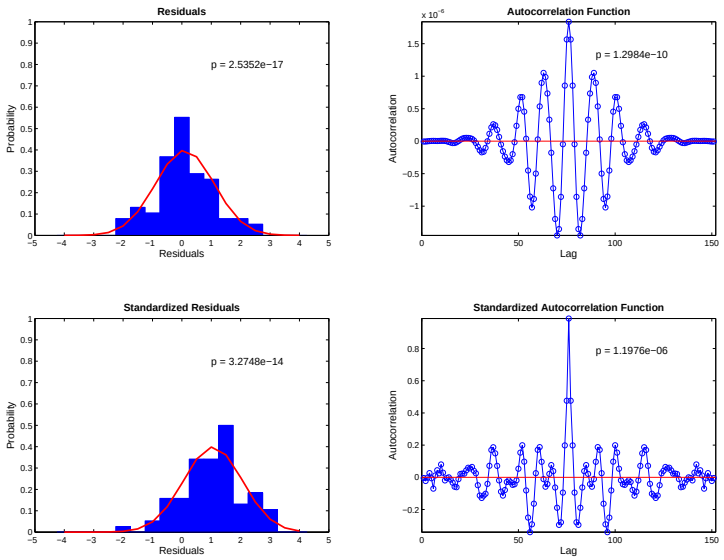

Figure 6.21: NC89 statistical tests to validate Gaussianity and randomness. The top panels represent raw residuals, while the bottom panels are the standardized residuals decorrelated by the $\mathbf{C_d}$ estimated from the single RF used at this station. The red line is a standard Gaussian distribution.

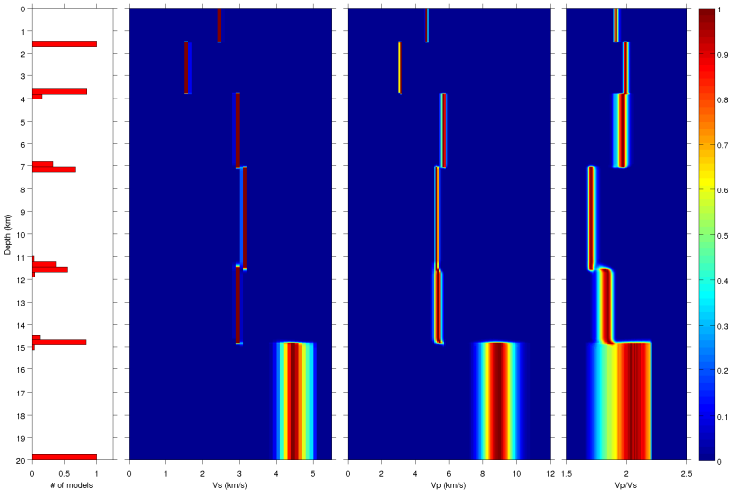

Figure 6.22: NC89 Bayesian inversion result for PGC using estimated $\mathbf{C_d}$ as described in section 4.6. Interface probability (left-most), and marginal probability profiles.

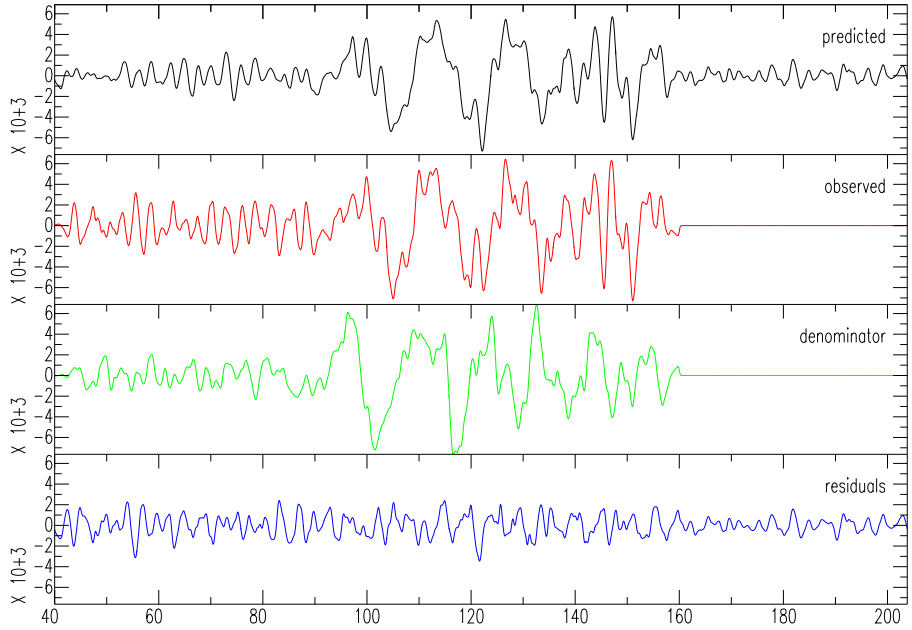

Figure 6.23: NC89 predicted and observed radial component, observed vertical component and radial component residuals of single event used for analysis. The horizontal scale is seconds from an arbitrary start time, while the vertical scale is counts.

It is recognized that this procedure to estimate error statistics is not ideal, as residuals are calculated from the raw data, but applied to the RF. The errors contributing to the RF undoubtedly have more sources than simply the processing errors and are likely correlated which is not captured by a single variance. Using a single σ assumes that the errors are IID, Gaussian distributed which could over-estimate the data error in some windows, while under-estimating it in others. Nonetheless, it is believed that this approach at least provides a representative error estimate which can be used in a meaningful Bayesian inversion.

Due to the data having a significantly better fit than the estimated data error, conducting a BIC study was also not successful. In such a case the BIC calculation is dominated by the structure penalization of the second term of equation 4.23. Multiple approaches to calculating the misfit and BIC were attempted, but the problem persisted.

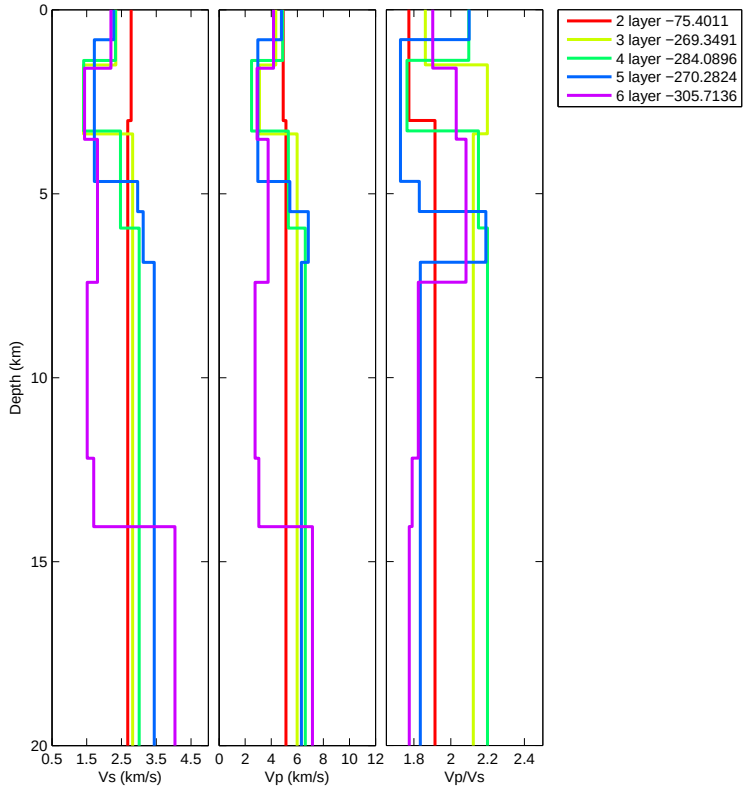

Figure 6.24: NC89 parametrization selection. Profiles represent optimal models for a varying number of layers. Legend entries are the number of layers and the accompanying model misfit.

Since the BIC was not useful in determining the number of parameters, models defined by an increasing number of layers (four parameters/layer) were investigated (figure 6.24) to qualitatively chose the number of layers. Using *a prior* information regarding the area, as well as experimental knowledge of RFs, a model of six layers was determined to be appropriate at NC89 for this data.

A Bayesian inversion was carried out for a six layer model (figure 6.25). As expected, the crustal structure beneath NC89 is not well constrained. Figure 6.26 shows that the deeper beneath the seafloor, the less constrained parameters are. Normalizing the probability distribution at each depth individually (figure 6.25), more clearly shows probable structure at all depths.

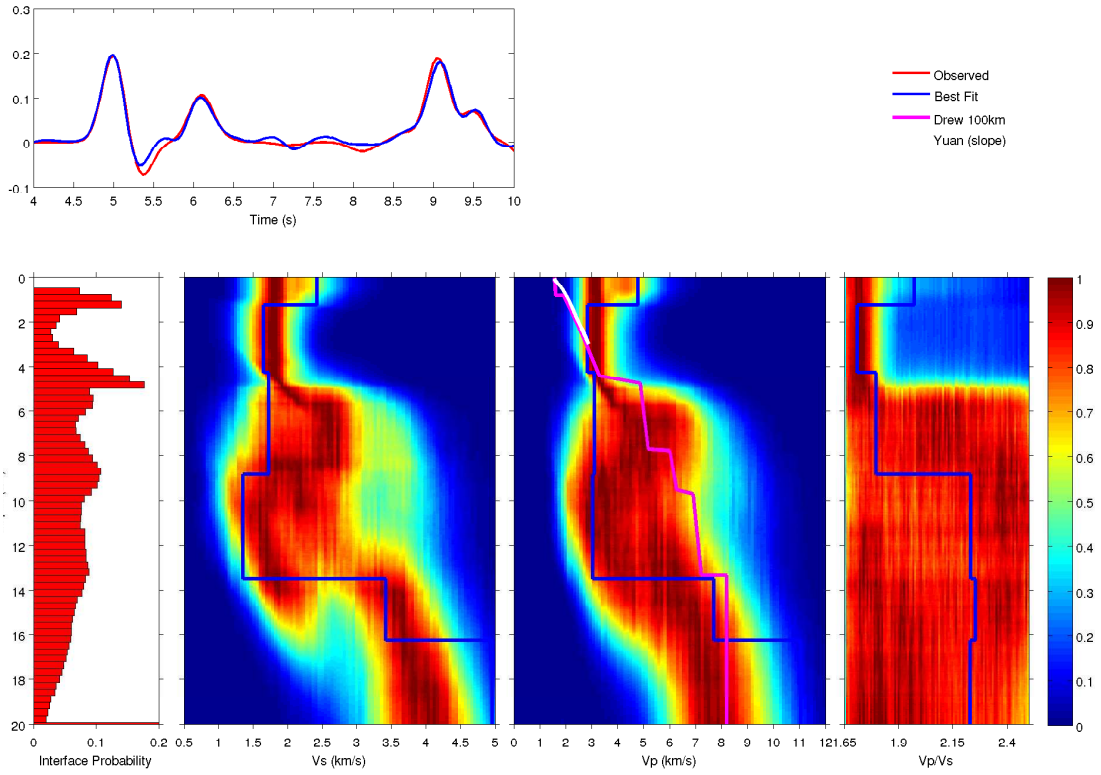

Figure 6.25: Bayesian inversion results for NC89. TOP: Comparison of observed RF and RF resulting from best fit model. BOTTOM: Interface probability (left-most), and marginal probability profiles of all parameters. Hot colours represent areas of high probability, cool colours represent low probability. Profiles labelled Drew and Yuan are V_p profiles from previous studies (Drew, 1987; Yuan et al., 1994).

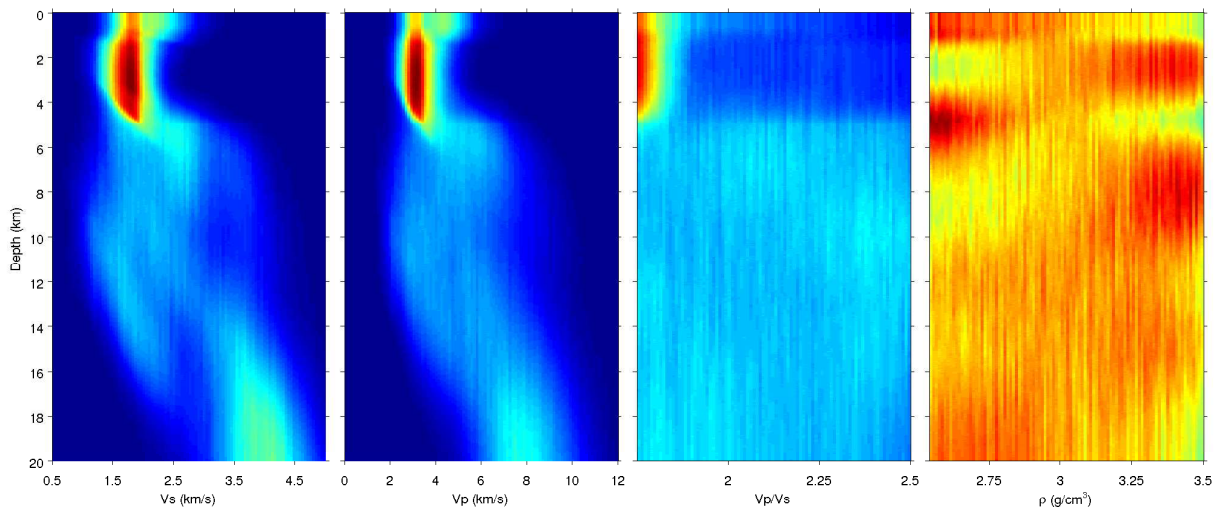

Figure 6.26: Bayesian inversion results for NC89. Marginal probability profiles of all parameters. Hot colours represent areas of high probability, cool colours represent low probability.

6.4 KEBB

KEBB is the western most station used in this study (figure 2.2). It was located just east of the JdFR during a temporary KECK funded deployment. The source of the event used (figure 5.3a) was near the south coast of Western Honshu, Japan, at a BAZ of 295° and epicentral distance of 69°. At KEBB, due to thin oceanic crust, a simple RF depicting a possible AMC was anticipated. The calculated RF (figure 6.27) shows the direct P wave at 5 s, followed by a small trough at ∼5.25 s, a peak at 5.5 s, a large trough at 6 s and peak at 6.5 s. These arrivals are a combination of direct conversions and multiples thereof. Following the last peak, the RF tapers and has no more significant arrivals, indicating that all the structure at this station is shallow. An inversion window of 4 s (1 s before and 3 s after the direct arrival) contains all the primary conversions from the seafloor to the Moho and free surface multiples.

Since this station was also an OBS station with only one usable event, similar problems were encountered estimating data errors as was the case at NC89. The same solution, using σ estimated from the deconvolution, was implemented. Figure 6.28 shows the residuals between the observed and estimated radial responses at KEBB which were used to calculate a σ of 0.08. Again, inversions using an increasing number of layers (2–6, figure 6.29) were investigated which lead to inverting for a four layer model at this station. The four layer model shows reasonable parameter profiles as well as the lowest misfit in the collection of models. The misfit for five and six layers increases, which indicates that the optimization algorithm had difficulty finding a good fit for the large number of (unconstrained) layers. The optimum model determined by ASSA (figure 6.27 upper panel) was used as the starting point for the Bayesian inversion. Parameter bounds for this station were the same as those used for NC89. Marginal PPDs normalized at each depth and normalized over all depths

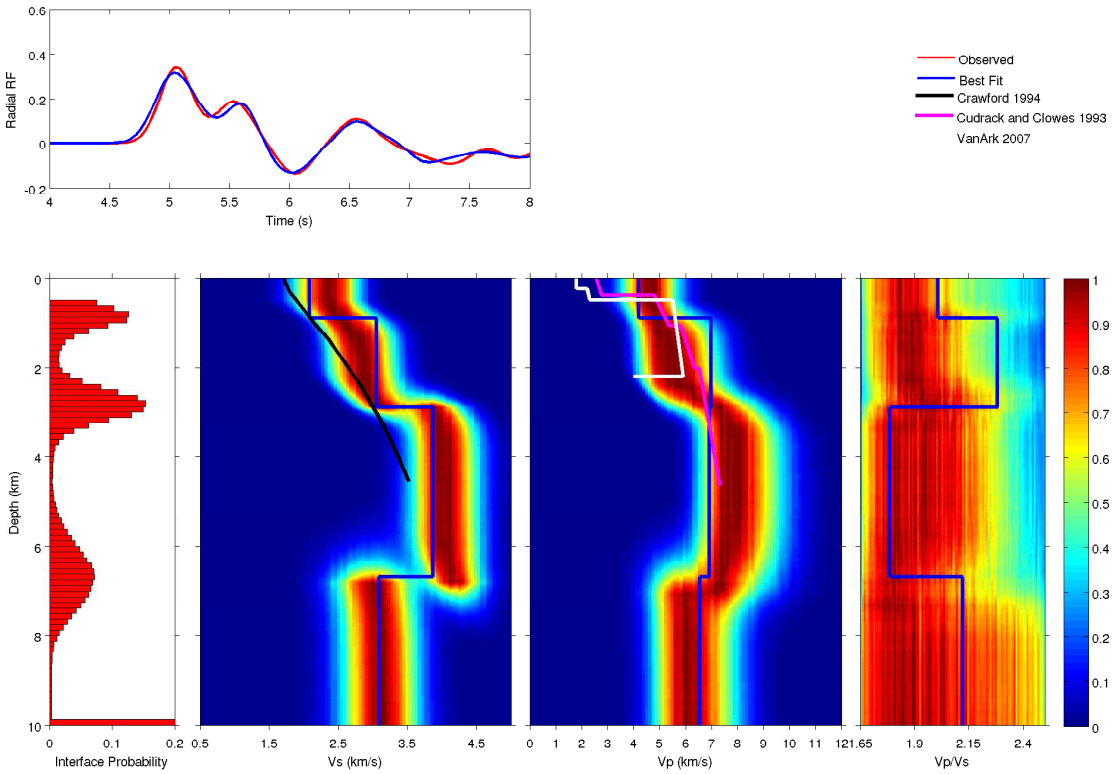

Figure 6.27: Bayesian inversion results for KEBB. TOP: Comparison of observed RF and RF resulting from best fit model. BOTTOM: Interface probability (left-most), and marginal probability profiles of all parameters (normalized at each depth). Hot colours represent areas of high probability, cool colours represent low probability. Profiles labelled Crawford and Cudrack and Clowes and VanArk are velocity profiles from previous studies (Crawford, 1994; Cudrack and Clowes, 1993; Van Ark et al., 2007).

are shown in the bottom panel of figure 6.27 and 6.30, respectively.

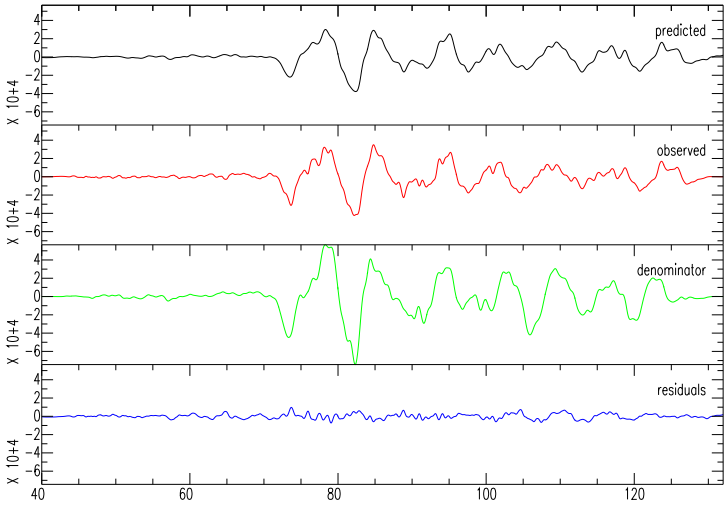

Figure 6.28: KEBB predicted and observed radial component, observed vertical component and radial component residuals of single event used for analysis. The horizontal scale is seconds from an arbitrary start time, while the vertical scale is counts.

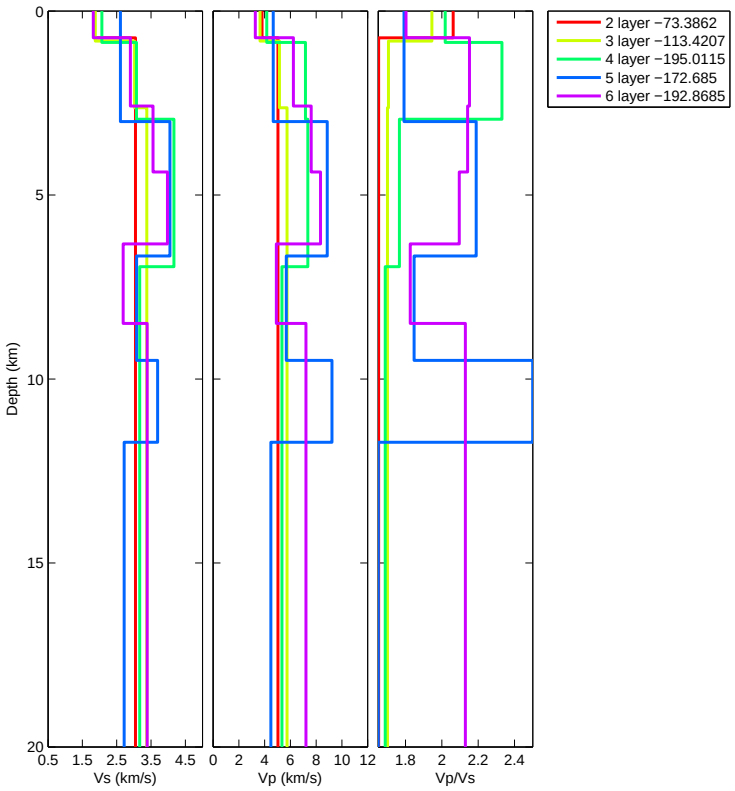

Figure 6.29: KEBB parametrization selection. Profiles represent optimal models for a varying number of layers. Legend entries are the number of layers and the accompanying model misfit.

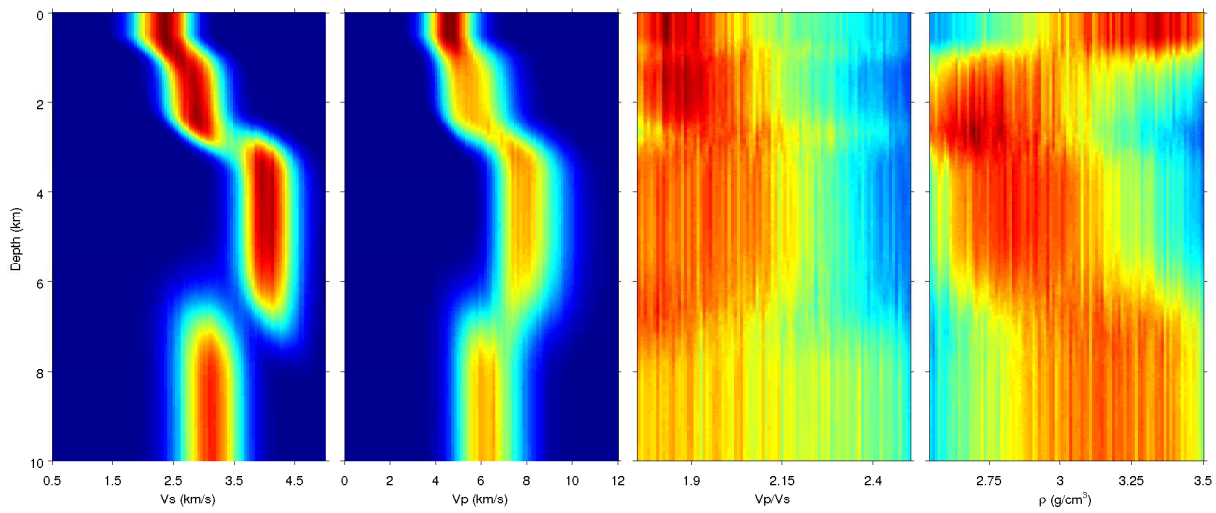

Figure 6.30: Bayesian inversion results for KEBB. Marginal probability profiles of all parameters. Hot colours represent areas of high probability, cool colours represent low probability.

Chapter 7

Interpretations

7.1 OZB

Results from OZB (west coast of Vancouver Island) show an eight layer model with well constrained parameters (figure 6.7). The uncertainties for the most influential parameter V_s, are $\sim$ 0.25 km/s. Other parameters show a range of uncertainties best described by the one dimensional marginal distributions (figure 6.7).

The V_s marginal profile (figure 6.10) generally agrees with the V_s profile of Nicholson et al. (2005) determined using RF inversion of Polaris data across southern Vancouver Island, as well as the interpretation of LITHOPROBE line 84-01 (Hyndman et al., 1990). Where these previous results resolved a 4–5 km thick E layer at about 22 km depth (figures 2.6 and 2.7), the result obtained here predicts a 6–8 km thick E layer at $\sim$19 km depth. The shallower depth and increased thickness predicted in this thesis are compensated for by a slightly higher average V_s ($\sim$3.2 km/s) of the E layer compared to 2.99 km/s predicted by Nicholson et al. (2005). The increased V_p/V_s of the E layer in these results is reasonable if it is assumed that this layer is one of decreased velocity due to pore fluids of the oceanic crust, as described by Bostock

et al. (2002). A dip of ∼18° related to the lower half of the E layer (and below) is estimated here. Values similar to this have been obtained for layer E and the oceanic mantle by past studies (Hyndman et al., 1990; Nicholson et al., 2005; Cassidy and Ellis, 1993). The shallower portion of the E layer determined by this inversion shows a dip of ∼8°. If in fact there is a difference in the dip, that would suggest that these two portions of the E layer are behaving slightly differently. Better azimuthal coverage as well as including muliples in the inversion would define this more clearly. The present inversion also suggests an oceanic Moho beneath OZB at a depth of ∼26 km which is accompanied by an increase in V_s to 4.5 km/s and decrease of V_p/V_s to 1.68, as expected for an interface representing the Moho.

The differences of the present model compared to the result of Nicholson et al. (2005) is the shallow layer with high V_s and absence of layers C and F (see figure 6.10). Layers C and F are thin, low velocity layers estimated at 7 km and 30 km, respectively, beneath the west coast of Vancouver Island, originally defined by active seismic studies (Spence et al., 1985; Hyndman, 1995; Hyndman et al., 1990), which have better resolving capabilities than RFs. One of the goals of this thesis was to determine how well the RF data alone resolved crustal structure, therefore minimal prior information was built into the inversion. A result of this is that thin layers with small velocity contrasts, that do not clearly stand out in the RF itself, are not resolved. The RFs used in this inversion at OZB do not show any definitive effects of the C and F layers as they do for the E layer as seen at 7 s in all RFs (figure 7.1). This results in marginal probability profiles without layers C and F.

The high V_s predicted at about 1 km depth (figure 7.1), however, is not expected and is not realistic. Without this high velocity, as shown in the RF represented by 'adjusted' in figure 7.1, the arrivals of the predicted RF arrive slightly later (<0.25 s), and the peak representing the direct arrival and shallow layers decreases in amplitude.

Although this high velocity is not reasonable, it is apparent that the inversion included it in an attempt to fit the high amplitude of the direct arrival. Decreasing the V_s and increasing the thickness of the shallow high velocity layer, or decreasing the V_s of neighbouring layers, as suggested by parameter correlations (figure 6.8) may provide a reasonable fit to the observed RF. However, this is not the structure the data resolves.

In this inversion, ρ is largely unconstrained. The alternating layers of large and small density in the marginal probability profile representing ρ indicates this. The strike and dip of the second, third and fourth layers appear to be constrained by the prior bounds, indicating that perhaps there is more strongly dipping structure in those layers than what was allowed in this inversion.

According to the result obtained in this thesis, the majority of earthquakes (from NRCAN 2012) within 10 km of OZB occur just above and below the E layer (figure 6.10). If the E layer is interpreted as the oceanic crust, this suggests that the earthquakes occur mainly in the continental crust and oceanic mantle. If the E layer is interpreted as a shear zone or duplex structure, this suggests that the earthquakes are predominantly in the continental crust.

7.2 PGC

Bayesian inversion of RFs collected at PGC (located in Sidney, BC) show comparable results to previous RF analysis by Cassidy and Ellis (1993) and interpreted from LITHOPROBE line 84-02 (Hyndman et al., 1990, figure 6.18), with similar uncertainties as were seen in the inversion of OZB data. V_s and V_p profiles resolved here are similar (within parameter uncertainties) to those found by Cassidy and Ellis (1993). Both results show a large negative velocity contrast at $\sim$40 km depth, which is the predicted depth of the E layer beneath central Vancouver Island (Hyndman et al.,

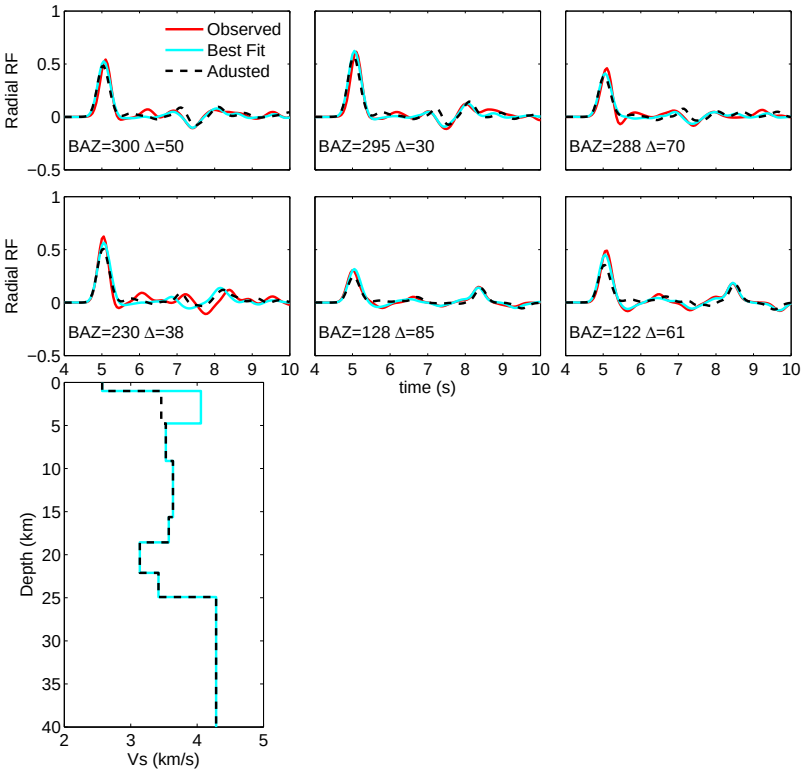

Figure 7.1: OZB optimal model and an adjusted model resembling a more likely V_s in the uppermost 5 km.

1990; Cassidy and Ellis, 1993; Bostock et al., 2002, figure 2.6). As well, the oceanic Moho of both inversions is determined to be at ∼52 km depth. The strike of these two interfaces is predicted to be between −20° and 0° with a dip of ∼18°, similar to that predicted at OZB. Similar to the inversion results for OZB, and for the same reason, the present inversion does not predict layers C and F; however, it does predict a 12 km thick low velocity layer (∼3.5 km/s) at a similar depth to that estimated by Cassidy and Ellis (1993), which is the approximate combined thickness from the top of layer E to the bottom of layer F predicted by Cassidy and Ellis (1993).

At PGC high V_s in the shallow layer, as well as a slightly high V_s in the half space, was estimated. Comparing the V_s of the best fit model here (figure 7.2) to that obtained by Cassidy and Ellis (1993) shows that this velocity is ∼0.5 km/s higher

than determined from seismic refraction (Yuan et al., 1994). Decreasing V_s by this amount decreases the amplitude of the direct P wave arrival and shifts arrivals a small amount (<0.25 s, figure 7.2). Although this shallow layer at both CNSN stations has higher than expected velocities, the properties of all other layers are reasonable. The cause of the high shallow velocities is probably due to a systematic error in the data processing (For example, using different deconvolution techniques when calculating RFs than what was used in the inversion) or model assumptions. The increased velocity of the half space could be due to the inversion window chosen. The layer velocity is better constrained when free surface multiples from that layer are included in the inversion. Unfortunately, including these also includes internal multiples from shallower layers which are not calculated in the forward model. To alleviate issues related to internal multiples a window which eliminated both desired free surface multiples and undesired internal multiples was used.

7.3 NC89

Crustal structure beneath NC89, the NEPTUNE OBS station located on the continental slope of Vancouver Island (figure 2.2), was inverted for using a six layer model (figure 6.25). The final result of the Bayesian inversion reveals only two well-defined interfaces (at 5 km and 13 km depth) and substantial parameter uncertainties. The first and second layers appear to be similar with V_s ~1.9 km/s, V_p ~3.0 km/s, V_p/V_s ~1.7 (figure 2.2). In total, the thickness of these two layers is ~5 km which is similar to the sediment thickness seen on nearby seismic lines 89-07 and 89-08 (Yuan et al., 1994). These sediment layers that the RF resolved are interpreted as a sediment package consisting of oceanic sediments as well as accretionary wedge material as seen at the ODP889 drill site (Scherwath et al., 2006). The low V_p/V_s ratio of

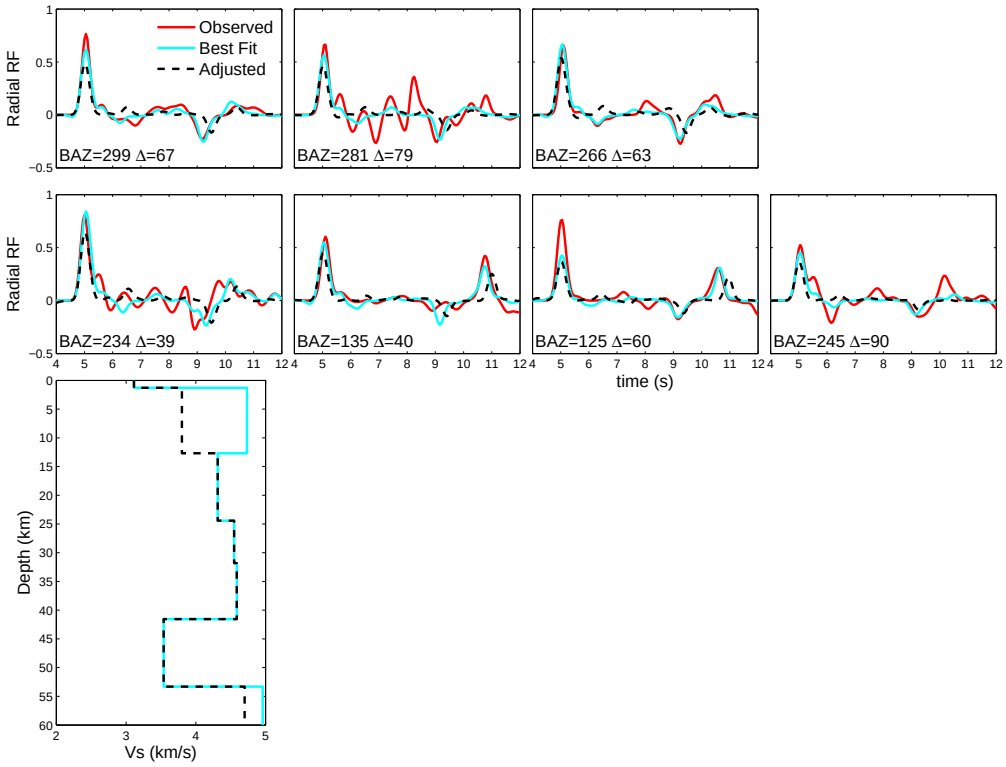

Figure 7.2: PGC best fit model and an adjusted model resembling a more likely V_s at shallow and deep depths.

the sediments is most likely due to the consolidation of incoming oceanic sediments and therefore loss of pore space fluid and increase in V_s as described by Yuan et al. (1994). The velocities and thicknesses of the third and fourth layers, representing oceanic layers 2 and 3, are not well defined. Most likely they represent two layers with constant properties, or two layers with a large negative velocity contrast between them totalling ∼10 km in thickness. The interface of the fifth layer at ∼13 km depth represents the oceanic Moho where V_s increases as it transitions from crust to mantle. The sixth layer, or half space, is a continuation of the upper mantle. The interface probability of the sixth layer is relatively low, compared to the other interfaces. This is a sign that the problem could be over-parametrized with six layers.

Both the sediment and mantle properties are comparable to that predicted by

Drew (1987). Although the RF does not resolve a shallow low velocity layer, the V_p found in previous studies (Drew, 1987; Yuan et al., 1994) is within the uncertainty bounds of the model inversion estimated here, as seen in figure 6.25.

The abrupt change to unconstrained parameters beneath the sediments is a consequence of a small poor quality dataset, the low frequency RF, and lack of identifiable multiples from within the oceanic crust. Forward modelling has been carried out to help identify the interfaces at which arrivals in the observed RF were generated. This modelling revealed that the direct P_ms arrival is seen at 6.25 s and its multiple may be represented (along with other arrivals) by the arrival at 9 s (figure 6.25). Any arrivals from structure within the crust are contained within these large amplitude arrivals, making it challenging to resolve them. For example, the P_s conversion from the lower sediment interface is contained within the direct P wave arrival, which causes the slight offset of this peak.

The structure between the sediments and the Moho is highly unconstrained. The best fit model has unreasonable V_s above the Moho. RFs were generated from models chosen arbitrarily from within the bounds of the PPD (figure 7.3). The amplitude of the P_ms arrival and timing of the observed multiple at 9 s cannot be replicated by any of the reasonable models tested. As well, extreme negative V_s contrasts are be required to match the large amplitude trough at 5.5 s seen in the observed RF. Such a model is not within uncertainty bounds, nor is it physically plausible. This leads one to believe that arrivals from unmodelled sources are interfering with the RF, or the RF itself is not correct. Sources of waves that we have not modelled include internal multiples, water reverberations (P_wp), and reflections off of internal and adjacent structure. Direct P_wp phases would arrive $\sim$4 s after the direct P wave, which is not seen in the raw data (figure 5.3b). Since P_wp is a compressional wave, it is not expected to have a significant effect on a RF, as RFs represent shear wave arrivals. However, P_wpp_ms

and $P_w ps_m s$ converted arrivals, which are not generated in the forward model, could exist. These arrivals would arrive outside the inversion window, therefore they are not a concern in this inversion. Including the assumed $P_m s$ arrival at 6 s in the inversion window means the RF samples structure within a radius of ∼2 km around the station (section 3). Within 2 km of NC89 not only is there structure on the seafloor but there is a significant amount of internal deformation (Yuan et al., 1994) which could cause unpredictable shear wave conversions. If many RFs were available at this site a comparison between RFs could highlight such spurious, unmodelled arrivals.

In an ideal situation many teleseismic events from deep sources at distances of

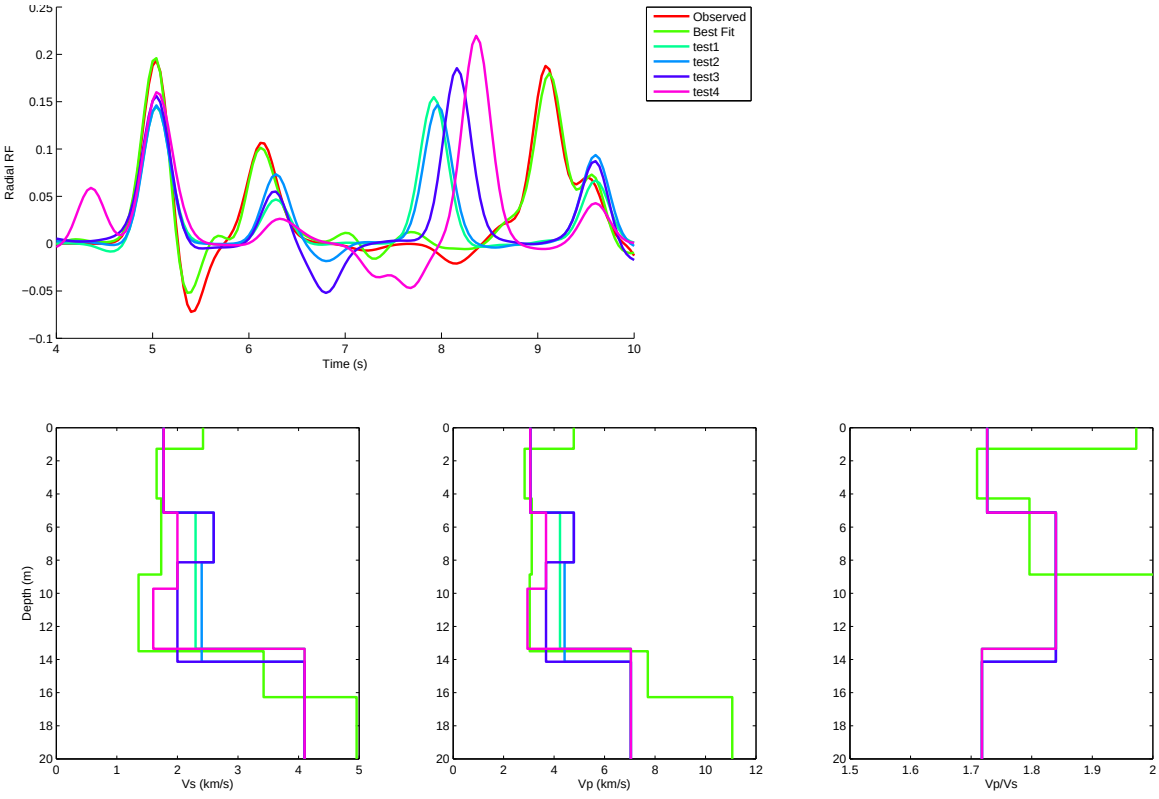

Figure 7.3: NC89 forward modelling. RFs from subjectively constructed reasonable models from within the bounds of PPD were modelled to attempt to fit the observed RF.

30° would be used for RF analysis. However, only a single RF is available at this station from ∼90° away and it has a significant amount of noise, making this RF less than ideal representation of the crustal structure at NC89. Although the parameter uncertainties estimated are large, interface probabilities (and therefore sediment and crustal thickness) were predicted at depths which agree with previous studies (Waldron, 1982; Spence et al., 1985; Drew, 1987).

7.4 KEBB

KEBB, the temporary OBS station located east of the JdFR, produced results which clearly defined three interfaces (figure 6.27). This RF was the simplest RF inverted in this thesis. A time window of only 4 s was used in the inversion to capture the shallow structure at the ridge. The interfaces resolved defined a thin layer of oceanic sediments and layer 2A extrusive basalts to a depth of approximately 1 km with V_s ∼1.9 km/s, a 1–1.5 km thick layer 2B containing sheeted dikes with V_s ∼2.8 km/s, and a 2.5–3.5 km thick layer 3 composed of V_s ∼3.8 km/s gabbro.

A combination of data quality, location and resolving ability of RFs resulted in the AMC (axial magma chamber) resolved by Van Ark et al. (2007) and Wilcock et al. (2002) not being resolved by the single RF inverted at this site. When a shorter data length (3 s) was inverted the optimal model appeared to resolve a low velocity zone at 2 km depth which may represent an AMC (figure 7.4). Using this model as a starting point for the Bayesian inversion resulted in a V_s marginal probability profile that did not resolve the AMC. This suggests that although an AMC may be present, and a model with an AMC does fit the observed data, the data can not resolve it due to the low frequency content of the data and the inability to meaningfully estimate data errors from a single RF (errors are likely over-estimated

by the deconvolution procedure). The ability to resolve the AMC is reliant upon its thickness. The thickness of the AMC underlying the Endeavour segment has not been accurately determined, but it is expected to be thin (∼1 km), which makes resolving it with RF inversion difficult.

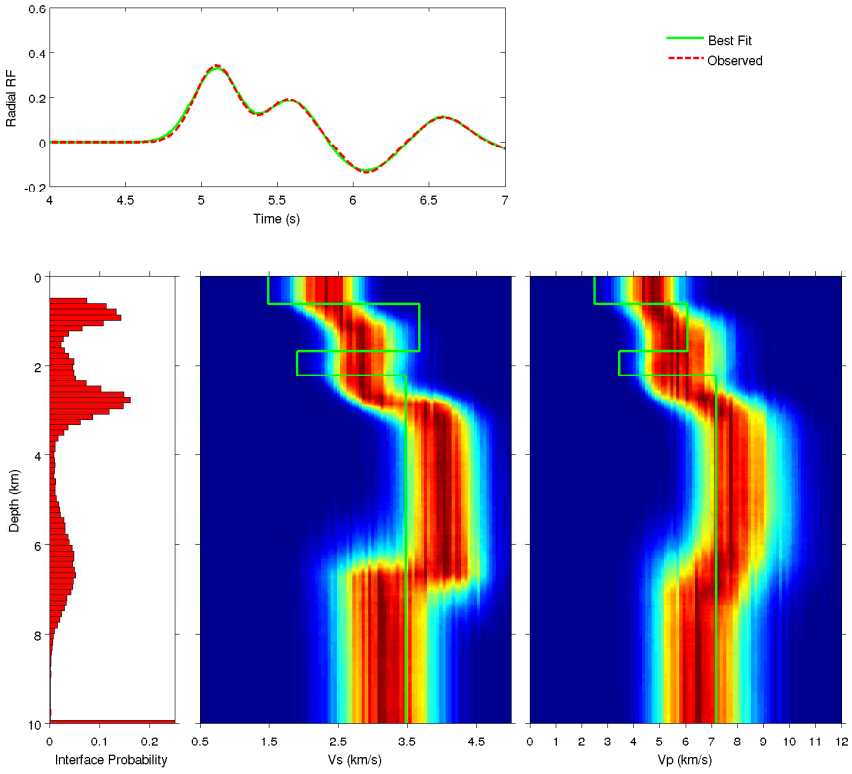

Figure 7.4: Bayesian inversion result for KEBB started at model showing possible AMC. TOP: Comparison of observed RF and RF resulting from starting model. BOTTOM: Interface probability (left-most), and marginal probability profiles of V_s and V_p and starting model (normalized at each depth). Hot colours represent areas of high probability, cool colours represent low probability.

The marginal probability profiles estimated at KEBB are comparable to V_p profiles from reflection (Van Ark et al., 2007), refraction (Cudrack and Clowes, 1993) and compliance (Crawford, 1994) studies (figure 6.27). Similar to NC89, velocities in the most shallow layer are much higher than what previous studies determined. This difference could be due to the lower resolution of the RF than reflection or refraction

data. Constraining the V_s parameter upper bound to a lower velocity does not change the inversion result for structure deeper than the first layer. The model adjustment is compensated in the inversion by accepting a higher misfit. The high velocities seen in this result are likely due to the same reason they are seen at OZB and PGC.

The significant arrivals seen in the RF are generated by the large velocity contrast around 3 km depth which is coincident to the bottom of the predicted AMC (Van Ark et al., 2007) and earthquake depths observed by Wilcock et al. (2002). The P_s arrival from this interface is seen around 5.5 s and its multiple at ∼6.5 s. The negative velocity contrast at 6 km controls the arrival time and amplitude of the trough at 6 s and the fit to the RF after 7 s. The depth of this contrast is similar to the predicted Moho depth on the Pacific plate at the Endeavour segment of the JdFR (Rohr et al., 1988); however, a positive velocity contrast is expected at the Moho. This decrease in velocity is likely not a representation of the structure at that depth. If multiples were included in the inversion this layer would be better constrained and more meaningful. V_p/V_s and ρ are largely unconstrained by the data at this station.

Chapter 8

Conclusions

This thesis explores receiver function analysis using a Bayesian inversion approach to address outstanding questions regarding the structure of the oceanic Juan de Fuca plate offshore Vancouver Island. This is the first detailed passive seismic study using new OBS and CNSN data in this region. The dataset used for inversion was comprised of RFs from two reliable onshore stations (OZB and PGC) and two offshore stations, which in all span from the Endeavour segment of the Juan de Fuca Ridge to the west coast of Vancouver Island.

8.1 Bayesian RF Inversion

The Bayesian inversion utilized in this thesis is a sophisticated method in which model uncertainties are derived from data error statistics. This is accomplished by sampling parameters proportional to their probability using an efficient implementation of MHS. Important steps leading to a meaningful Bayesian inversion include data error estimations and determining an appropriate model parametrization. At stations where multiple RFs were calculated (OZB and PGC) data uncertainties were estimated from data residuals. At these stations a thorough BIC study was carried

out to determine the model parametrization consistent with the resolving power of the data. For stations where only one RF was available, data uncertainties were estimated using the misfit introduced in the time domain deconvolution process and model parametrizations were determined by considering previous studies and experimental knowledge.

The results of the Bayesian inversion carried out at each station are interpreted in terms of marginal probability profiles for V_s, V_p, ρ, and in some cases strike and dip.

8.2 Data Availability

With seismometers located offshore Vancouver Island, there is a possibility of increasing knowledge regarding the JdF plate and the subduction process in northern Cascadia. Data were provided for use in RF analysis from five offshore locations. Factors including the short duration recording period for OBS data, and high levels of oceanic noise, resulted in only one useful teleseismic event recorded on each of two OBSs (KEBB and NC89). The deconvolution of each single event produced a RF which did not preserve realistic data errors. For these reasons, intended methods of data error estimation were not possible, and therefore the Bayesian inversion results were not as informative as desired. To take full advantage of RF inversion a larger dataset, covering a wide range of BAZ, is required.

Data recorded at OZB and PGC were more numerous and of higher quality. RF inversion has been previously carried out using an older dataset from PGC. For this reason, using data from this station provides a good comparison of the inversion implemented here. OZB is a more recent CNSN station and has not been used for RF analysis. The location of OZB with respect to the subducting JdF plate, NC89

and PGC, make results from this station informative of the subduction process and seismic hazard the CSZ poses.

8.3 The JdF Plate

Bayesian RF inversion was carried out at four sites, KEBB, NC89, OZB, and PGC. A goal of this thesis was to provide additional information to answer outstanding questions regarding the depth and thickness, strike and dip angles of the seismic E layer, and the oceanic Moho of the Juan de Fuca plate. Observing the best fit models (figure 8.1) and marginal probability profiles interpreted from the Bayesian inversion results at each of the four stations gives insight into these questions.

Starting at KEBB at the JdFR, results show a layer ∼1 km thick containing a thin layer of oceanic sediments and oceanic layer 2A. Beneath this layer lies layer 2B and the 2B/3 interface at 2.5–3.5 km depth (figure 8.1). Previous active source studies have provided evidence of an AMC at this location (Rohr et al., 1988; Wilcock et al., 2002; Van Ark et al., 2007). The dataset used here could not resolve an AMC.

KEBB is located on the Pacific plate and is approximately 300 km east of NC89, therefore it is not meaningful to make correlations between the two stations. However, assuming that the sediment thickness is similar on both sides of the JdF ridge, the results indicate that sediment and oceanic crust thickness increases with distance away from the ridge.

As shown in figure 8.1, results at NC89 indicate a 4–5 km thick layer of sediments, beneath which is a 8–10 km thick oceanic crust with V_s of 2–3 km/s. The depth of the oceanic Moho at this station is resolved at ∼13 km. Approximately 150 km east of NC89 is OZB. Here, the low velocity E layer is resolved to be at ∼19 km depth with an average V_s of ∼3.2 km/s, and the oceanic Moho is at ∼25 km depth. East of

OZB, at PGC, the E layer is observed at 40 km depth (with a similar V_s as observed for the E layer at OZB), and the oceanic Moho at $\sim$ 53 km depth.

While NC89 is expected to have an insignificant dip angle, which was therefore constrained to zero in the inversion, the strike and dip associated with the E layer at OZB and PGC was determined by inversion to be most probable between N35°E and N10°W and 16°–20°, respectively. Marginal probability profiles of strike and dip for the two stations generally agree with each other (figures 6.10 and 6.18) as well as with previous studies (Hyndman et al., 1990; Cassidy, 1992; Nicholson et al., 2005). Using the depth of the E layer from the best fit model (figure 8.1) at OZB and PGC, the dip of the JdF plate is approximated to be 19°, which is within uncertainty bounds at each station.

The thickness of the crust at NC89, as well as the thickness of the E layer at OZB and PGC, are between 7–10 km. The similarity of thickness, V_s, and depth (taking into account dip) at all three stations, as well as strike and dip at OZB and PGC, is supporting evidence that a model where the E layer represents the oceanic crust is probable, similar to the results of Bostock et al. (2002) and Nicholson et al. (2005).

At NC89 there is 4–5 km of sediments overlying the oceanic crust. If these sediments were subducted with the oceanic crust, layer E at OZB and PGC would be 4–5 km thicker than what the inversion predicted at these stations, therefore it is likely that most of the sediments observed at NC89 are scraped off the JdF plate as subduction proceeds.

As well as sediments being removed during subduction, pore space fluid is also reduced. The E layer at OZB is defined by two distinct layers with slightly different velocities ($\sim$ 3.0 km/s and 3.2 km/s) but similar to V_s seen at NC89, located east of OZB, and at PGC, located west of OZB. The two-part E layer at OZB may represent a transition area where different mineralogical properties exist within the oceanic

crust due to compression of pore space and de-watering of the of the oceanic crust as it subducts.

The depth of the oceanic Moho, indicated by the large contrast of V_s at depths of 14 km, 25 km, and 53 km, at NC89, OZB, and PGC, respectively, as shown in figure 8.1, is coincident with the Moho depth proposed by Cassidy and Ellis (1993), Bostock et al. (2002), Nicholson et al. (2005), Yuan et al. (1994), and Drew (1987). It can be concluded that this interface represents the oceanic Moho of the JdF plate at all three of these stations.

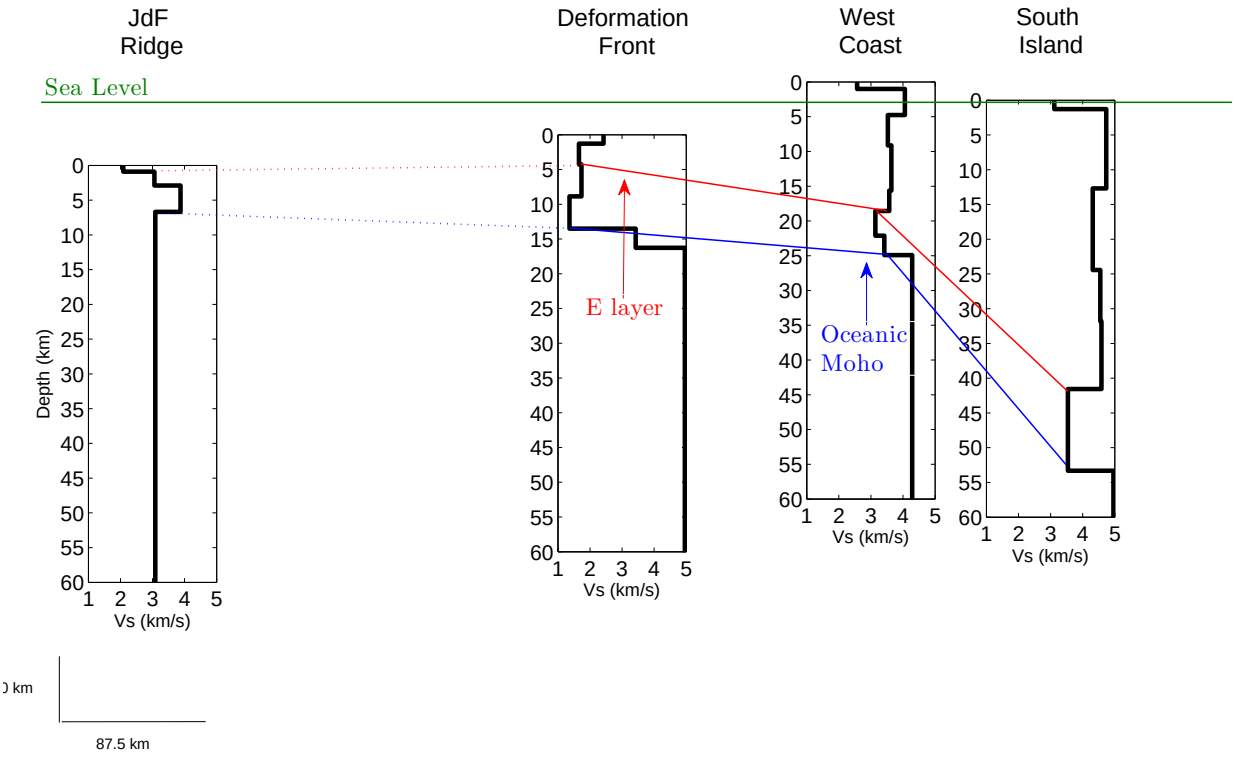

Figure 8.1: Cross section of best fit models from each station. Scale refers to the location of the to left hand corner of each plot, not the depths annotated.

8.4 Suggestions for Future Studies

The underlying cause of any shortcomings encountered using the new OBS data stemmed from a shortage of data. Normally, over two years sufficient data are recorded for an adequate RF study. However, due to the high noise levels recorded on the OBSs, there were few useful events available. As mentioned previously, NEPTUNE has three OBS deployed at this time. Given a longer time period, it is likely more useful events will be recorded which would allow for a more detailed RF study at these stations.

Future studies should examine the most appropriate forward modelling routine to use in an oceanic environment. The forward model used in this thesis was designed to model only direct conversions and free surface multiples. RF generated from OBS data may have multiples that the forward model used does not consider. Perhaps the Thompson-Haskell forward model (Haskell, 1953), which models the complete waveform response, would be more suitable in this environment. Assumptions of an isotropic, flat, crustal structure at the OBS stations may be an over-simplification of the structure which complicates inversions. Using a forward model that could take into account these properties may also improve inversion results.

Bibliography

Ammon, C. (1991). The isolation of receiver effects from teleseismic P waveforms. *Bulletin of the Seismological Society of America*, 81:2504–2510.

Ammon, C., Randall, G., and Zandt, G. (1990). On the non-uniqueness of receiver function inversions. *Geophysical Journal International*, 95(B10):15303–15318.

Barclay, A. H. and Wilcock, W. S. (2004). Upper crustal seismic velocity structure and microearthquake depths at the Endeavour segment, Juan de Fuca Ridge. *American Geophysical Union*, 5(1).

Blackman, D. K., Orcutt, J. A., and Forsyth, D. W. (1995). Recording teleseismic earthquakes using ocean-bottom seismographs at mid-ocean Ridges. *Bulletin of the Seismological Society of America*, 85(6):1648–1664.

Bodin, T. (2010). *Transdimensional approaches to geophysical inverse problems*. PhD thesis, Australian National University, Canberra, ACT, Australia.

Bostock, M., Hyndman, R., Rondenay, S., and Peacock, S. (2002). An inverted continental moho and serpentinization of the forearc mantle. *Nature*, 417:536–538.

Calvert, A., Hasselgren, E., and Clowes, R. (1990). Oceanic rift propagation—a cause of crustal underplating, and seamount volcanism. *Geology*, 18(9):886–889.

Calvert, A., Preston, L., and Farahbod, A. (2011). Sedimentary underplating at the Cascadia mantle-wedge corner revealed by seismic imaging. *Nature*, 4:545–548.

Calvert, A. J. (2004). Seismic reflection imaging of the two mega-thrust shear zones in the northern Cascadia subduction zone. *Nature*, 428:163–167.

Canales, J. P., Detrick, R. S., Carbotte, S. M., Kent, G. M., Diebold, J. B., Harding, A., Babcock, J., Nedimovic, M., and VanArk, E. (2005). Upper crustal structure and axial topography at intermediate spreading ridges: Seismic constraints from the southern Juan de Fuca Ridge. *Journal of Geophysical Research*, 110:B12104, 27 PP.

Canales, J. P., Nedimovic, M. R., Kent, G. M., Carbotte, S. M., and Detrick, R. S. (2009). Seismic reflection images of a near-axis melt sill within the lower crust at the Juan de Fuca ridge. *Nature*, 460:89–93.

Cassidy, J. (1992). Numerical experiments in broadband receiver function analysis. *Bulletin of the Seismological Society of America*, 82(32):1453–1474.

Cassidy, J. and Ellis, R. M. (1993). S wave velocity structure of the northern Cascadia Subduction Zone. *Journal of Geophysical Research*, 98(B3):4407–4421.

Clowes, R. and Au, D. (1993). In-situ evidence for a low degree of S-wave anisotropy in the oceanic upper mantle. *Geophysical Research Letters*, 9(1):13–16.

Clowes, R., Baird, D., and Dehler, S. (1997). Crustal structure of the Cascadia subduction zone, southwestern British Columbia, from potential field and seismic studies. *Canadian Journal of Earth Sciences*, 34:317–335.

Crawford, W. C. (1994). *Determination of Oceanic Crustal Shear Velocity Structure from Seafloor Compliance Measurements*. PhD thesis, University of California, San Diego, San Diego, California, USA.

Cudrack, C. F. and Clowes, R. M. (1993). Crustal structure of Endeavour Ridge segment, Juan de Fuca Ridge, from a detailed seismic refraction survey. *Journal of Geophysical Research*, 98(B4):6329–6349.

DeGroot, M. (1975). *Probability and Statistics*. Addison-Wesley, Reading.

Dolenc, D., Romanowicz, B., McGill, P., and Wilcock, W. (2008). Observations of infragravity waves at the ocean-bottom broadband seismic stations Endeavour (KEBB) and Explorer (KXBB). *AGU*, 9(5).

Dosso, S. (2002). Quantifying uncertainty in geoacoustic inversion I: a fast Gibbs sampler approach. *Journal of Acoustics Society America*, 111:143–159.

Dosso, S. and Dettmer, J. (2011). Bayesian matched-field geoacoustic inversion. *Inverse Problems*, 27(5):doi:10.1088/0266–5611/27/5/055009.

Dosso, S., Nielsen, P., and Wilmut, M. (2006). Data error covariance in matched-field geoacoustic inversion. *Journal of Acoustical Society of America*, 119:208–219.

Dosso, S., Wilmut, M., and Lapinski, A. (2001). An adaptive hybrid algorithm for geoacoustic inversion. *IEEE Journal of Oceanic Engineering*, 26:324–336.

Drew, J. (1987). A re-evaluation of the seismic structure across the active subduction zone of Western Canada. Master's thesis, University of British Columbia,, Vancouver British Columbia, Canada.

Gilks, W., Richardson, S., and Spiegelhalter, G. (1996). *Markov Chain Monte Carlo in Practice*. Chapman and Hall, London.

Haskell, N. A. (1953). The dispersion of surface waves on multi-layered media. *Bulletin of the Seismological Society of America*, 43(1):17–34.

Hasselgren, E. and Clowes, R. (1995). Crustal structure of northern Juan de Fuca plate from multichannel reflection data. *Canadian Journal of Earth Sciences*, 100(B4):6469–6486.

Hasselgren, E., Clowes, R., and Calvert, A. (1992). Propagating rift pseudofaults—zones of crustal underplating imaged by multichannel seismic reflection data. *Geophysical Research Letters*, 19(5):485–488.

Hyndman, R. (1979). Poisson's ratio in the oceanic crust—a review. *Techtonophysics*, 59:321–333.

Hyndman, R. (1995). The Lithoprobe corridor across the Vancouver Island continental margin: the structural and tectonic consequences of subduction. *Canadian Journal of Earth Sciences*, 32:1777–1802.

Hyndman, R. and Rogers, G. (2010). Great earthquakes in Canada's west coast: a review. *Canadian Journal of Earth Sciences*, 47:801–820.

Hyndman, R., Yorath, C., Clowes, R., and Davis, E. (1990). The northern Cascadia Subduction Zone at Vancouver Island: seismic structure and tectonic history. *Canadian Journal of Earth Sciences*, 27:313–329.

Ingber, L. (1989). Very fast simulated reannealing. *Mathematical Computing and Modelling*, 12:967–993.

Kass, R. E. and Raftery, A. E. (1995). Bayes factors. *Journal of the American Statistical Association*, 90(430):773–795.

Kirkpatrick, S., Gelatt, C., and Vecchi, M. (1983). Optimization by simulated annealing. *Science*, 220:671–680.

Kurtz, R., DeLaurier, J., and Gupta, J. (1990). The electrical conductivity distribution beneath Vancouver Island: a region of active plate subduction. *Journal of Geophysical Research*, 95:10929–10946.

Langston, C. (1977). The effect of dipping structures on source and receiver responses for constant ray parameter. *Bulletin of the Seismological Society of America*, 67:1029–1050.

Langston, C. (1979). Structure under Mount Rainier, Washington, inferred from teleseismic body waves. *Journal of Geophysical Research*, 84:4749–4762.

Laske, G., Collins, J., Wolfe, C., Solomon, S., Detrick, R., Orcutt, J., Bercovici, D., and Hauri, E. (2009). Probing the Hawaiian hot spot with new broadband ocean bottom instruments. *EOS Transcripts, AGU*, 90(41):362–363.

McClymont, A. F. and Clowes, R. M. (2005). Anomalous lithospheric structure of the northern Juan de Fuca plate—a consequence of rift propagation? *Techtonophysics*, 406:213–231.

Montgomery, D. and Peck, E. (1992). *Introduction to Linear Regression Analysis*. John Wiley and Sons, New York.

Nedimovic, M., Hyndman, R., Ramachadran, K., and Spence, G. (2003). Reflection signature of seismic and aseismic slip on the northern Cascadia subduction interface. *Nature*, 42:416–420.

Nelder, J. and Mead, R. (1965). A simplex method for function minimization. *Computer Journal*, 7:308–313.

Nicholson, T., Bostock, M., and Cassidy, J. (2005). New constraints on subduction zone structure in northern Cascadia. *Geophysics Journal International*, 161:849–859.

NRCAN (2012). Earthquakes Canada, GSC, Earthquake Search (On-line Bulletin). http://earthquakescanada.nrcan.gc.ca/stndon/NEDB-BNDS/bull-eng.php.

Owens, T. (1984). *Determination of crustal and upper mantle structure from analysis of broadband teleseismic P-waveforms*. PhD thesis, University of Utah, Salt Lake City.

Piana Agostinetti, N. and Malinverno, A. (2009). Receiver function inversion by trans-dimensional Monte Carlo sampling. *Geophysical Journal International*, 181:858–872.

Press, F. and Seiver, R. (2001). *Understanding Earth*. WH Freeman and Company, New York, NY, USA, 2nd edition.

Press, W., Teukolsky, S., Vetterling, W., and Flannery, B. (1992). *Numerical Recipes*. Cambridge University Press, Cambridge.

Ramachandran, K., Hyndman, R., and Brocher, T. (2006). Regional P wave velocity structure of the northern Cascadia Subduction Zone. *Journal of Geophysical Research*, 111(B1230):B12301, 15 PP.

Riddihough, R. (1979). Gravity and structure of an active margin—British Columbia and washington. *Canadian Journal of Earth Sciences*, 16:350–363.

Riddihough, R. (1984). Recent movements of the Juan de Fuca plate system. *Journal of Geophysical Research*, 89(B8):6980–6994.

Riddihough, R. and Hyndman, R. (1991). *Geology of the Cordilleran Orogen in Canada*, volume 2, pages 435–455. Geological Survey of Canada.

Ristau, J. and Rogers, G. (2006). Noise studies of KECK broadband ocean bottom seismographs off the British Columbia coast. (personal communication).

Rohr, K., Milkereit, B., and Yorath, C. (1988). Asymmetric deep crustal structure across the Juan de Fuca Ridge. *Geology*, 16:533–537.

Sambridge, M. (1999a). Geophysical inversion with a neighbourhood algorithm—I. Searching a parameter space. *Geophysics Journal International*, 138(2):479–494.

Sambridge, M. (1999b). Geophysical inversion with a neighbourhood algorithm—II. Appraising the ensemble. *Geophysical Research Letters*, 138(3):727–746.

Sambridge, M. and Mosengaard, K. (2002). Monte Carlo methods in geophysical inverse problems. *Reviews of Geophysics*, 40(3(1)):3–29.

Scherwath, M., Riedel, M., Spence, G. D., and Hyndman, R. D. (2006). *Proceedings of the Integrated Ocean Drilling Program*, volume 311, page doi:10.2204/iodp.proc.311.110.2006. IODP Management International, Inc.

Schwartz, G. (1978). Estimating the dimensions of a model. *Institute of Mathematical Statistics*, 6(2):461–464.

Shibutani, T., Sambridge, M., and Kent, B. (1996). Genetic algorithm inversion for receiver functions with application to crust and uppermost mantle structure beneath Eastern Australia. *Geophysical Research Letters*, 23(14):1829–1832.

Spence, G., Clowes, R., and Ellis, R. (1985). Seismic structure across the active subduction zone of Western Canada. *Journal of Geophysical Research*, 90(B8):6754–6772.

Tarantola, A. (1987). *Inverse Problem Theory: Methods for Data Fitting and Model Parameter Estimation*. Elselvier, Amsterdam.

Tucholke, B. (1998). Discovery of 'megamullions' reveals gateways into the ocean crust and upper mantle. *Oceanus*, 14(1):15–19.

Van Ark, E., Detrick, R., Canales, J., Carbotte, S., Harding, A., Kent, G., Nedimovic, M., Wilcock, W., Diebold, J., and Babcock, J. (2007). Seismic structure of the Endeavour Ridge: Correlations with seismicity and hydrothermal activity. *Journal of Geophysical Research*, 112:B02401, 22 PP.

Waldron, D. (1982). Structure characteristics of a subducting oceanic plate. Master's thesis, University of British Columbia, Vancouver, BC, Canada.

Webb, S. (1992). The equilibrium oceanic microseism spectrum. *Journal of the Acoustics Society of America*, 92:2141–2158.

White, R. and Clowes, R. (1987). Juan de Fuca plate crustal structure: Results from ocean bottom seismograph studies. *Geophysics Journal International*, 100:349–367.

White, R. and Clowes, R. (1990). Shallow crustal structure beneath the Juan de Fuca Ridge from 2D seismic refraction tomography. *EOS transcripts AGU*, 68(1371).

White, R., M^{c}Kenzie, D., and O'Nions, R. (1992). Oceanic crustal thickness from seismic measurements and rare earth element inversions. *Journal of Geophysical Research*, 97(B13):19683–19715.

Wilcock, W. S., Archer, S., and Purdy, G. (2002). Microearthquakes on the Endeavour segment of the Juan de Fuca Ridge. *Journal of Geophysical Research*, 107(B12).

Wilcock, W. S. P. M., Hooft, E., Toomey, D., Patel, H., Stakes, D., Barclay, A., Ramirez, T., and Weekly, R. (2007). The deployment of a long-term seafloor seismic network on the Juan de Fuca Ridge.

Wilson, D. (1993). Confidence intervals for motion and deformation of the Juan de Fuca plate. *Journal of Geophysical Research*, 98(B9):16053–16071.

Wilson, D., Hey, R., and Nishimura, C. (1984). Propagation as a mechanism of reorientation of the Juan de Fuca Ridge. *Journal of Geophysical Research*, 89(B11):9215–9225.

Yuan, T., Spence, G., and Hyndman, R. (1994). Seismic velocities and inferred porosities in the accretionary wedge sediments at the Cascadia margin. *Journal of Geophysical Research*, 99(B3):4413–4427.

Appendix A

Event Selection

The use of ocean bottom seismometers represents a growing area of seismology. In this thesis, I explored using data recorded on OBS for receiver function analysis. As shown in table A.2, few events suitable for RF analysis were recorded on the OBS over a time period in which one would normally expect to record a sufficient number of suitable teleseismic events. The main reason for the shortage of good quality teleseismic events recorded at the OBS sites is the noise levels. As seen in figure 5.2 and plots shown in this appendix (figure A.1–A.4), noise levels often obscured the P wave arrival, if not the entire event. In some cases, such as the event on 2011113 (figure A.3c-d), the signal to noise ratio is acceptable; however, the event is emergent resulting in an unsuccessful deconvolution. Analysis using land based stations generally requires events of magnitude 6 or higher. Due to the noise levels associated with the OBS sites, and the nature of the events of interest, this magnitude threshold at the seabed sites is closer to 7. This increase in magnitude reduced the number of events applicable for RF analysis at OBS stations in this thesis.

Each of the five stations where data were accessible also had individual issues that are reflected in the number of events used at each OBS station (table A.2). Station

KXBB had frequent data gaps, which made events unusable. Events recorded at KEBB are often dominated by infragravity waves (figure A.1–A.4). Data from the NEPTUNE stations are often filtered from public use. This data is now accessible at a later time; however, when data were being collected for this thesis, all recordings were not accessible in a timely manner.

Below are plots of events recorded at each station from similar BAZ and distances described in table A.1. In general, the signal to noise ratio decreases towards the east. Most events at PGC are of a quality acceptable for RF analysis, whereas at OZB there are less, and at the OBS stations even fewer events are usable. Further investigation is needed to determine if noise levels have an azimuthal or seasonal dependency.

Julian Date	**Latitude**	**Longitude**	**Magnitude**	**Back Azimuth** (°)	**Distance** (°)	**Quadrant**	**Stations**
2004249	33.07	136.62	7.2	296	69	NW	KEBB, KXBB
2005036	16.01	145.87	6.6	281	79	NW	KEBB, KXBB
2011097	38.25	141.64	7.1	300	65	NW	NC27, NC89, OZB, PGC
2010355	26.9	143.69	7.4	288	70	NW	NCBC, OZB, PGC
2004326	-15.4	-174.91	6.0	225	76	SW	KEBB, KXBB
2011113	-10.35	161.23	6.8	252	88	SW	NC27, NC89, OZB, PGC
2004326	15.68	-61.71	6.3	97	63	SE	KEBB
2005164	-19.99	-69.19	7.8	128	85	SE	KXBB
2010294	24.69	-109.16	6.7	143	27	SE	NC27, NC89, NCBC
2007164	13.55	-90.62	6.7	131	44	SE	OZB, PGC

Table A.1: Events from similar BAZ compared at each station in the following plots.

Station	Dates of Data Availability	Number of Possible M6+ Events	Number of Events Used
KXBB	08/2004–09/2005	101	0
KEBB	08/2004–03/2005	63	1
NCBC	01/2010–02/2011	153	0
NC27	10/2010–08/2011	204	0
NC89	01/2010–08/2011	249	1
OZB	04/1996–08/2011	1023	10
PGC	07/1993–08/2011	1185	13

Table A.2: Number of events used from each station compared to the total number of possible events.

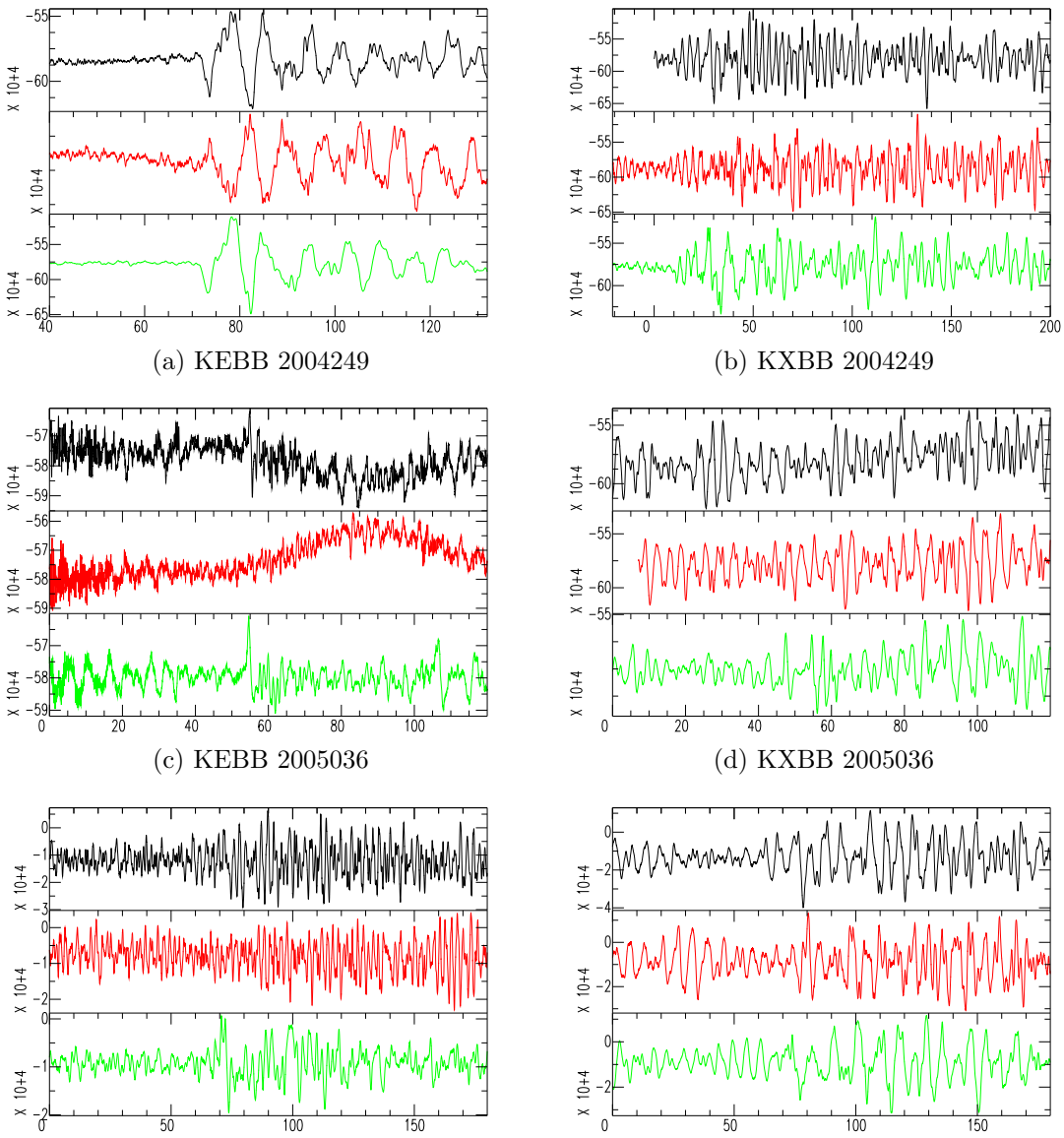

(a) KEBB 2004249

(b) KXBB 2004249

(c) KEBB 2005036

(d) KXBB 2005036

(e) NC27 2011097

(f) NC89 2011097

Figure A.1: Raw data from NW quadrant recorded at all stations. Black, red and green waveforms represent E-W, N-S and Z components, respectively. Vertical scale is digital counts, horizontal scale is seconds from arbitrary event extration time.

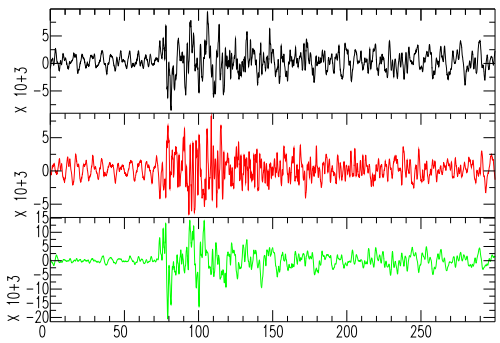

(a) OZB 2011097

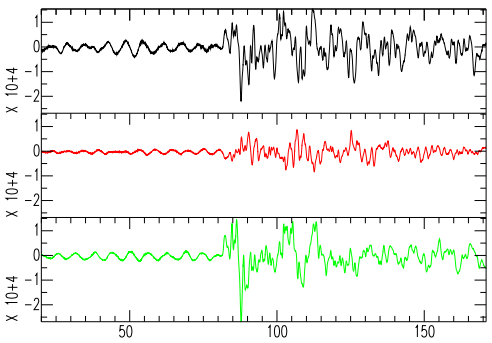

(b) PGC 2011097

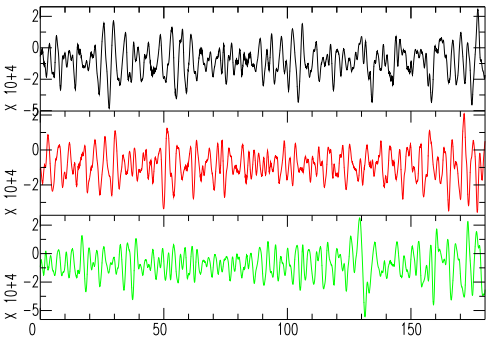

(c) NCBC 2010355

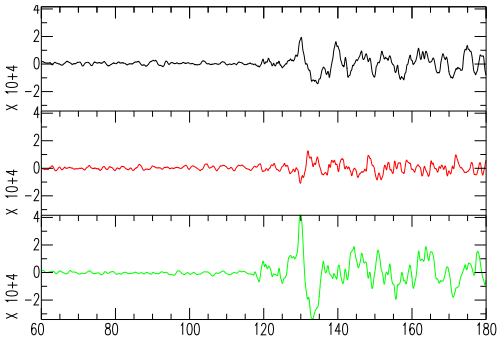

(d) OZB 2010355

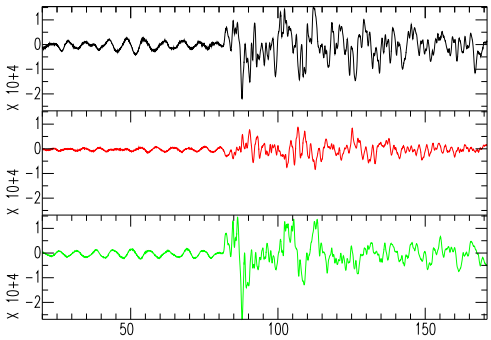

(e) PGC 2010355

Figure A.2: Raw data from NW quadrant recorded at all stations (continued). Black, red and green waveforms represent E-W, N-S and Z components, respectively. Vertical scale is digital counts, horizontal scale is seconds from arbitrary event extration time.

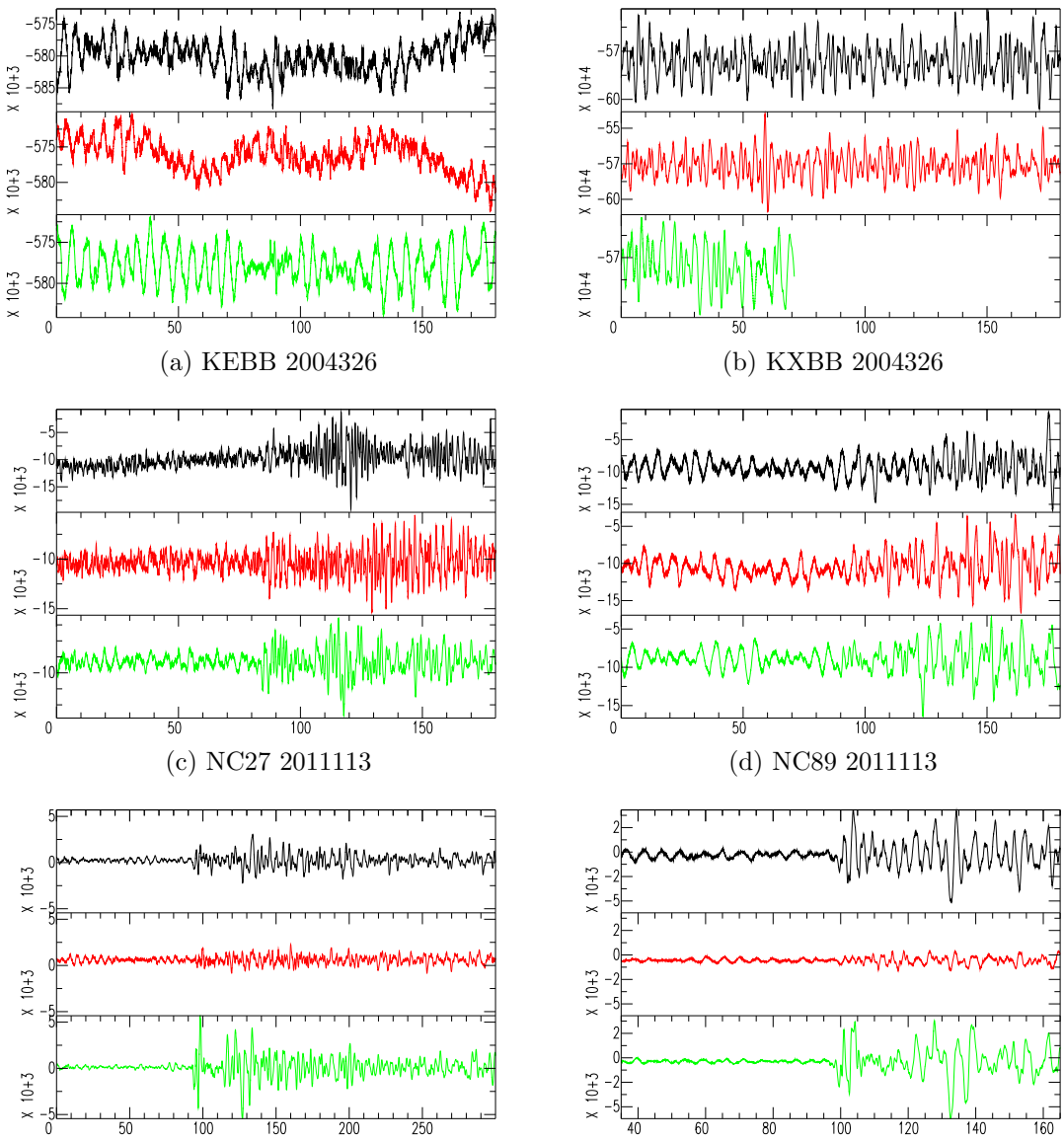

(a) KEBB 2004326

(b) KXBB 2004326

(c) NC27 2011113

(d) NC89 2011113

(e) OZB 2011113

(f) PGC 2011113

Figure A.3: Raw data from SW quadrant recorded at all stations. Black, red and green waveforms represent E-W, N-S and Z components, respectively. Vertical scale is digital counts, horizontal scale is seconds from arbitrary event extration time.

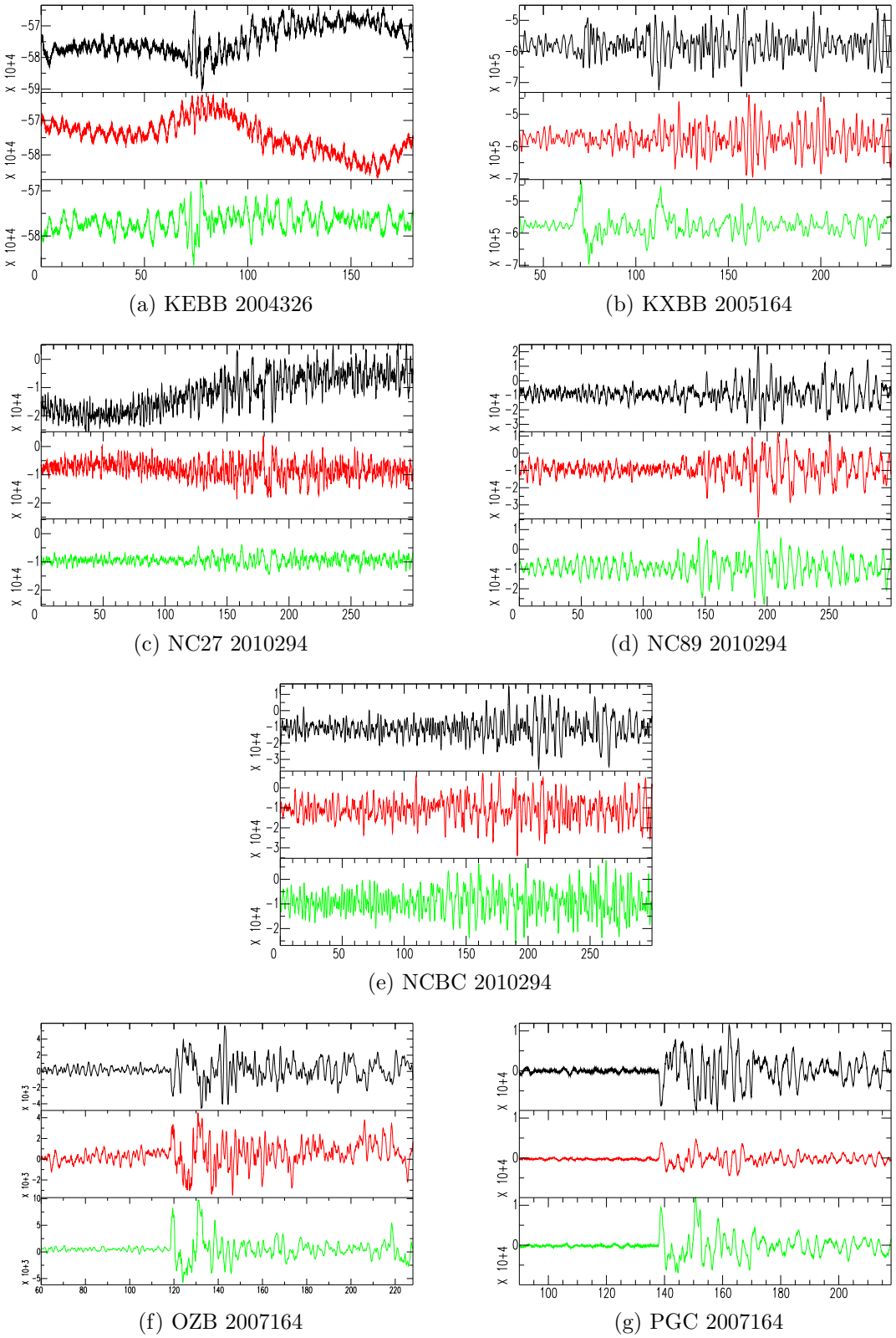

(a) KEBB 2004326

(b) KXBB 2005164

(c) NC27 2010294

(d) NC89 2010294

(e) NCBC 2010294

(f) OZB 2007164

(g) PGC 2007164

Figure A.4: Raw data from SE quadrant recorded at all stations. Black, red and green waveforms represent E-W, N-S and Z components, respectively. Vertical scale is digital counts, horizontal scale is seconds from arbitrary event extration time.